Ph.D. Thesis

박사 학위논문

Design, fabrication and characterization of magnetically actuated microrobots for targeted cell transportation

Sangwon Kim (김 상 원 金 相 元)

Department of

Robotics Engineering

DGIST

2017

Ph.D. Thesis

박사 학위논문

Design, fabrication and characterization of magnetically actuated microrobots for targeted cell transportation

Sangwon Kim (김 상 원 金 相 元)

Department of

Robotics Engineering

DGIST

2017

Design, fabrication, and characterization of magnetically actuated microrobots for targeted cell transportation

Advisor   :   Professor   Hongsoo Choi

Co-advisor :   Professor   Bradley J. Nelson

By

Sangwon Kim

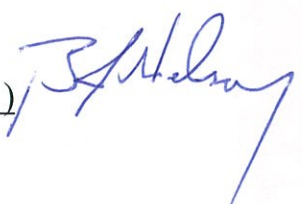Department of Robotics Engineering

DGIST

A thesis submitted to the faculty of DGIST in partial fulfillment of the requirements for the degree of Doctor of philosophy in the Department of Robotics Engineering. The study was conducted in accordance with Code of Research Ethics[1]

01. 06. 2017.

Approved by

Professor   Hongsoo Choi   (Signature)
(Advisor)

Professor   Bradley J. Nelson   (Signature)
(Co-Advisor)

Design, fabrication and characterization of magnetically actuated microrobots for targeted cell transportation

Sangwon Kim

Accepted in partial fulfillment of the requirements for the degree of Doctor of philosophy.

29. 11. 2016.

Head of Committee	<u>Prof. Hongsoo Choi</u>	(인)
Committee Member	<u>Prof. Bradley J. Nelson</u>	(인)
Committee Member	<u>Prof. Jonghyun Kim</u>	(인)
Committee Member	<u>Prof. Cheil Moon</u>	(인)
Committee Member	<u>Prof. Seung-Woon Yu</u>	(인)

Ph.D/RT
201132001

김 상 원. Sangwon Kim. Design, fabrication, Characterization of magnetically actuated microrobots for targeted cell transportation. Department of Robotics Engineering. 2017. 00p. Advisors Prof. Choi, Hongsoo, Co-Advisors Prof. Nelson, Bradley J.

ABSTRACT

Magnetically actuated microrobots were developed as a platform for the cell study and targeted transportation. Fundamental microrobotics for biomedical applications including the targeted therapy, efficient propulsion methods in the micro-scale environment, fundamental principal of magnetic manipulation and electromagnetic coils systems were briefly explained in the beginning of thesis. Proposed microrobots were fabricated with microfabrication technologies including the three dimensional (3D) laser lithography to form the basic structures, and metal sputtering system for deposition of magnetic material and biocompatible material, and are precisely controlled with magnetic fields to swim in the fluid environments. Scaffold shapes of microrobots were fabricated to carry the cells into the specific target area with 3D cell cultured microrobots; bundle of cells are entangled on the porous microrobots. Structures of scaffold type microrobots were designed to apply the various propulsion mechanisms such as pulling, rolling, and Corkscrew motions with cylindrical, hexahedral, spherical, and helical shapes, etc. First, the cylindrical and hexahedral shapes of microrobots were designed and fabricated, which microrobots were manipulated by external magnetic field gradient to pull and push those bulky structures. The maximum averaged translational velocities were evaluated as 50 μm/sec for cylindrical microrobots and 35 μm/sec for hexahedral microrobots under the 800 mT/m of external magnetic field gradient in the de-ionized (DI) water, respectively. The velocities and those pulling translation mechanism would be not suitable for micro-

scale swimming environment, because of the low Reynolds number fluid (high viscos force with low inertia force). To enhance the propulsion efficiency in this micro-scale swimming environment, the Corkscrew motion and rolling motion were suggested, and designed the helical and spherical shapes of microrobots, respectively with preserving the previous scaffold shapes. The maximum translational velocities were evaluated as 550 µm/sec for the helical microrobots and 1400 µm/sec for the spherical microrobots under 15 mT of magnetic field intensity and their step-out frequencies in the de-ionized (DI) water, which velocities were dramatically increased than previous cylindrical and hexahedral shapes of microrobots. The power efficiencies of developed four kinds of scaffold type microrobots were also compared among various microrobots developed, which defined as translational velocities per normalized current on the electromagnetic coils system. The power efficiencies for helical and spherical scaffold type microrobots were much higher than those of cylindrical and hexahedral shapes of scaffold type microrobots. Also ciliary microrobots were developed which also use one of the efficient propulsion mechanism in the low Reynolds number fluid inspired by microorganisms such as Paramecium which shows the non-reciprocal stroke motion to translate the body. The fabricated cilia, attached on the ellipsoidal body were manipulated by an electromagnetic coils system which generates stepping magnetic field to actuate the cilia with non-reciprocal motion. The cilia beating motion produces a net propulsive force to translate the microrobots. The magnetic forces on cilium were calculated with various input parameters including magnetic field, cilium length, applied field angle, actual cilium angle, etc., and the translational velocity was measured by experiments. Also the complex trajectory driving and the particle transport experiment were conducted to show the feasibility of the targeted cell or drug delivery. Developed scaffold type microrobots were also manipulated in the microfluidic

channels, to show the possibility for microrobots to perform in the blood vessels, or confined environment. The human embryonic kidney (HEK) cell culture, and hippocampal neuronal stem cells (NSCs) culture and differentiation were completed for scaffold type microrobots to show the feasibility for targeted cell transportation. 3D cell cultured microrobots of NSCs were proliferated and the NSCs were differentiated into target cells composing brain tissues such as astrocytes, oligodendrocytes, and neurons.

In summary, magnetically actuated microrobots were developed with various shapes with designated driving mechanisms such as four different shapes of scaffold types and ciliary type. Microfabrication technologies were used to form the basic 3D structures of microrobots, and nickel and titanium were deposited to manipulate by magnetic fields and for the biocompatibility. The position and orientation of developed microrobots were precisely controlled and the driving performances were evaluated and compared among the microrobots. The human embryonic kidney (HEK) cells were cultured on scaffold type microrobots. The hippocampal neuronal stem cells (NSCs) were cultured on scaffold type microrobots and differentiated into specific neuronal cells to show the possibility of NSCs therapy using microrobots.

Contents

List of Figures

List of Tables

1. INTRODUCTION

1.1 Background

1.1.1 Medical microrobots

Recently, the interest in the health has been growing by the influence of aging society and qualitative and quantitative growth of the medical market. According to this flow, the development of sciences and technologies on medical devices has been accelerating. Also, various advanced medical devices and technologies will be developed and clinically tested to overcome the problems of conventional surgical procedures for achieving a minimally invasive medicine.

Figure 1.1 One of the most successful surgical robot system, 'da Vinci' [1]

Robotics industries have been rapidly developed concurrently with growing of medical market. Now, robots are commonly found in everywhere around us which serve various works such as manufacturing, service, surveillance, military, and medical fields. Robots are getting sophisticated and smarter, which perform a lot of works that are hard work or cannot

be done by human. Figure 1.1 shows the image of the most successful surgical robot system, 'da Vinci' [1], which is the tele-operating surgical robot system and commonly available now a days in hospitals over the worlds. This robot helps surgeons to perform the surgical procedures effectively with minimally invasive methods. Capsule endoscopy is another commercially available medical procedure using robotic devices to record images of the gastrointestinal (GI) tracks using pill shaped capsule which has tiny camera (See Figure 1.2, image in the most lower right [2]). By the success of the medical robots such as 'da Vinci' and capsule endoscopy, the potential on medical robots have been proven, and various forms of medical robots would be steadily developed.
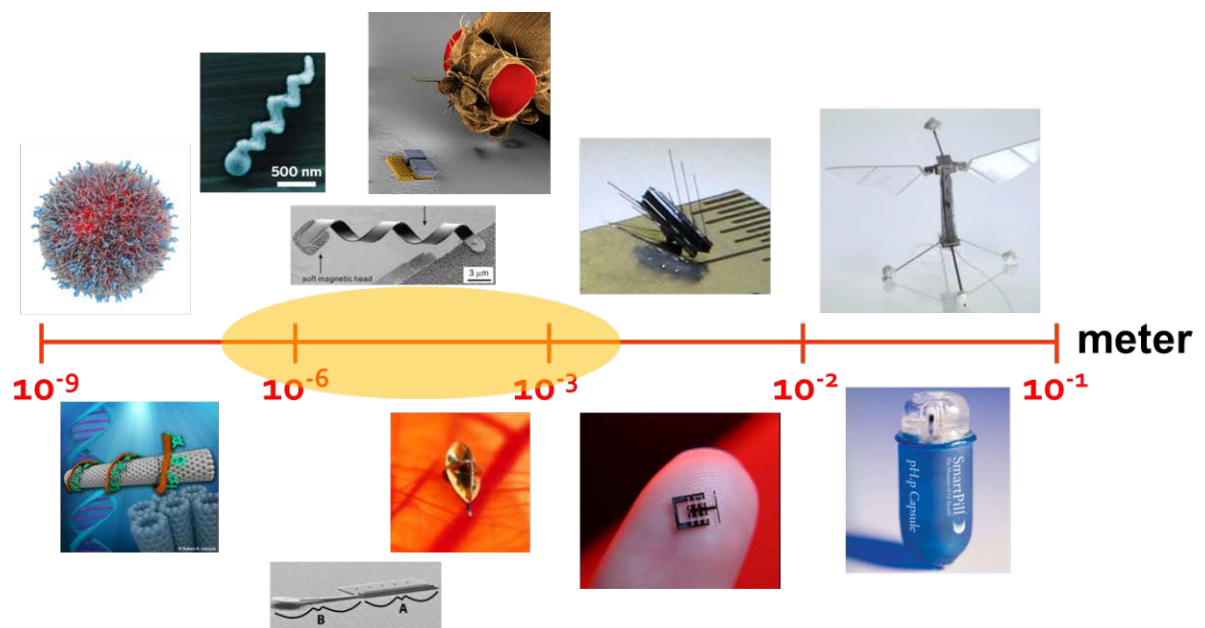
Figure 1.2 Scale of microrobots with some examples [2-10]

Microrobots are actively driven tiny mediators on a millimeter to micrometer size, designed to perform various missions to the unexplored space which may be dangerous or hard to access by human sensing. Figure 1.2 shows the scale of microrobots. Scale of microrobots covers generally micron-scale which is from 10^{-3} to 10^{-6} millimeters (1 micrometer to 1000 micrometers). But some of nanometers-scale and some of millimeters

scale robots could be countered. Figure 1.3 shows the various kinds of microrobots such as walking, crawling, flying, and swimming, etc. Most of microrobots for the medical applications would be the swimming microrobots, because their acting places are mainly fluids environments in the biological systems. The medical microrobots perform biomedical functions, such as diagnosis, treatment, neural interfaces, micro-surgery, cell/drug delivery, and transplantation by acting in the fluid environment such as cerebrospinal fluid (CSF), blood vessels, ureter, eyeball, etc. [11-16] Untethered microrobots could be one of the best robotic instruments for biomedical fields, because which have high level of degrees of freedom. Unlike conventional surgical methods, micro-surgery using microrobots has potential advantages, such as reduced pain, infections, and trauma in accessing a particular spot in the body, due to their small size and wireless intervention [11, 12].
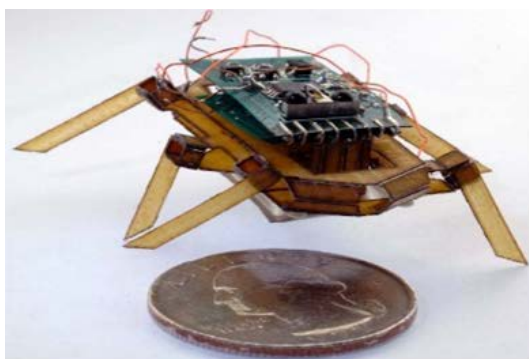
Walking microrobot

Flying microrobot
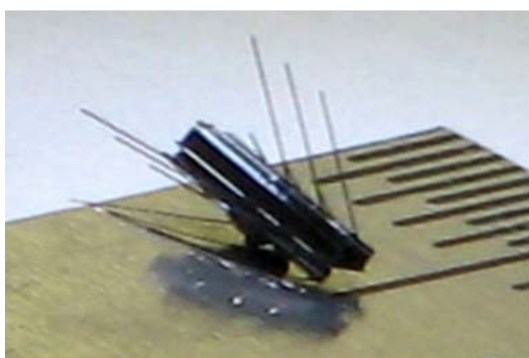
Crawling microrobot
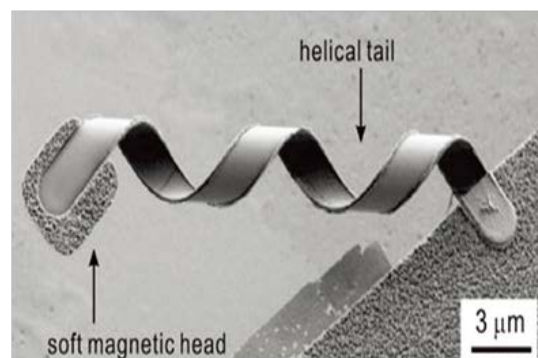
Swimming microrobot

Figure 1.3. Various types of microrobots [17, 18]

Figure 1.4 shows the various biomedical applications with microrobots [11]. The microrobots enable to deliver the drugs, radioactive, heat, and stem cells into the specific target area as targeted therapy. Microrobots could be the mechanical ablation and biopsy tools, and expand or block the blood vessels. Also microrobots could offer the structural benefits such as scaffolds and electrodes for interfacing. Markers and sensors could be altered into microrobots with mobility. For the control of those microrobots, wireless magnetic field actuation is the most famously used and it is one of the best selections for biomedical applications, because magnetic field is harmless to the biological system, and it has no distortion or attenuation during body penetration [11].

Figure 1.4. Various biomedical applications of microrobots. [11]

In this thesis, studies are focusing on the microrobots that are manipulated by external magnetic fields, as well as are mainly performing in the fluid environments, to conduct the medical functions as listed in Figure 1.4.

1.1.2 Microrobots for regenerative medicine

Tissue engineering has been actively studied in terms of its use in treatment or regeneration of tissue [18, 19]. Figure 1.5 shows a conceptual image of tissue engineering. The purpose of tissue engineering is to understand the correlation between the structure and function of biological systems and to enhance or maintain the body's abilities by implanting fresh tissue (cell-scaffold composites) after cultivation of extracted cells from tissues into functional structures. Human organ or tissue damage occurs more frequently with age. Despite rapid progress in medical engineering technology, organ transplant surgery has long been difficult due to high cost, the side effects of immunosuppressant, a lack of donors, and difficult surgical procedure in some specific area such as brain or small spots.
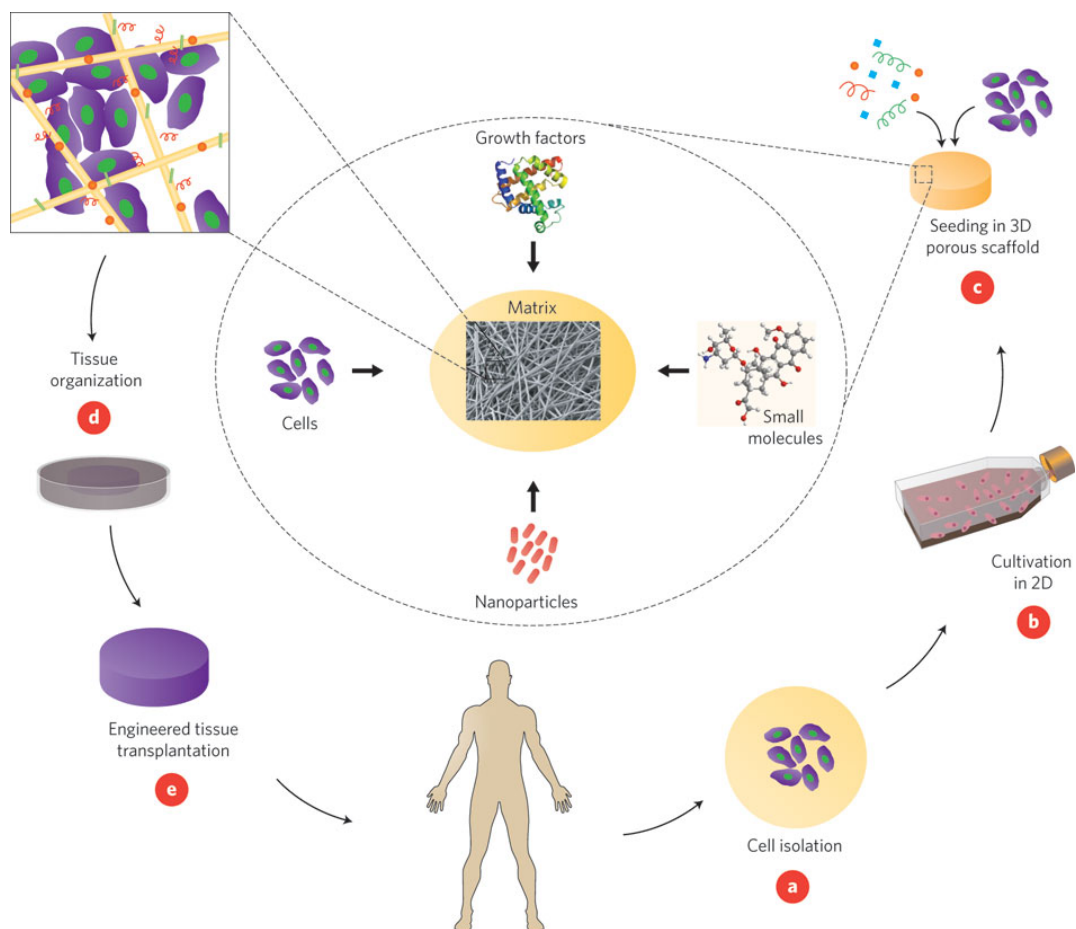
Figure 1.5 Conceptual image of tissue engineering [20]

Stem cell therapy has emerged as a promising therapeutic method to restore damaged tissue or organs in various diseases [21-25]. Recently, Neuronal stem cells (NSCs) have been considered a promising route for neuro-regenerative medicines for degenerative neural disorders, such as Alzheimer's disease. It is important to deliver stem cells precisely into a targeted area of the brain for accurate and effective stem cell therapy. Thus, microrobots could constitute novel therapeutic agents for enhancing the effects of neuro-regenerative therapeutics using NSCs.

Bio-scaffolds for tissue regeneration must meet the following conditions. Bio-scaffolds should be manufactured from materials that support attachment of cells and differentiation of active cells within the structures. The structure of bio-scaffolds should be porous to allow for proliferation and regeneration of cells. The interconnectivity allows circulation of nutrients to all cells inside the structure. For use in specific areas, the scaffold may be biodegradable. The sizes of structures and pores are determined by the target shape, cell size, and cell density [26].
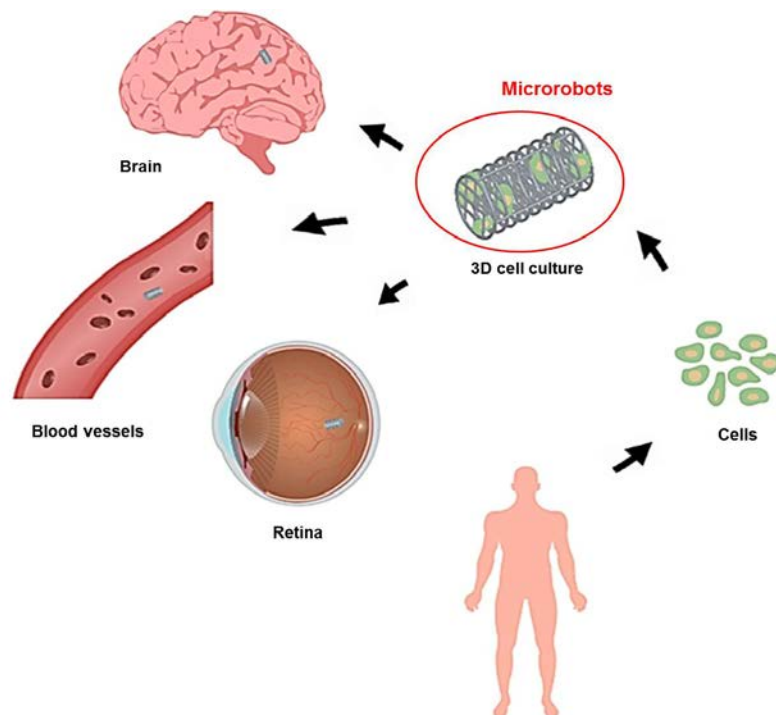
Figure 1.6 Conceptual image of cell therapy using microrobots

The conventional implantation process is associated with a risk of infection and trauma, and scaffold insertion is difficult in typically affected areas, such as blood vessels and brain tissue, which may require critical treatment. These scaffolds are directly inserted into the desired position by invasive methods or by natural orifices, such as by hand or using tools like a needle. The accessing for critical place without damages on the target structures is also challenging so far. Therefore, to solve this problem the microrobots could be introduced as a stem cell delivery platform. Figure 1.6 shows the concept of the possible applications and methods of our targeted cell transportation system. Cells or reparable tissues can be extracted from the human body or can be synthesized outside the body. The cells or tissues are implanted in the microrobots within a scaffold shape, which can then enter the body to be delivered into the target area. The proposed microrobots may be one of the promising tools for *in vivo* stem cell delivery for future stem cell therapies.

1.2 Research trend or related research works

1.2.1 Magnetic microrobots
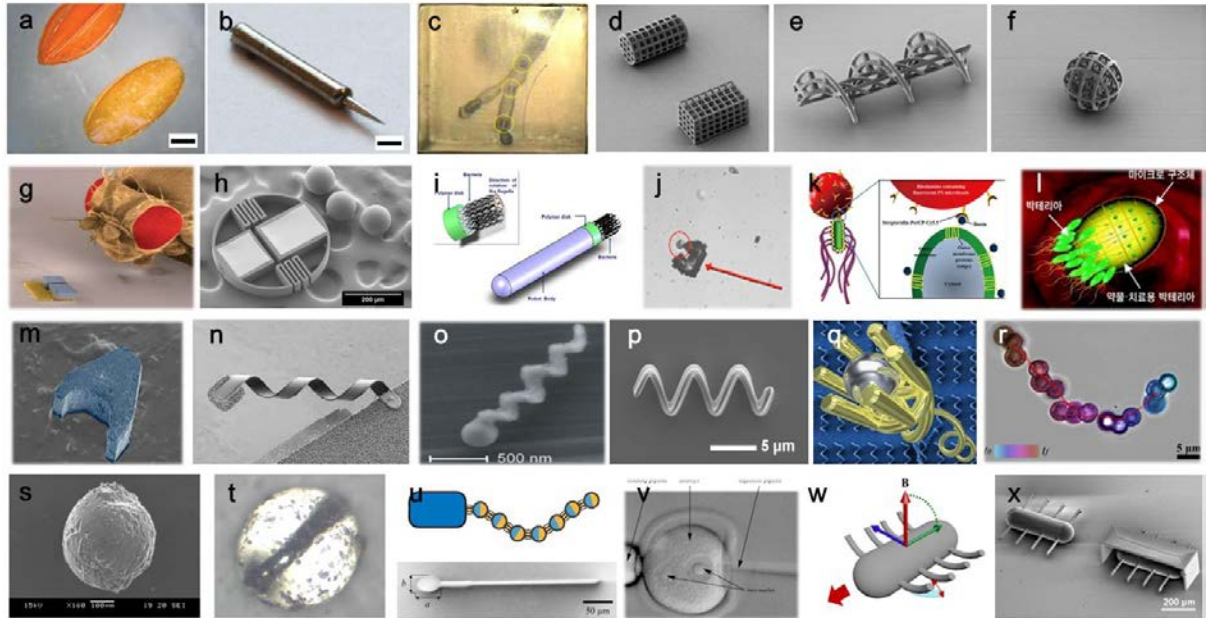
Figure 1.7 Various kinds of microrobots. (a) microrobots with two cross-assembled plates [1], (b) bulky microrobots with needle [27], (c) bulky microrobots in the blood vessel phantom [14], (d) cylindrical and hexahedral scaffold type microrobots [28], (e) helical scaffold type microrobots [28], (f) spherical scaffold type microrobots [28], (g-h) spring-mass type oscillating microrobots [29], (i-m) bacteria-based microrobots [30-34], (n) metal helical microrobots by self-rolling method [4], (o) helical microrobots with glancing angle deposition method [5], (p) helical microrobots with 3D laser lithography [35], (q) helical microrobot with gripper [36], (r) modular microrobots with magnetic particles [37, 38], (s-t) spherical microrobots with magnetic stick inside [39], (u) flagella-inspired microrobots [40, 41], (v) precise cell manipulation with microrobotic insertion system [42], (w-x) ciliary microrobots [43]

Many research groups have been developing magnetically driven microrobots because it is safe to the body, has no attenuation during body penetration, and easy to fabricate the agent without internal energy source as long as it contains magnetic materials inside. Various microrobots have been developed for biomedical applications with different kinds of magnetic field for accurate and efficient locomotion. Bulky, spring mass-based, spherical,

helical, and cilia-based microrobots have been controlled by external magnetic field gradients to pull and push [17], and oscillating and rotating magnetic fields to generate thumping [18], rolling [19], corkscrew [20-25], and ciliary stroke motions [43]. Figure 1.7 shows the various kinds of microrobots using different motions.
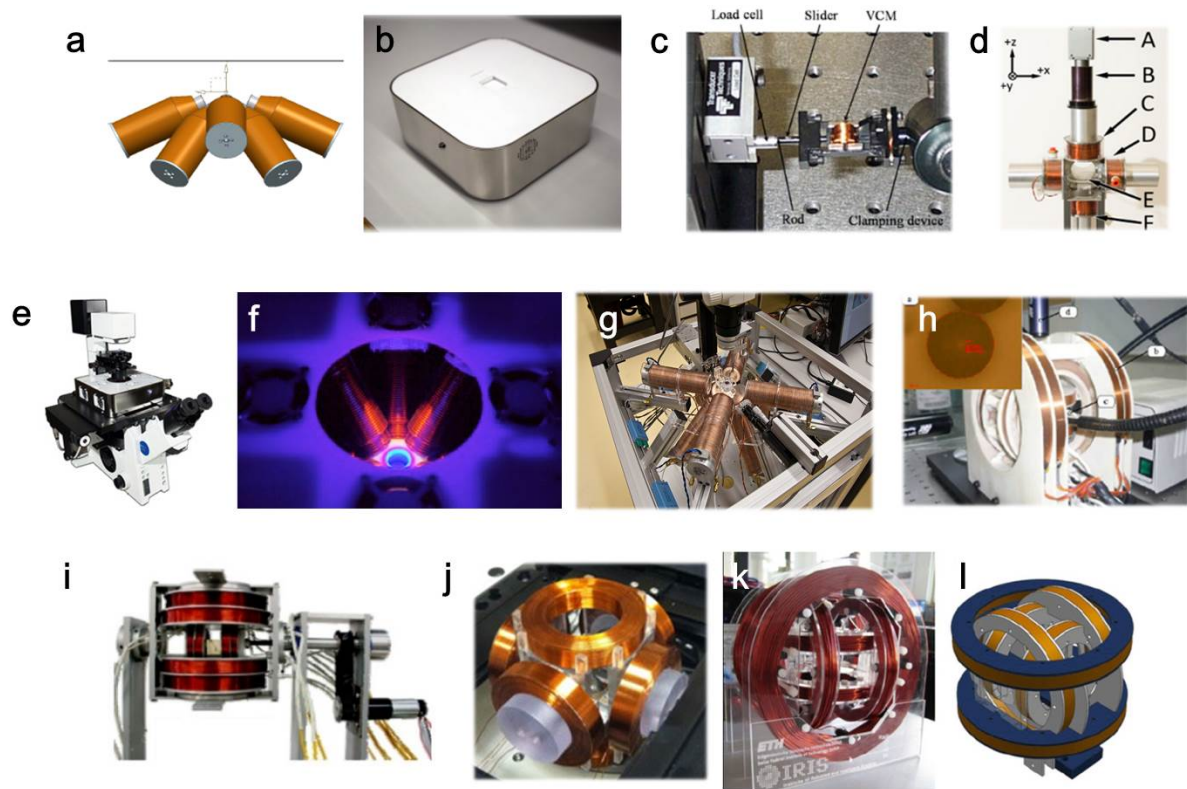
Figure 1.8 Various kinds of magnetic manipulators [34, 44-50]

Figure 1.9 Commercial magnetic steering systems as human-scale medical devices [51-53]

For the magnetic manipulation of microrobots, magnetic systems are needed and generally the electromagnetic coils systems are used. Many research groups have been developing the magnetic manipulators with higher performances such as higher field

intensities, smaller size of whole system, broad working area with uniform fields, low power consumptions, etc. Figure 1.8 shows the developed magnetic manipulators by the various research groups. Also several clinical tests have already been performed with commercially available magnetic manipulators; the Aeon Phocus, Aeon Scientific, GmbH, Switzerland [51], the Niobe system, Stereotaxis, Inc., USA [52], and the Robotic Catheter Guidance Control and Imaging (CGCI) system, Magnetecs, Inc., USA [53]. Figure 1.9 shows the commercial magnetic steering systems for human-scale medical devices. These devices are developed to treat the human arrhythmia which is cardiac disorder, need to be electrical treatment to regulate the abnormal electrical pathway in the heart. The magnetically steerable catheter is steered by magnetic fields, to access into the specific spot in the human cardiac system.

1.2.2 Various driving mechanisms

As listed in the Figure 1.7, there are various kinds of microrobots with different propulsion mechanisms for swimming of microrobots in the fluids. Different types of microrobot features and accurate manipulation techniques are being continuously developed, and increasing the efficiency of locomotion for microrobots is an important design goal. Reynold's number is the dimensionless number indicates the ratio between the viscous force and inertia force. equation (1) shows the Reynolds number.

$$\text{Re} = \frac{Inertial\ forces}{Viscouse\ forces} = \frac{\rho V L}{\eta} \qquad \text{equation (1.1)}$$

where ρ is density of the fluid, V is velocity of flow, L is characteristic length which indicate the size of the swimming object, η is the kinetic viscosity of the fluid. This equation implies that the inertial force based propulsion does not generate the effective motion for the swimming of small objects such as microorganisms or microrobots. Therefore efficient swimming in a low Reynolds number environment requires innovative approaches for

microrobots in terms of shape and actuating methodology on structure and mechanism design because of absence of inertia and presence of relatively high drag forces due to the small size of the microrobots.
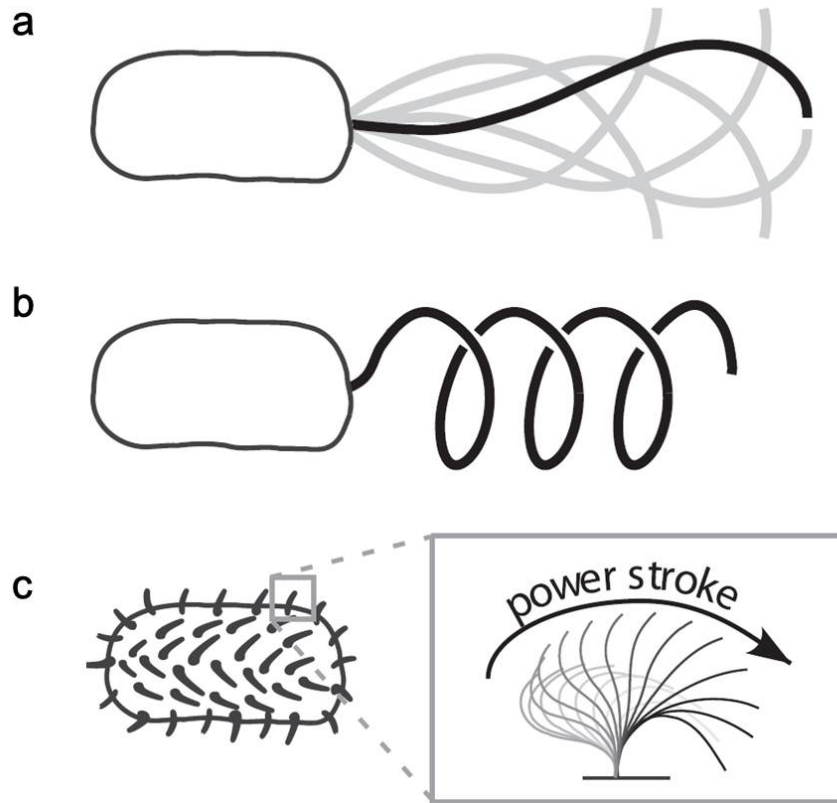
Figure 1.10 Various motions of microorganisms. (a) Prokaryotic flagellar motion, (b) eukaryotic flagellar motion, and (c) ciliary stroke motion [54]

Biomimicry is one of the most effective approaches to achieving energy-effective structures and functionality on a small scale [4, 36, 40, 41, 56-67]. Microorganisms sometimes provide inspiration for efficient moving in a low Reynolds number fluidic environment. Figure 1.10 shows the various motions of microorganisms [54]. Among the various motions of microorganisms, prokaryotic and eukaryotic flagellar motion and ciliary motion have been well reviewed theoretically. [11-27] Prokaryotic flagella show a corkscrew motion with helical tails, and to implement this motion, rotational magnetic fields were used.

Propulsion velocity of helical microrobots is determined by the drag forces, rotating frequency, intensity of magnetic fields, and geometrical parameters including the helix pitch. Eukaryotic flagella use a traveling-wave motion with flexible tail and the motion is possible by the external oscillating magnetic fields. Velocity for traveling wave motion is affected by the drag forces and bending stiffness of the tail. The effective motion by traveling wave is possible when the distributed actuation of tail part, therefore it is more difficult to implement than the helical propulsion. [1] Cilia move with a power stroke motion. The power stroke and recovery stroke motions have different actuating forces which make the net propulsive force for translation. A key characteristic of these motions is the requirement for non-reciprocal motion within the low Reynolds number fluids.

The design, fabrication and actuating methods for microrobots have been studied widely and realized with micro-/nano-technologies and the magnetic manipulation is one of the popular methods for biomedical applications. The designs for locomotion of many microrobots have been motivated by microorganisms for efficient manipulation under external magnetic fields. [68-70] Other mechanisms to manipulate micro-swimmers include biological and bio-hybrid approaches, which use a biological motor to achieve locomotion of microrobots. [71-74] However, such biological structures may have immune or toxicity issues, which may be unsuitable for in vivo applications. Also, the lifetime of microrobots based on a biological motor is relatively short and unstable in terms of material safety and reliability. Our main interests are the magnetically actuated artificial microrobots with high propulsion efficient for many potential applications. An artificial ciliary motion is an actuation mechanism that mimics non-reciprocal ciliary beating motion but it has not been reported before because of the difficulty to fabricate a ciliary structure with high aspect ratio. Thus, we propose an artificial ciliary microrobot to be actuated by the non-reciprocal actuation for net positive propulsion which mimics the cilium beating of paramecium.

In a low Reynolds number environment, time-symmetric movement cannot create a net propulsive force, as can be explained with Purcell's scallop theorem. [75] Thus, non-reciprocal motion of microrobots is required for effective locomotion within Newtonian liquids. Non-reciprocal motion can be achieved in one of two ways: a non-symmetric structure of the microrobot or non-symmetric actuation. For the first case, even though the actuating force is applied in a consistent and time-symmetric manner, a microrobot can move in a non-reciprocal way if the shape of the microrobots has chirality: a helical or other non-symmetrical shape [37, 38]. Artificial helical micro-swimmers using a corkscrew motion have been developed and their motions are realized by magnetic actuation. Magnetic locomotion was demonstrated by rotating a magnetic field, which generated a magnetic torque along the rotational long axis of the helical microrobots for a corkscrew thrust. Secondly, non-reciprocal motion can also be generated from non-reciprocal actuation. Micro-organisms using a traveling wave motion and a ciliary stroke motion may not have chirality in their shape, but they can generate a propulsive force by non-symmetric actuation motion. [75] If a non-symmetric actuation magnetic field can be applied, non-reciprocal motion is possible even with a symmetric structure. Microrobots using non-reciprocal motion due to non-reciprocal actuation have not been developed to our knowledge, probably because of the difficulty of implementing non-symmetrical actuation and fabricating the complicated ciliate structures.

1.2.3 Bio-scaffolds

A scaffold is a porous 3D structure that is used for cell adhesion and mechanical support for tissue and organ regeneration. [76–79] A 3D cell culture is important for sustaining the structural and functional complexities of the cells, because most in-vivo environments are 3D. Porous structures with controllable porosity have benefits over scaffolds with random pores,

because they exhibit enhanced characteristics, such as the ability to produce the proper nutrient supply, uniform cell distribution, and high cell density. Three-dimensional laser lithography offers excellent control over the geometry and porosity of the sample, as well as high resolution, and has been used recently to fabricate bio-scaffolds. [80–83] Figure 1.11 shows the bio-scaffolds fabricated by using the additive manufacturing methods such as 3D laser lithography.
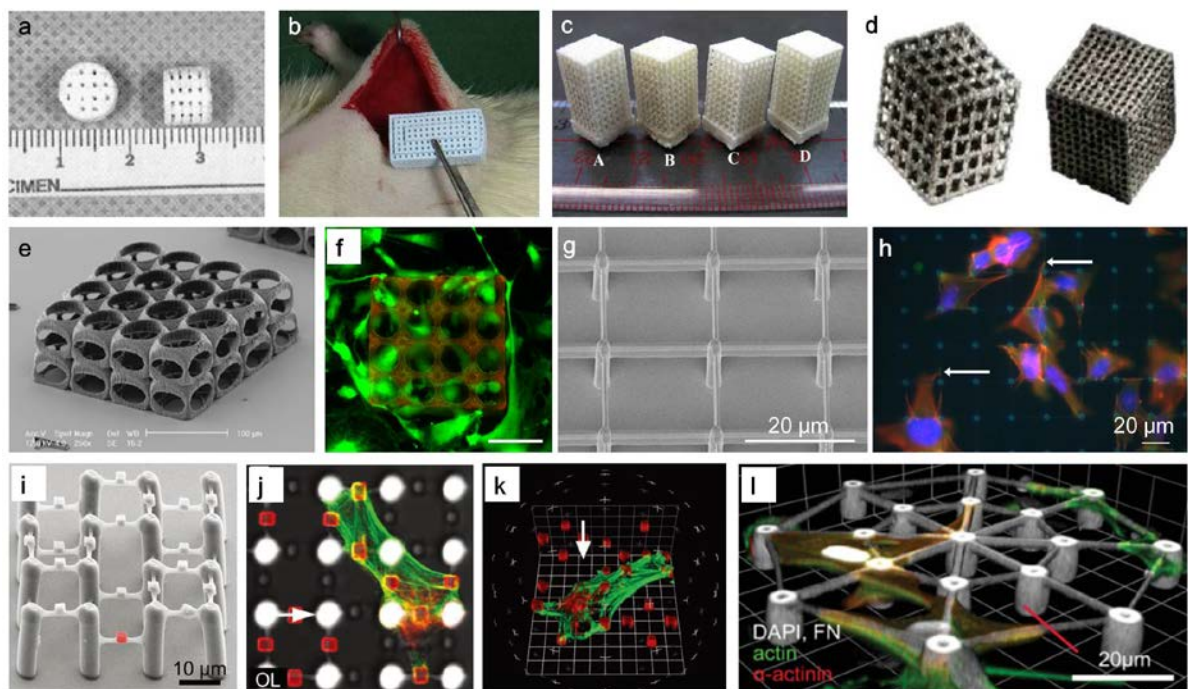
Figure 1.11 Various kinds of bio-scaffolds [80-83]

1.3 Magnetic manipulation

1.3.1 Magnetic manipulation

For the manipulation of magnetic microrobots, magnetic manipulator is required. Many research groups developed magnetic manipulators based on the electromagnetic coils. By the ampere's law shown in equation (1.2), the magnetic field is generated by the current through the coil.

$$\oint \boldsymbol{B} \cdot d\boldsymbol{l} = \mu_0 i \qquad \text{equation (1.2)}$$

where $\boldsymbol{B}$ is magnetic flux density, μ_0 is magnetic permeability in the free space, i is the current through the coil. Base on this equation (2), we can derive the magnetic fields with coil pairs called Helmholtz coil pair, and Maxwell coil pair. Figure 1.12 shows the configurations for Helmholtz coil pair and Maxwell coil pair. The magnetic fields from a single coil exponentially changes along with the distance from the coil center. However by using the Helmholtz coil pair or Maxwell coil pair, uniform magnetic fields or magnetic field gradient around the center between two coils can be achieved. The magnetic field from Helmholtz coil and magnetic field gradient from Maxwell coil are shown in equation (1.3) and (1.4).
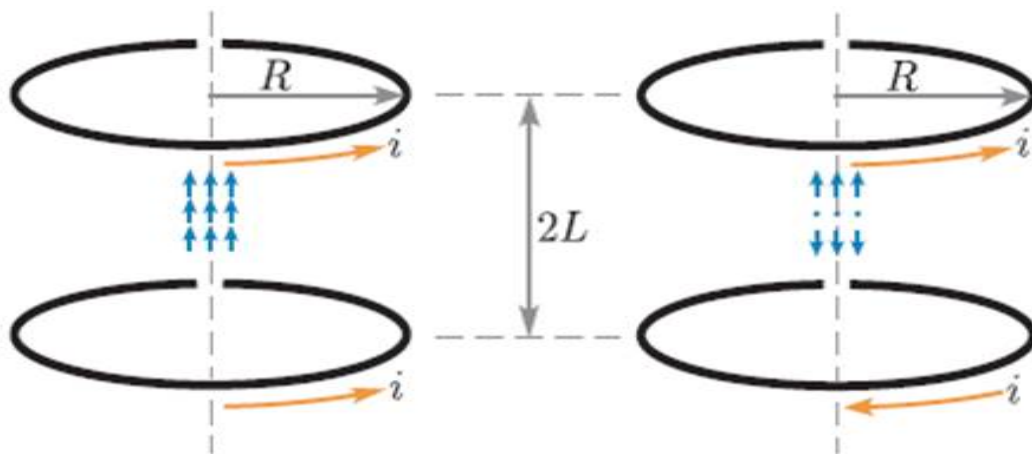
Figure 1.12 Helmholtz coil pair and Maxwell coil pair [54].

25

$$|\boldsymbol{H}| = \frac{R^2 i}{\left(R^2 + L^2\right)^{3/2}} \qquad\qquad \text{equation (1.3)}$$

$$\nabla|\boldsymbol{H}| = \frac{3R^2 L i}{\left(R^2 + L^2\right)^{5/2}} \qquad\qquad \text{equation (1.4)}$$

where, $\boldsymbol{H}$ is magnetic field intensity, R is radius of the coils, $2L$ is the distance between two coils, and $\boldsymbol{i}$ is current through the coils. In summary, the Helmholtz coil pair generates the constant magnetic field such as equation (1.3), and the Maxwell coil pair generates the magnetic field gradient indicated in equation (1.4).
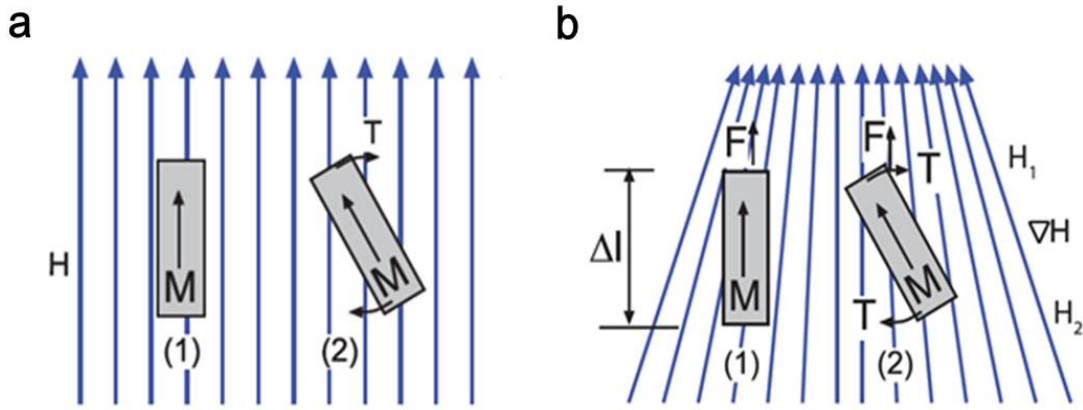
Figure 1.13 Magnetic torque and magnetic force. (a) Magnetic torque from magnetic field (H), and (b) magnetic force and torque from magnetic field gradient (∇H) [84]

Once we have magnetic field and field gradient, applied torque and force on microrobots could be calculated. Figure 1.13 shows the magnetic torque and magnetic force on magnetic materials or magnetic microrobots, which values could be calculated from the magnetic field (**H**), and magnetic field gradient (∇**H**). The magnetic torque from the magnetic field is indicated in the equation (1.5), and the magnetic force from the magnetic field gradient is in the Equation (1.6), respectively.

$$\boldsymbol{T}_m = v\boldsymbol{M} \times \boldsymbol{B} \qquad\qquad \text{equation (1.5)}$$

$$\boldsymbol{F}_m = v(\boldsymbol{M} \cdot \nabla)\boldsymbol{B} \qquad\qquad \text{equation (1.6)}$$

26

where, $\boldsymbol{T}_m$ is magnetic torque, v is the volume of magnetic material, $\boldsymbol{M}$ is magnetization of magnetic material, $\boldsymbol{B}$ is the applied magnetic field. $\boldsymbol{F}_m$ is the magnetic force, and the $\nabla\boldsymbol{B}$ is applied magnetic field gradient. Therefore, we can calculate the torque to control the orientation, and the force to control the position of microrobots, respectively.

1.4.2 Magnetic materials

Magnetic materials can be classified into three parts about their magnetic susceptibility, χ_m which is the quantified indicator showing the ability of the magnetic domains aligned by the external magnetic fields. Figure 1.14 shows the three classification and properties of magnetic materials. The materials with $\chi_m > 0$, are the paramagnetic materials which net magnetic domains align into external field direction with small magnetization (magnetic polarization) value, materials with $\chi_m < 0$ are diamagnetic materials which net magnetization direction is opposite direction of the external field also with small magnetization value. And materials with $\chi_m \gg 0$ are superparamagnetic or ferromagnetic materials which net magnetization direction is same as external field direction, and the magnetization value is very high.
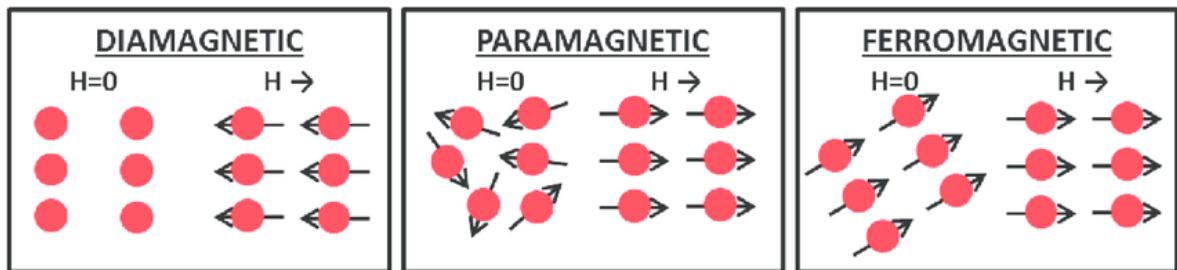
Figure 1.14 Classification of magnetic materials and their magnetic properties under the external magnetic field. [85]

Magnetic susceptibility is the material properties which indicate the net magnetization direction and the intensities for magnetic materials. And the magnetic permeability is also can be expressed by the magnetic susceptibility using equation (1.7).

$$\mu_m = 1 + \chi_m \qquad \text{equation (1.7)}$$

where, μ_m is magnetic permeability. When external magnetic field is applied on the magnetic materials, the magnetic flux goes through the magnetic materials. equation (1.8) shows the relationship between the magnetic flux density and the field intensity.

$$B = \mu_m H \qquad \text{equation (1.8)}$$

$$\mu_m = \mu_0 \mu_r \qquad \text{equation (1.9)}$$

where, μ_0 is the permeability in the free space. μ_r is the relative permeability, B is magnetic flux density, and H is magnetic field intensity. This equation can be expressed and ordered with χ_m using equation (1.10), to (1.13).

$$B = \mu_0 \mu_r H \qquad \text{equation (1.10)}$$

$$B = \mu_0 (1 + \chi_r) H = \mu_0 H + \mu_0 \chi_r H \qquad \text{equation (1.11)}$$

$$\chi_r H = M \qquad \text{equation (1.12)}$$

$$B = \mu_0 (H + M) \qquad \text{equation (1.13)}$$

Magnetic materials have residual magnetism, which enables for magnetic materials to act as the permanent magnets. Hard magnets are magnetic materials which are very hard for materials to be demagnetized; it means materials have strong residual magnetism inside by the initial magnetizing energy. Soft magnet is materials which magnetic domain is easily react under the external fields, and easy to change their domain orientation. Figure 1.15 shows the hysteresis curve (M-H curve) for "Hard" and "Soft" magnetic materials. The nickel (Ni) and cobalt (Co) is the soft magnetic materials, and the iron (Fe) and neodymium magnet (NdFeB) are hard magnetic materials.
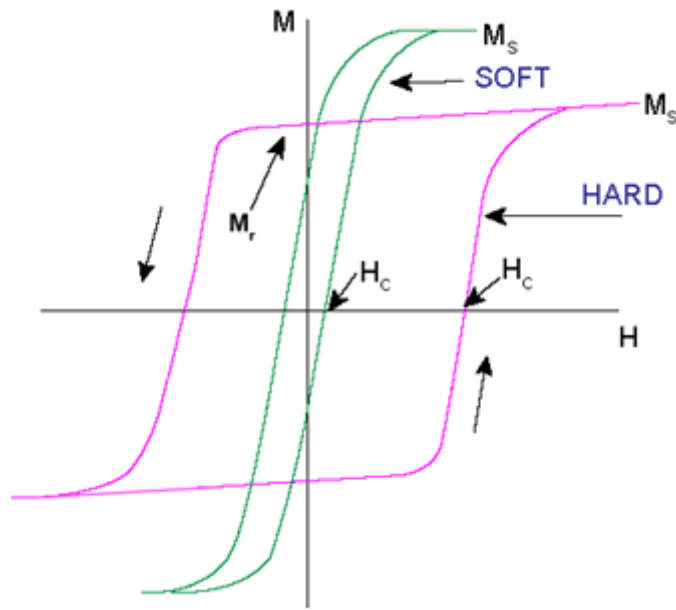
Figure 1.15 hysteresis curve (M-H curve) for "Hard" and "Soft" magnetic materials [86].

Magnetic materials have their own orientation for the magnetic fields because they have easy axis which is imaginary line for the materials to be aligned by the external field direction easily. If we want to control the orientation of magnetic materials, we should expect the magnetic easy axis of the materials. Figure 1.16 indicates the kinds of magnetic anisotropy. All the anisotropy is originated from the magnetic domain arrangement and their reaction from the external fields. However, I classified magnetic anisotropy into three cases for easy understanding. Firstly, the shape of magnetic materials shows the easy axis and hard axis if which materials are homogeneous. This is called shape anisotropy (Figure 1.16(a)). The easy axis of cylindrical magnet is the longitudinal axis, so we can expect it would be align with external field direction. Second, the easy axis is determined from the atomic arrangement (magnetic domain arrangement) of the materials (Figure 1.16(b)) which is crystallographic orientation. Figure 1.16(b) shows the easy axis of the magnetite material which crystal lattice is arranged in different way along with the crystal direction. Atomic arrangement and the structures are different from the materials even it seems uniform, when we see the atomic

29

arrangement in larger, we can see certain arrangement to determine the anisotropy of the materials. Third, we can program, or putting the anisotropy on the magnetic materials, by the arrangement of magnetic materials inside of the structures or particles, which called programmed anisotropy (Figure 1.15(c)). By considering of the magnetic easy axis, we should design and expect the motion of magnetic materials to be controlled.
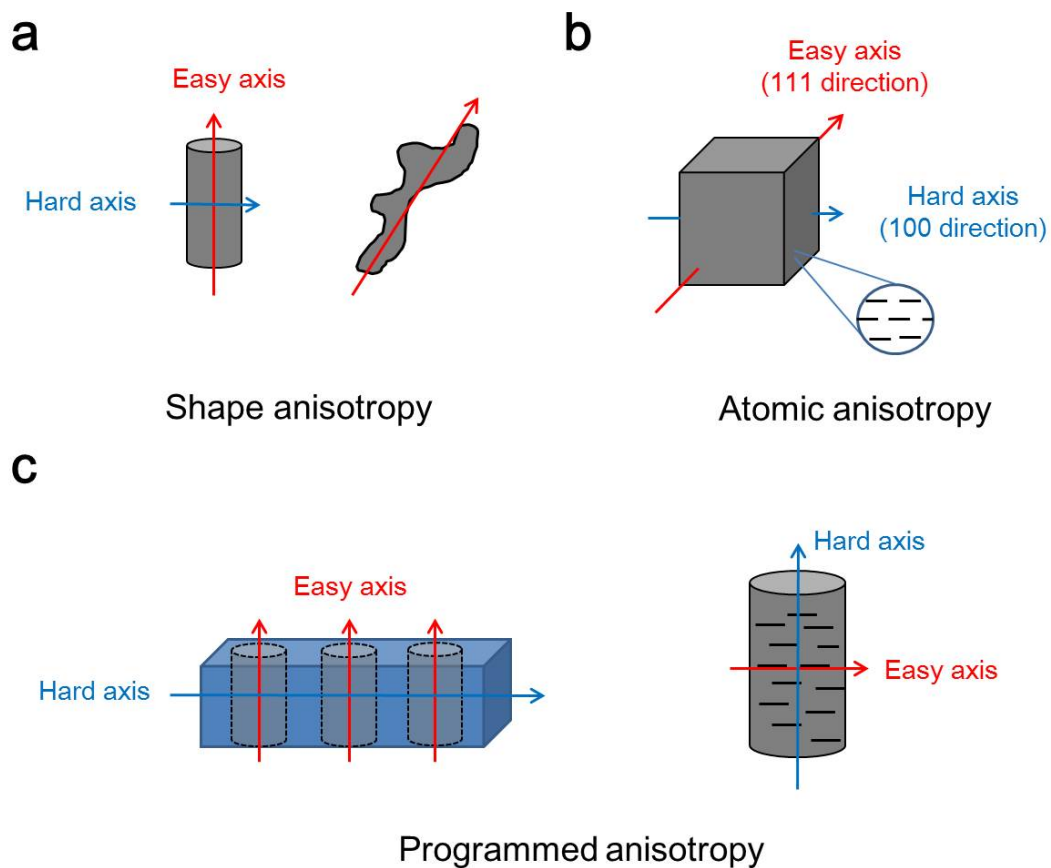
Figure 1.17 Magnetic anisotropy. (a) Shape anisotropy (macroscopic characteristics), (b) atomic anisotropy (microscopic characteristics), and (c) programmed anisotropy (macroscopic characteristics)

1.4 Objective of research

In this study, 3D porous microrobots were developed as a platform for cell delivery manipulated by magnetic fields. Design and fabrication of microrobots are introduced in section 2. Helical and spherical microrobots showed higher translational velocities than cylindrical and hexahedral microrobots. We characterized the motion of microrobots in the section 3, and demonstrated the manipulation of the microrobots with complex trajectories and in a microfluidic channel. The ciliary microrobots were developed as one of the efficient propulsion methods in the micro scale fluid environment. Cell attachment, proliferation, and differentiation of the hippocampal NSCs on the microrobots were confirmed with immunofluorescent staining and SEM images which are in the section 4. The NSCs were used for targeted and controlled differentiation into astrocytes, oligodendrocytes, and neurons on the microrobots. These results showed the feasibility of the microrobot as a platform for a new era of neuro-regenerative medicine. The proposed microrobots may be promising tools for *in vivo* NSC delivery, with high propulsion efficiencies for future stem cell therapies.

2. DESIGN AND FABRICATION OF

MICROROBOTS

2.1 Design and fabrication of scaffold type microrobots

Scaffold type microrobots were fabricated by Microelectromechanical systems (MEMS) technologies. Conventional MEMS technologies are commonly accomplished on the silicon wafer, glass wafer, or ceramics with several series of micromachining technologies including photolithography, wet and dry etchings, depositions, growing, surface treatments, etc., and those results fundamentally show two dimensional features. Three dimensional (3D) microrobots could be formed by 3D fabrication systems such as 3D printers or 3D laser lithography systems, etc. However, the feature resolution of 3D printer is not so high which is difficult to form less than 1 mm of feature size therefore, the 3D laser lithography system were used for microrobots fabrication in this research.
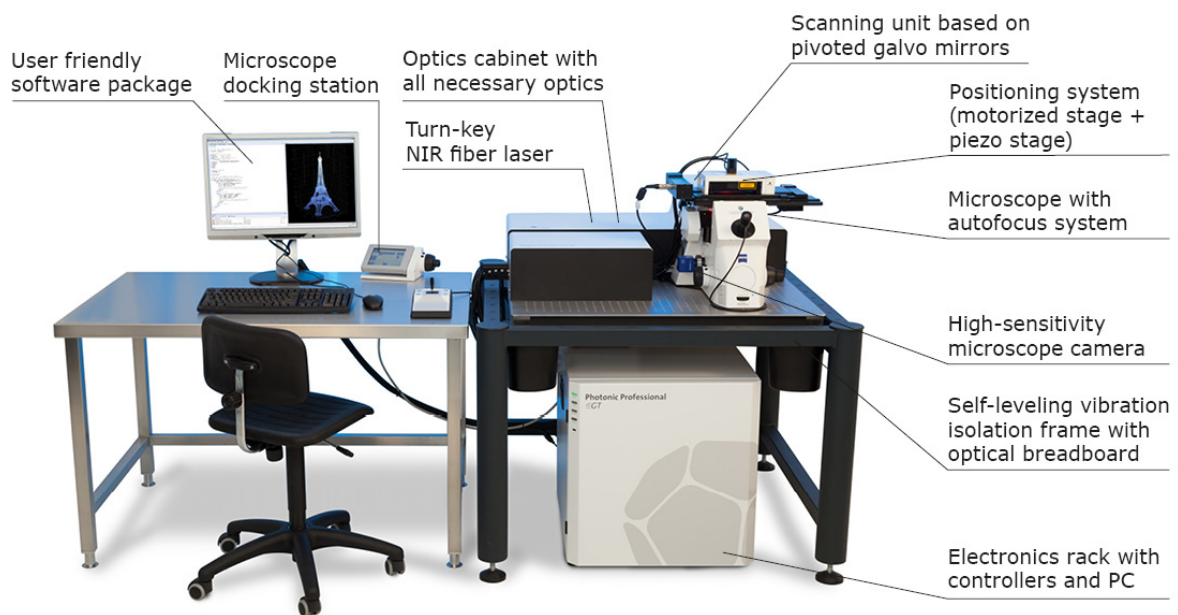
Figure 2.1 The picture of the 3D laser lithography system [87]

2.1.1 3D laser lithography system for microrobots fabrication

3D laser lithography is the one of the photolithography techniques which is procedure to form a designated patterns or structures on a substrate, using photosensitive material called photoresist to be chemically changed by exposure of light energy source. 3D laser lithography offers excellent control over the geometry and porosity of the sample, as well as high resolution, and has been used recently to fabricate bio-scaffolds. [76–33] Figure 2.1 is the picture of the 3D laser lithography system (Photonic Professional (GT), Nanoscribe GmbH). The system consists of the laser source, piezo-stage, motor-stage, galvo-stage, inverted microscope with laser focusing lens, sample holders, etc. The femtosecond laser (~780 nm of wavelength) was used to form the voxel (volume pixel) which is made by two photon absorption, which voxel becomes a minimum scanning point to exposure. By scanning of this voxel, the photo-sensitive polymer (photoresist; PR) became hardener of softener from basic properties of exposed PR. The movement of a precisely controlled piezoelectric stage enables to exposure a pre-programmed path to pattern the PR in 3D. The feature quality; resolution, voxel size, and the hardness without failure such as burning, insufficient energy, is determined by regulating of scanning parameters like a laser power, scanning speed, and slice distance between adjacent lines.
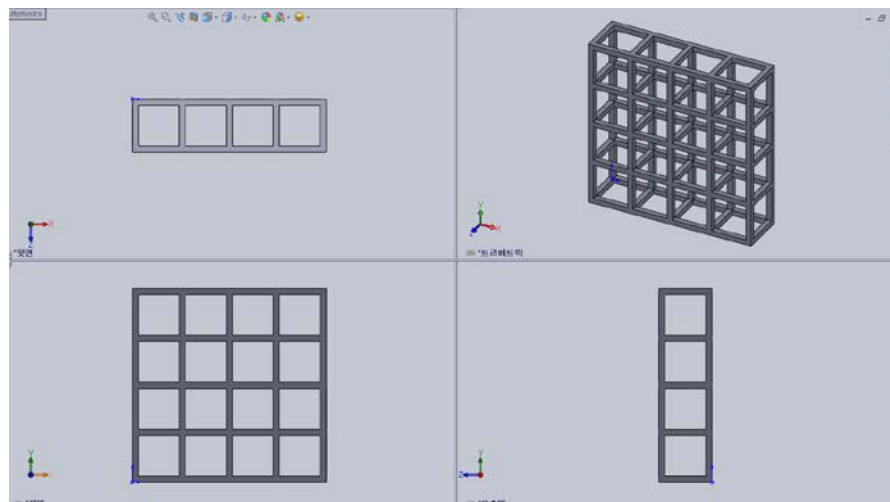
Figure 2.2 A CAD layout for scanning parameter test of 3D laser lithography system

Table 2.1. Test parameters for 3D laser lithography system using SU-8 photoresist with the oil-immersion 100x Zeiss objective lens [88].

Slice distance[a] [μm]	Scan speed[b] [μm s^{-1}]	Laser power[c] [mW]
1.2	50	2.0
0.9	100	3.2
0.6	200	4.4
0.3		5.6

[a] Slice distance is the distance between adjacent horizontal lines. [b] Scan speed and [c] laser power determine the total laser power delivered to the exposed spot. The combination of these parameters determines the quality of the structure, as shown in Figure 2.3.
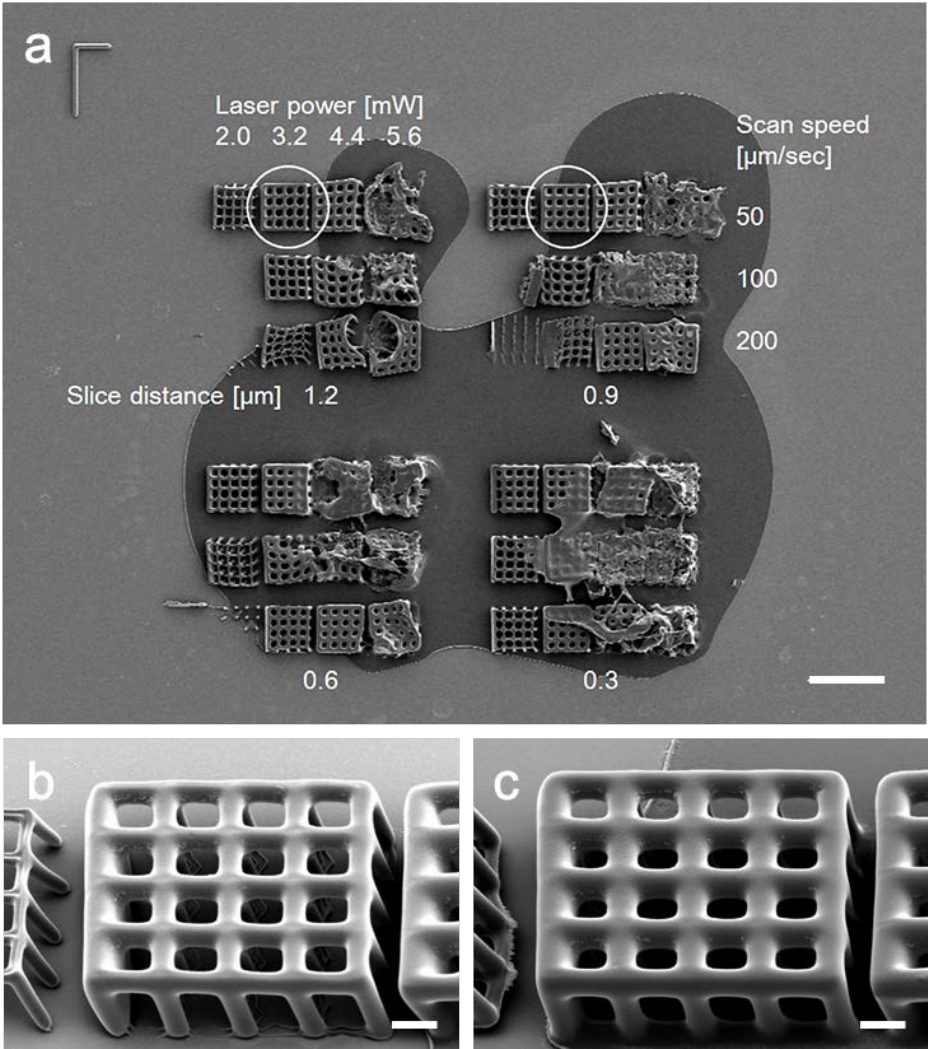
Figure 2.3 SEM image of parametric test results using SU-8with test structures. (a) Array of test structures, scale bar is 100 μm, Two well-defined structures with optimum parameters; 1.2 (b) and 0.9 μm (c) for the slice distance, 50 μm/s for the scan speed, and 3.2 mW/s for the laser power [88].

34

Before fabricating the complicated structures, writing parameters of the 3D laser lithography system were tested. Computer aided design (CAD, Solidworks, Dassault Systèmes SolidWorks Corp., USA) software was used to draw the 3D structures. Figure 2.2 is the design layout of simplified scaffold structure. Table 2.1 is the test parameters for the 3D laser lithography with an oil-immersion 100x Zeiss objective lens. Figure 2.3 shows the SEM image of simplified scaffold structures with SU-8 with different test parameters. The laser power, scanning speed, and slice distance were varied to check the quality of features, and which parameters would be different for the kinds of PR because of the differences of photosensitivity. Two well-defined structures were fabricated with optimum parameters; 1.2 (Figure 2.3(b)) and 0.9 μm (Figure 2.3(c)) for the slice distance, 50 μm/s for the scan speed, and 3.2 mW/s for the laser power.

Table 2.2. Designed and measured microrobot sizes [88].

Design[a] [μm]	I (I′)	II (II′)	III (III′)	IV (IV′)
Length	153.98 (157.00)[b]	144.20 (147.20)	154.40 (157.40)	156.60 (159.60)
Diameter	78.00 (81.02)	73.00 (76.00)	73.00 (76.00)	73.00 (76.00)
Line width	1.98 (5.08)	1.98 (5.08)	1.98 (5.08)	1.98 (5.08)
Pore size	13.22 (10.20)	16.00 (13.00)	20.00 (17.00)	24.00 (21.00)

[a] Each microrobot design has two shapes: cylindrical (I, II, III, and IV), and hexahedral (I′, II′, III′, and IV′). The diameter of the cylindrical shape of the microrobots corresponds to the width or height of the hexahedral-shaped microrobots. [b] The measured values for Type I were actually measured. The other values, Type I′, II, II′, III, III′, IV, and IV′ are the expected values based on the Type I measurement (see Figure S2 in Supporting Information).

The scanning parameters were optimized to form the features with SU-8 photoresist for scaffold structure. By using these values, the various designs of the scaffold type microrobots were fabricated. Figure 2.4 shows the SEM images of fabricated scaffold type microrobots. The design values of microrobots are listed in Table 2.2. Those scaffold microrobots are designed to culture the cell on the microrobots, therefore the pore size is designs as 10~21 um

to cover the general mammalian cell size which is around 10~20 um. Also the array of microrobots could be fabricated with same methods. Figure 2.5 shows the SEM images of cylindrical shape and hexahedral shape of scaffold type microrobot arrays with 10 um of pore size.
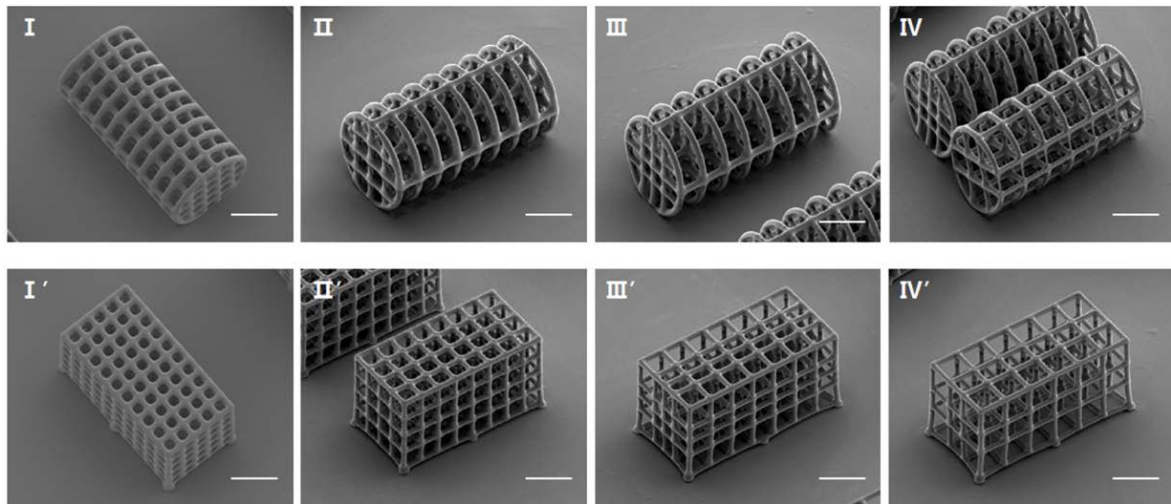
Figure 2.4 SEM images of various designs of the fabricated scaffold type microrobots. The design values are listed in Table 1. The pore sizes of the microrobots are 10, 13, 17, and 21 µm for I (I′), II (II′), III (III′), and IV (IV′), respectively, which covers most of the biological cell sizes. The scale bar is 40 um [88].
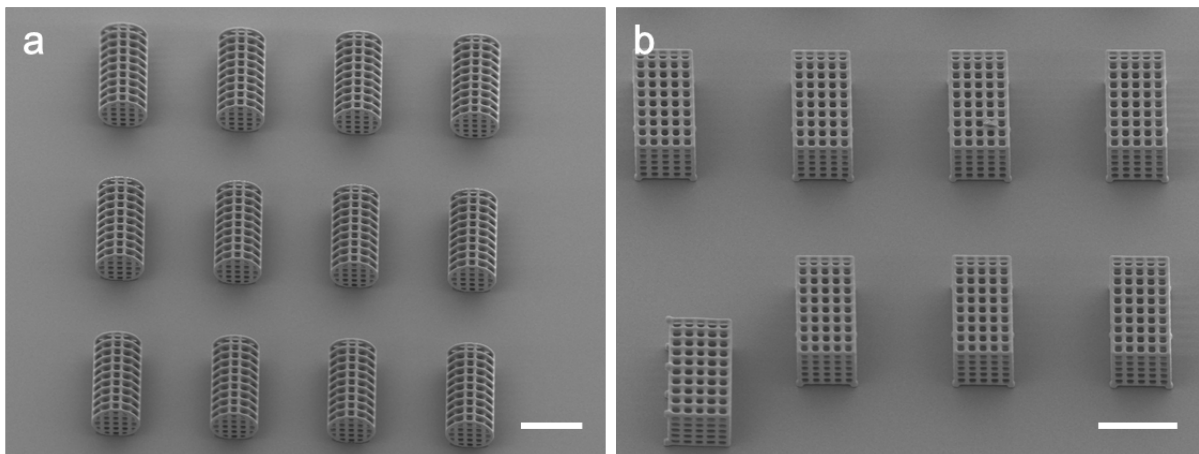
Figure 2.5 SEM images of microrobots array. (a) Cylindrical shapes of 12 microrobots array, and (b) hexahedral shapes of 8 microrobots array.

2.1.2 Detailed fabrication process for scaffold type microrobots

Microrobot structures were fabricated by 3D laser lithography system using SU-8 photoresist. However they have not magnetic properties to be manipulated with magnetic fields. Therefore the magnetic material should be included, and the most outer parts would be biocompatible material for the biomedical application. In this research, the nickel and titanium were used for magnetic material and biocompatible material, respectively and which were deposited by electron beam evaporation system.
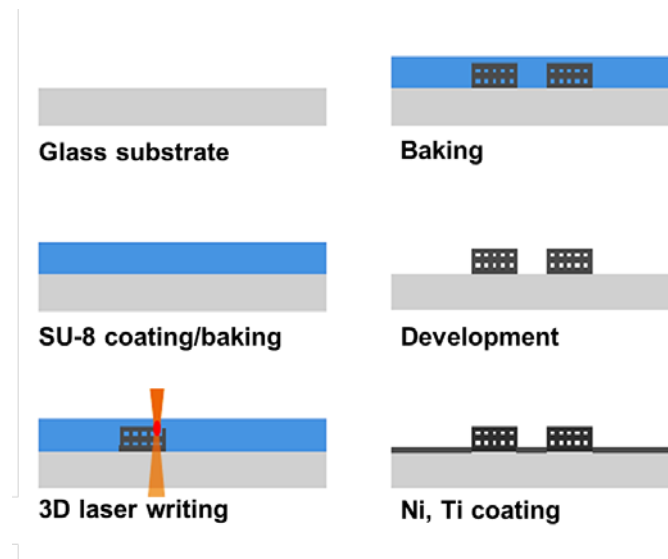
Figure 2.6 Overall fabrication processes for scaffold type microrobots [88].

Overall fabrication process for scaffold type microrobots with 3D laser lithography and metal deposition is shown in Figure 2.6. A 3 cm glass wafer was cleaned in an ultrasonic bath, using isopropyl alcohol (IPA) to remove any residual dust or organics. SU-8 (1.25 mL NANO SU-8 100, MicroChem, US) was spin-coated onto the glass wafer in two steps: 500 rpm for 10 s with a speed ramp of 100 rpm/s, and 1000 rpm for 30 s with a speed ramp of 300 rpm/s. This produced a 100 μm-thick layer of SU-8 on the glass wafer surface. Then, the substrate was baked using a two-step process at 65 ° C for 10 min, followed by 95 ° C for 30 min. Then, the substrate was cooled to room temperature for 10 min. Two-photon polymerization

(TPP) and 3D laser lithography were conducted to polymerize the designed structures partially, followed by a pre-development bake at 65 ° C for 1 min and a 95 ° C bake for 10 min. After cooling the substrate, mr-Dev 600 (micro resist technology GmbH, Germany) was used to develop the SU-8 for 20 min. After form the microrobot structures, 150 nm of nickel and 20 nm of titanium layers were deposited using e-beam evaporation; the chuck was rotated and tilted to reduce the shadowing effect [36, 88].
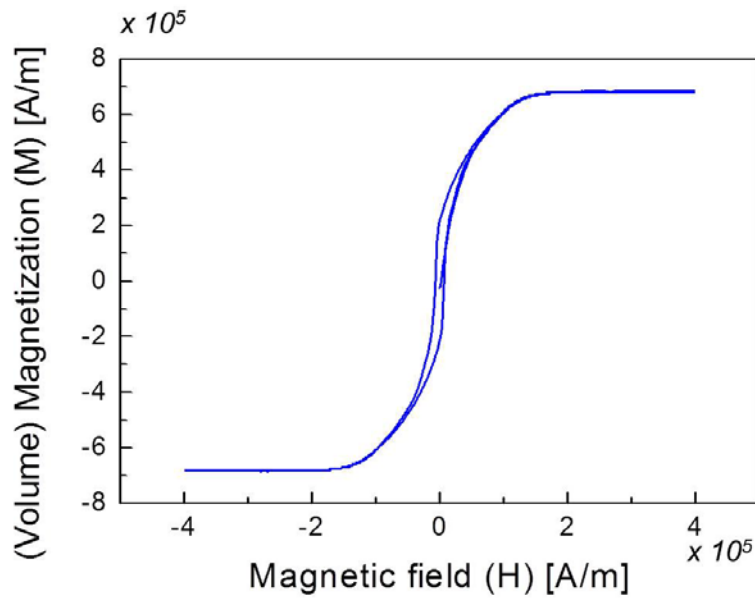
Figure 2.7 M-H curve for deposited nickel on microrobots

The magnetic property of deposited nickel was measured after fabrication of microrobots. High saturation magnetization and low coercive value are desired for fast actuation of magnetic materials. Figure 2.7 shows the measured magnetization per unit volume for nickel using Physical Property Measurement System (PPMS; Quantum Design, US). The measured saturation magnetization per volume was 686 kA/m 1 (686 emu/cm^3) and the coercivity was 5 kA/m (62.83 Oe), which suggested that the deposited nickel has a perfect ferromagnetic nature and suitable for magnetic manipulation of microrobots.

2.2 Design and fabrication of scaffold type microrobots with higher propulsion efficiencies

The cylindrical and hexahedral shapes of microrobots were fabricated in the previous section. By taking the advantages of different microrobot motions, various shapes of microrobots could be designed and fabricated. We can imagine the various kinds of scaffold type microrobots for the 3D cell culture on them. Figure 2.8 is the conceptual images of 3D cell cultured scaffold type microrobots with hexahedral, hexahedral with helical tail, helical, and spherical shapes. In this section, the scaffold type microrobots with different shapes are suggested for the better propulsion performance, and will be focused on the fabrication of those structures.
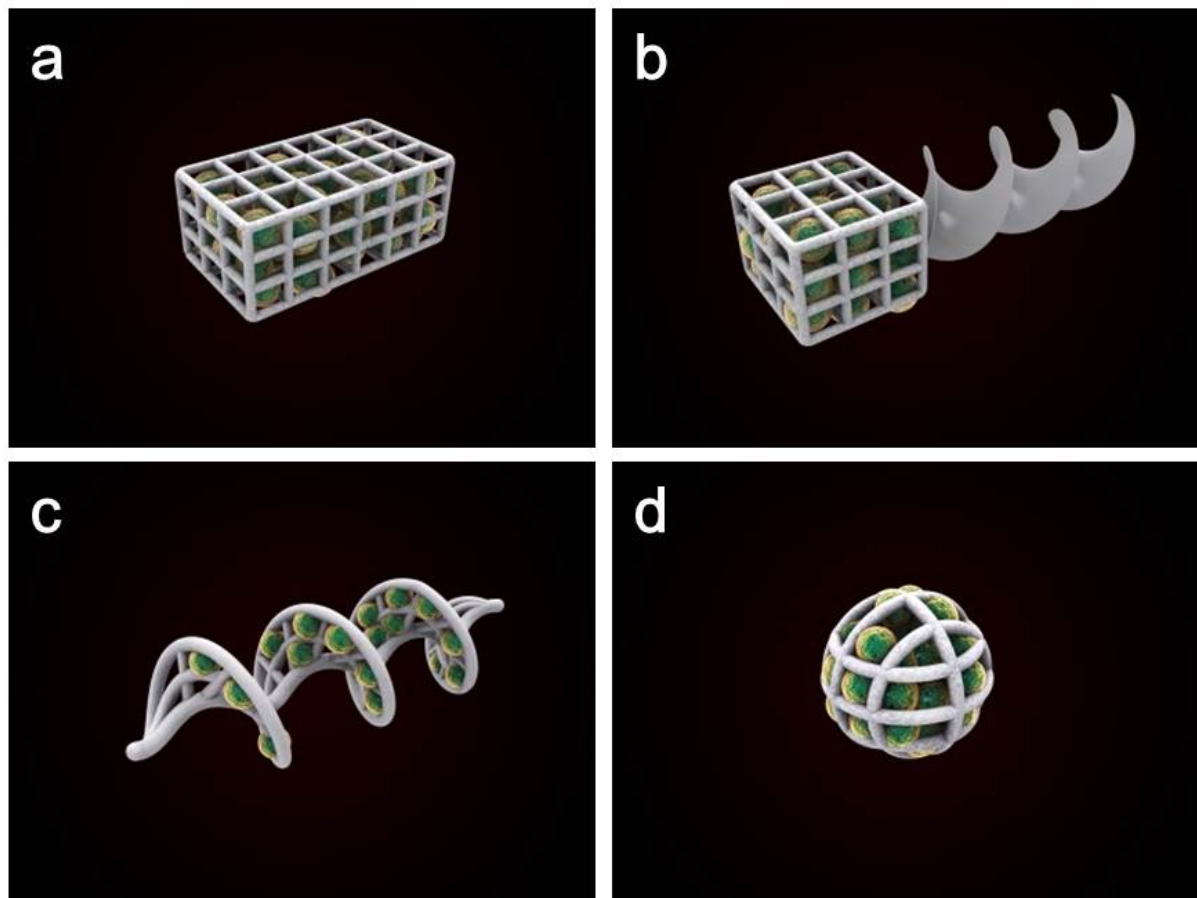
Figure 2.8 Conceptual images of 3D cell cultured scaffold type microrobots with (a) hexahedral, (b) hexahedral with helical tail, (c) helical, and (d) spherical shapes.

Various shapes of microrobots are fabricated using SU-8 as well as nickel and titanium bilayers, which fabrication processes are exactly same as described in section 2.1. Figure 2.9 shows the SEM images of various shapes of microrobots.
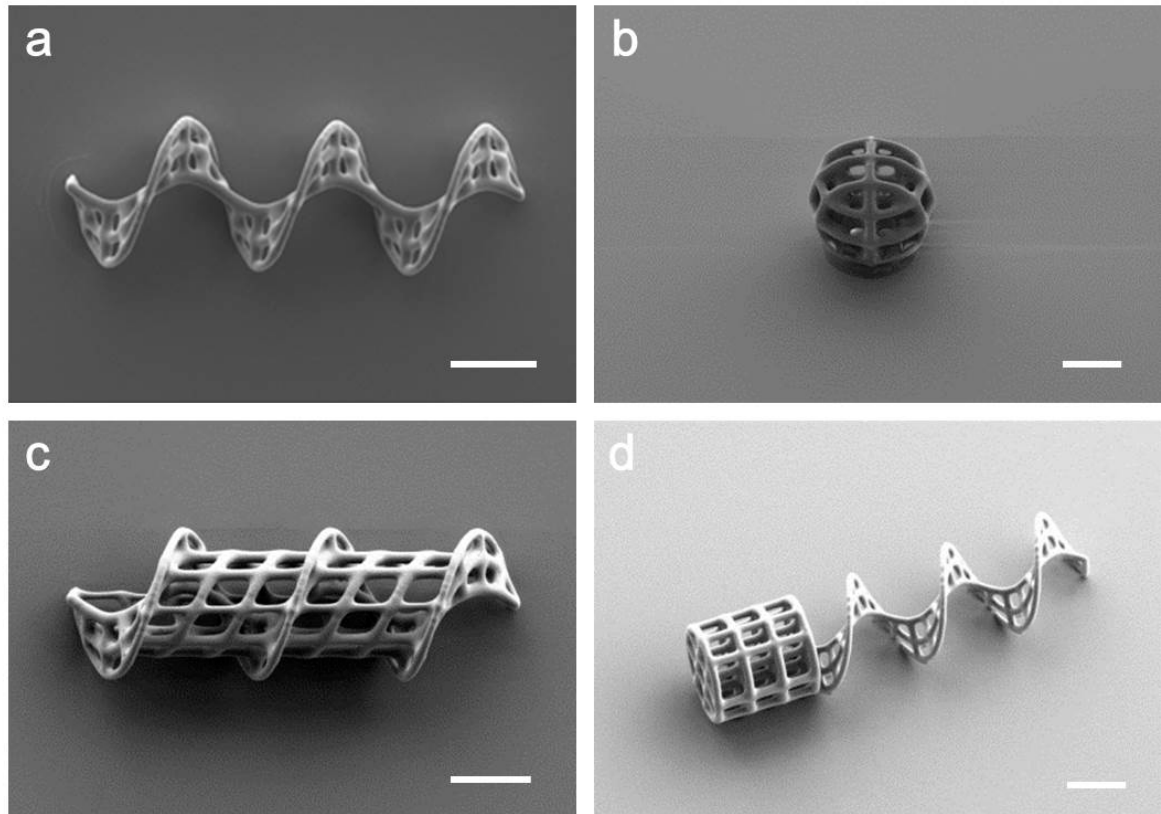
Figure 2.9 SEM images of various scaffold type microrobots with (a) helical, (b) spherical, (c) larger helical, and (d) cylindrical with helical tail shapes.
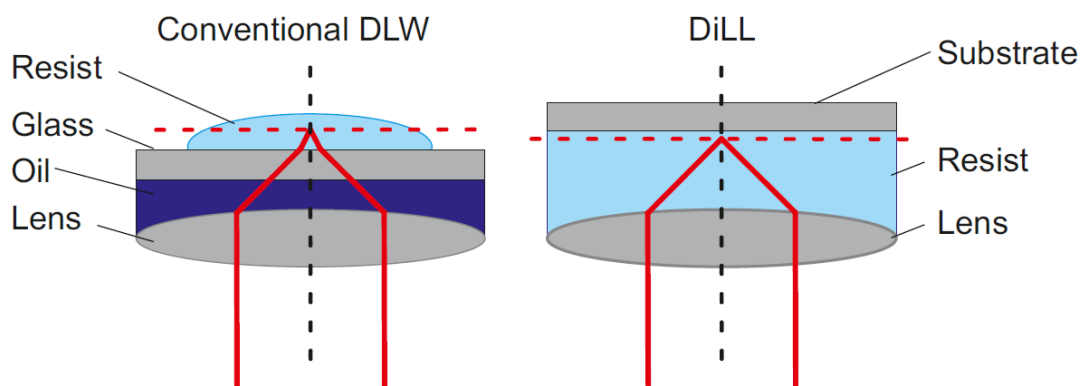
Figure 2.10 Comparison between the conventional writing configuration and Dip-in Laser Lithography [87]

So far, SU-8 was used for microrobots as a high contrast epoxy-based photoresist to provide the mechanical stability required for complex, full 3-D structures with high sensitivity to the light. However, the photolithography process with SU-8 is difficult because it needs long time of baking, and development process as well as its sticky property which make people hard to handle. By using the Dip-in Laser Lithography (DiLL) technique, we do not need the SU-8 photoresist anymore for microrobots fabrication, and the easier fabrication process we can take to achieve the similar results as conventional writing what we have done so far. For the Dip-in Laser Lithography, the oil immersion does not need, and that is mixed with specially designed photoresist such as IP-dip. Figure 2.10 shows the comparison between the conventional writing configuration and Dip-in Laser Lithography. From now on, the DiLL techniques would be used for microrobots fabrication with IP-dip photoresist.
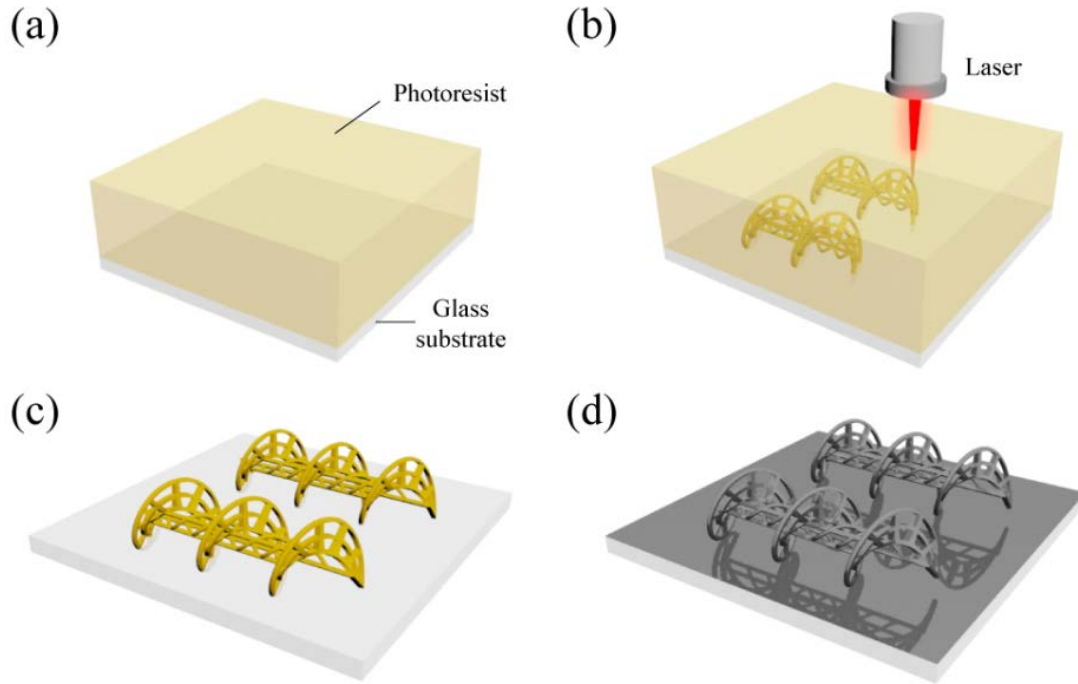
Figure 2.11 Overall fabrication processes for scaffold type microrobots with DiLL technique and sputtering system [28]

Figure 2.11 shows the overall fabrication process for four kinds of scaffold type microrobots by DiLL technique with IP-dip photoresist, and the deposition of nickel and titanium was also changes from evaporation to sputtering system to reduce the shadow effect. Glass substrates (2 cm^2) were cleaned and IP-dip (a photoresist; Nanoscribe GmbH, Germany) was applied at the center of the substrate (Figure 2.11(a)). The substrates were stuck on the holder with glue and inserted into the 3D laser lithography system (Photonic professional; Nanoscribe GmbH), and the CAD design for each microrobot was loaded on to the machine for laser writing. The writing code for each microrobot included writing parameters, such as scanning speed, laser power, and slice distance. These parameters were optimized for a designated structure by test writings. The optimum writing parameters were found to be a scanning speed of 70 μm/s, a laser power of 8.0 mW, and a slice distance of 0.3 μm. After laser writing, the designed structures were polymerized (Figure 2.11(b)) using a piezoelectric stage movement, and the structures were developed with SU-8 developer for 5 minutes at room temperature (Figure 2.11(c)). After realizing the structures, 170-nm nickel and 20-nm titanium layers were deposited with a sputtering system (SRN-110, Sorona, Inc., Korea) for magnetization and biocompatibility, respectively. Samples for magnetic manipulation and cell culture experiments were completed with the structures shown in Figure 2.11(d). The CAD layouts of four kinds of scaffold type microrobots, and SEM images after fabrication of scaffold type microrobots are shown in Figure 2.12. Design parameters for scaffold type microrobots with IP-dip photoresist is shown in the Table 2.3.

Table 2.3. Microrobot design parameters with IP-dip photoresist [28].

	Cylindrical type	Hexahedral type	Spherical type	Helical type
Length	156 μm	156 μm	80 μm	246 μm
Width	Diameter:	80 μm	80 μm	80 μm
Height	80 μm	80 μm	80 μm	80 μm
Line width	4 μm	4 μm	4 μm	4 μm
Pore size	15 μm	15 μm	15 μm	15 μm -30 μm
Enclosed volume	783,744 μm^3	998,400 μm^3	267,947 μm^3	308,976 μm^3
Surface area	117,564 μm^2	138464 μm^2	33039 μm^2	51816 μm^2
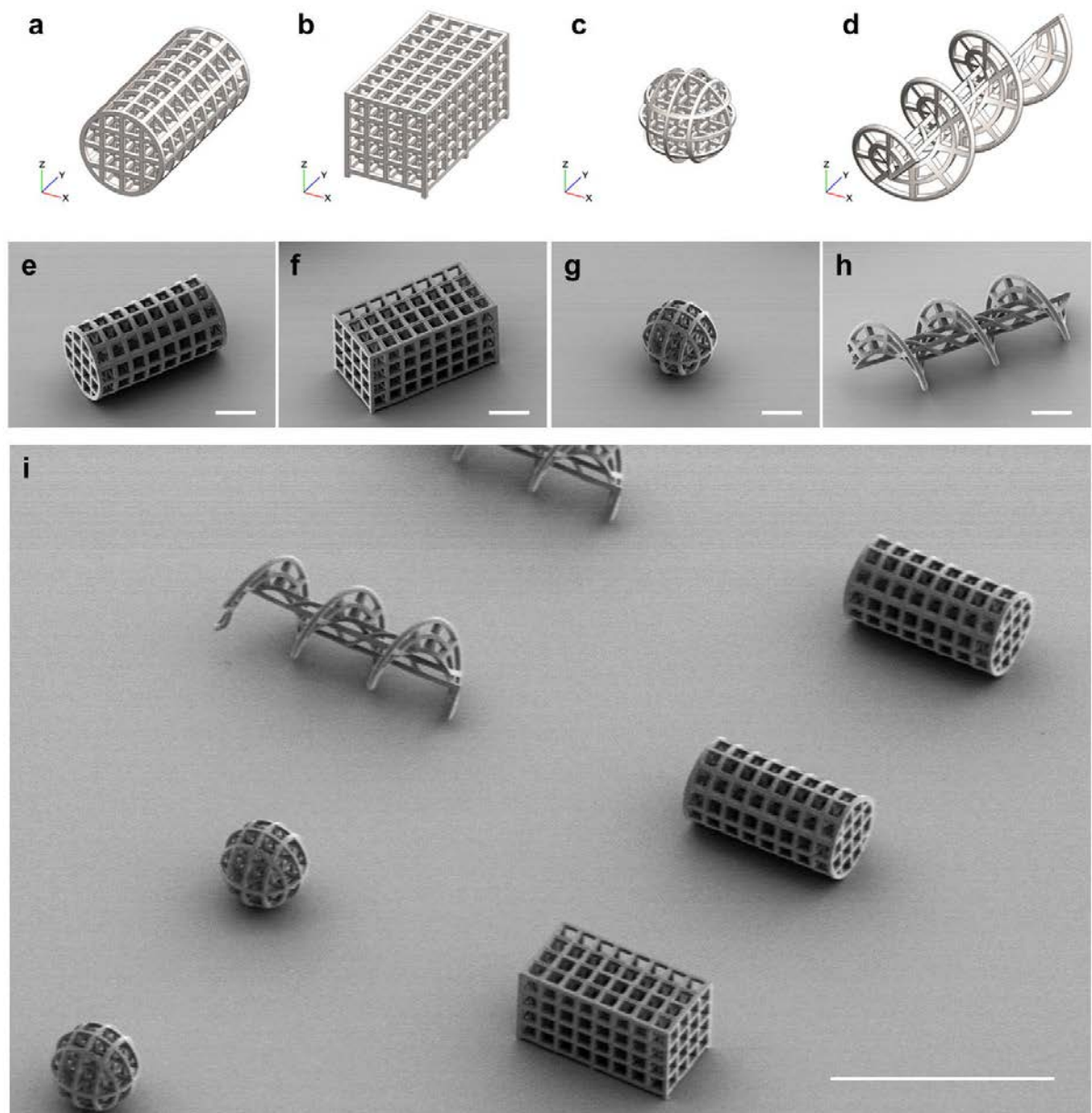
Figure 2.12 CAD layouts of four kinds of scaffold type microrobots, and SEM images after fabrication of scaffold type microrobots. CAD layout of (a) cylindrical, (b) hexahedral, (c) spherical, and (d) helical scaffold type microrobot. SEM images of fabricated (a) cylindrical, (b) hexahedral, (c) spherical, (d) helical (scale bar is 40 μm for each microrobots, and scaffold type microrobots array (scale bar is 200 μm for array) [28].

2.3 Design and fabrication of ciliary microrobots with higher propulsion efficiencies

For the ciliary microrobots, the overall fabrication process is exactly the same as the scaffold type microrobots by Dill technique. Figure 2.13 shows the CAD layout of the ciliary microrobot. The shape of ciliary microrobots were inspired by Paramecium, which is the microorganisms using ciliary stroke motion. The four cilia were attached on the each left and right side of ellipsoidal body, and the mask structures were also designed to prevent the metal layers deposition on the body parts. Figure 2.14 shows the overall fabrication processes for ciliary microrobots and detailed fabrication procedures are explained in the section 2.2. The body parts of the microrobots were not deposited by nickel because of the mask structures.

Figure 2.13 CAD layouts of ciliary microrobots. (a) bottom view, (b) side view, (c) 3D view with mask structure, (d) 3D view without mask structure [43].
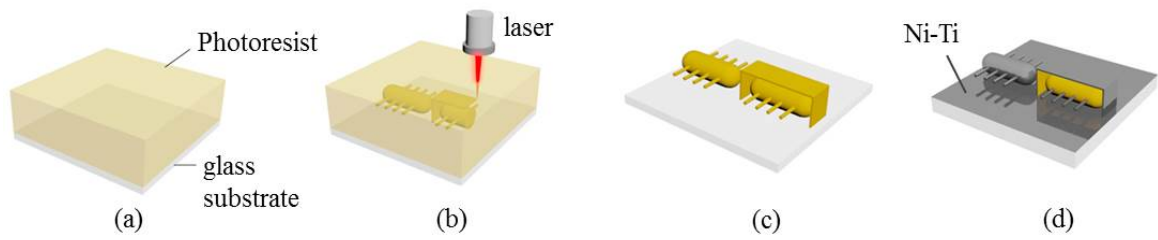
Figure 2.14 overall fabrication processes for ciliary microrobots [43].
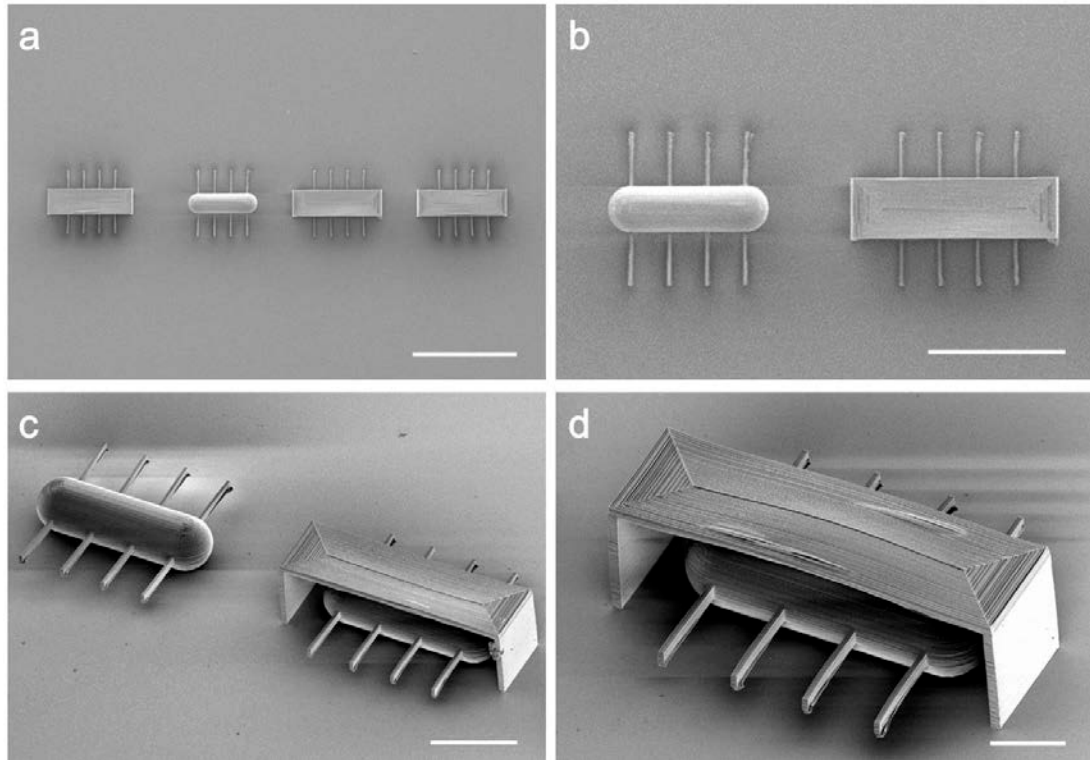
Figure 2.15 SEM images of fabricated ciliary microrobots. (a) Top view of four ciliary microrobots (scale bar = 300 µm), (b) Top view of two ciliary microrobots (scale bar = 200 µm), (c) 3D view of two ciliary microrobots (scale bar = 100 µm), (d) 3D view of a ciliary microrobot [43].

For the ciliary microrobots, the overall fabrication process is exactly the same as the scaffold type microrobots by Dill technique. Figure 2.13 shows the CAD layout of the ciliary microrobot. The shape of ciliary microrobots were inspired by Paramecium, which is the microorganisms using ciliary stroke motion. The four cilia were attached on the each left and right side of ellipsoidal body, and the mask structures were also designed to prevent the metal layers deposition on the body parts. Figure 2.14 shows the overall fabrication processes for

ciliary microrobots and detailed fabrication procedures are explained in the section 2.2. The body parts of the microrobots were not deposited by nickel because of the mask structures. Figure 2.15 shows the SEM images of fabricated ciliary microrobots with and without mask structures.

2.4 Design and fabrication of microfluidic channels as *in-vitro* test platforms

For the manipulation test for microrobots in the confined environments, PDMS (Polydimethylsiloxane) based microfluidic channels were fabricated. PDMS is the silicon based organic polymer which is widely used for prototyping of microfluidic channels. PDMS is transparent, bio-inert, non-toxic, non-flammable, and easy to cure. Microfluidic channels were designed including the curved shape which slope angle is about 00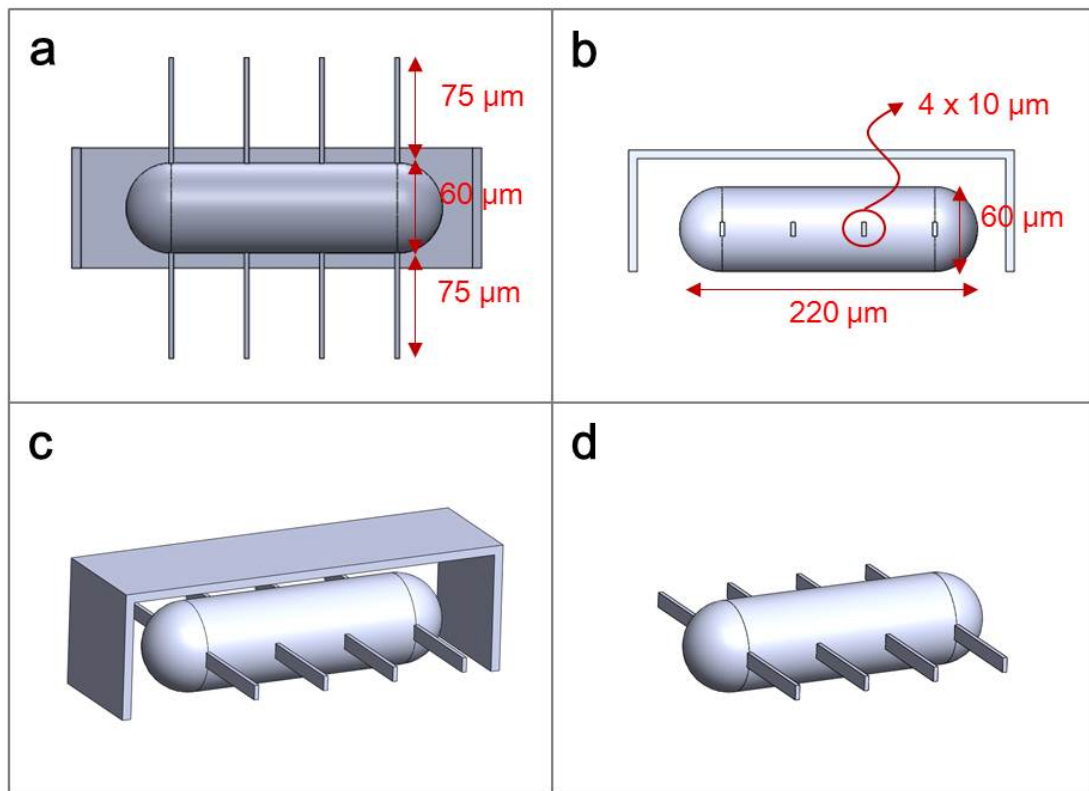 degrees from horizontal line. Figure 2.16 shows the channel design layout which was designed by CAD software (AutoCAD, Autodesk, USA). Microrobots are introduced into the microrobot loading port and this port will be closed, then microrobots are moves in the curved fluidic channel. Filter structures prevent for microrobots to escape the channel. Microfluidic channels were fabricated by general PDMS channel fabrication method indicated in Figure 2.17. A 4-inch silicon wafer was used for SU-8 coating on the wafer with a spin coater at 3000 rpm for 30 s to achieve a thickness of 150 μm (Figure 2.17(a)). The wafer was then baked on a hot-plate for 5 min at 65°C and 30 min at 95°C. The photolithography was followed using a MA-8 mask aligner (SUSS MicroTec AG, Germany) with an I-line (365 nm) UV source at 700 mJ/cm^2 (Figure 2.17(b)). The wafer was then developed in the SU-8 developer for 20 min and 150 μm thick channel patterns were achieved as a mold (Figure 2.16(c)). The PDMS elastomer (Silgard 184, Dow Corning, USA) was poured on the mold in a square dish, bubbles in the PDMS were removed in a vacuum chamber, and it was cured in an oven for 3 h at 70°C (Figure 2.17(d)). The cured PDMS was released (Figure 2.17(e)) and attached on a glass slide after oxygen plasma treatment with plasma equipment (Femto Science, Korea) after punching of inlet and outlet holes (Figure 2.17(f)). The microfluidic

channel with a height of 150 μm was ready for microrobot manipulation. Figure 2.17 is the

fabricated PDMS microfluidic channel.
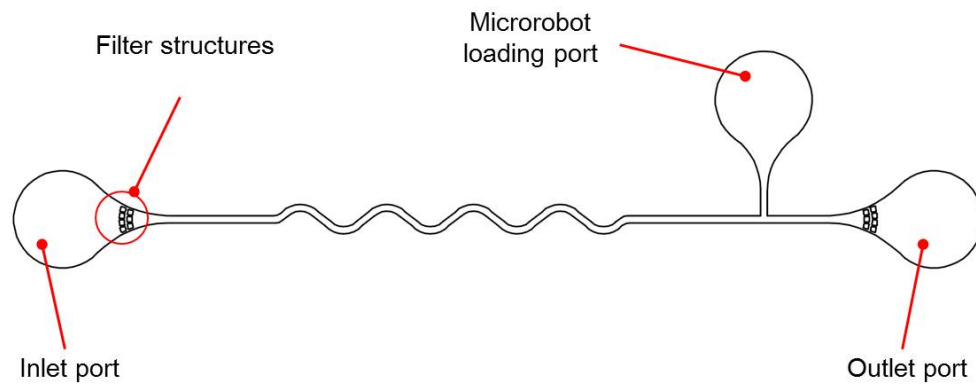
Figure 2.16 Design layouts for microfluidic channel.
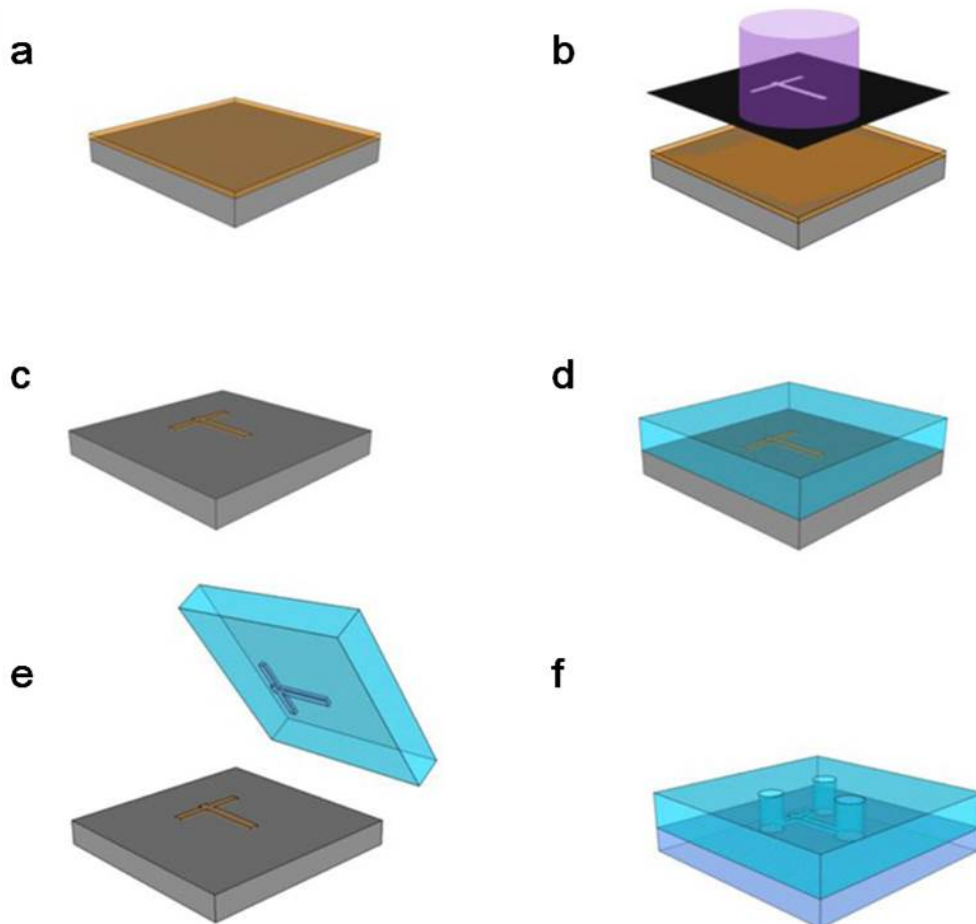
Figure 2.17 Fabrication processes for microfluidic channel with PDMS [89]
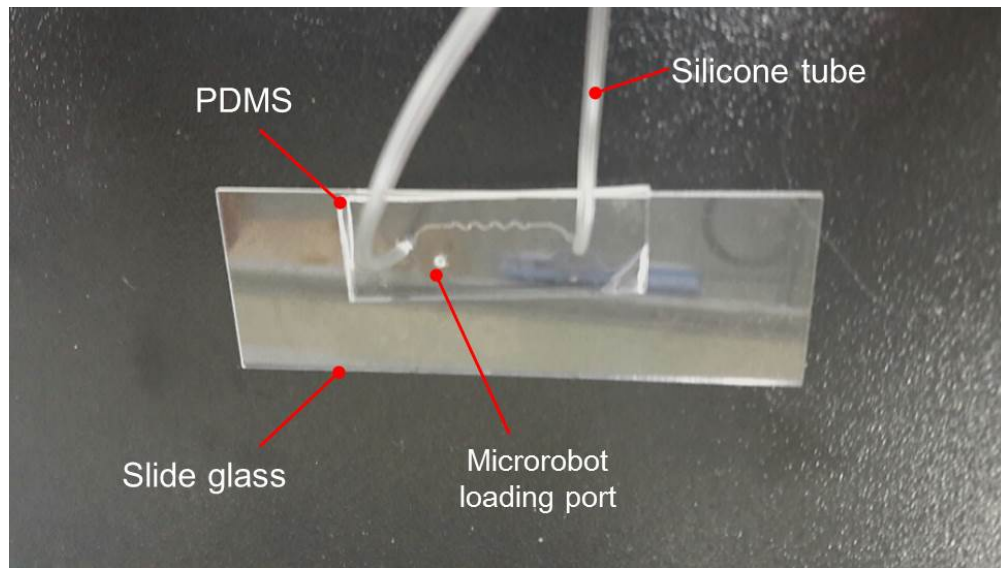
Figure 2.18 Picture of fabricated PDMS microfluidic channel with curves.

3. MAGNETIC MANIPULATION OF MICROROBOTS

3.1 Magnetic manipulation of magnetic materials

A hemispherical-configured magnetic manipulator (Minimag, Aeon Scientific, GmbH, Switzerland) with eight coils was used for the magnetic manipulation of the microrobots with a constant magnetic field and a rotating field in 3D space (with field intensity B and a field gradient ∇B) [33]. Figure 3.1 shows the image of the magnetic manipulator, Minimag, and the Figure 3.4 shows an image of the whole experimental setup for the electromagnetic manipulator, top camera, side camera for recording, and a light source.
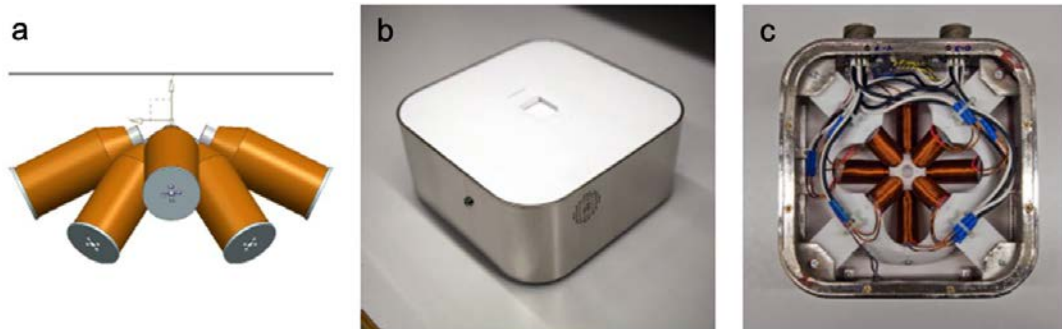
Figure 3.1 Magnetic manipulator with eight electromagnetic coils. (a) the schematic view of coils configuration inside of the manipulator, (b) picture of magnetic manipulator, (c) picture of inside of magnetic manipulator [45]
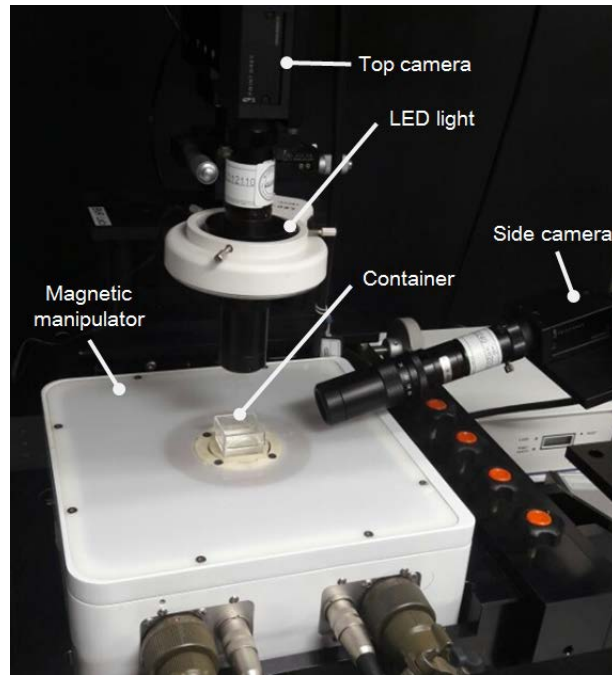
Figure 3.2 image of the whole experimental setup for microrobot manipulation [28].

The magnetic field was generated by the linear superposition of individual fields from eight coils carrying different currents.

3.2 Pulling motion with scaffold type microrobots

In this system, the magnetic field was generated by the linear superposition of individual fields from eight coils carrying different currents.[38] The microrobot was controlled in deionized (DI) water in a plastic container, with five degrees of freedom (5-DOF): three translational (x, y, z) DOF, and two rotational (around the z-axis and x-axis) DOF. Rotational and translational locomotion of the microrobot require a magnetic torque and force on the magnetized structure. The magnetic material on the surface of an anisotropic structure induces rotational motion, and the structure aligns with the external magnetic field ($\boldsymbol{B}$) direction. Magnetic torque and force can be calculated using the magnetic field ($\boldsymbol{B}$) and magnetic field gradient ($\nabla\boldsymbol{B}$) as Equation 4, and 5. Table 3.1 shows the Parameters and properties for cylindrical and hexahedral shape of scaffold type microrobots for force calculation. Figure 3.3 shows the calculated magnetic force under the applied magnetic field gradient, which range of 100 mT/m to 800 mT/m is almost full range for magnetic manipulator. The calculated results are driven from the Equation 4, and 5.

Table 3.1. Parameters and properties for cylindrical and hexahedral shape of scaffold type microrobots for force calculation

	Cylinder (type B)		Hexahedron (type B′)	
Material	SU-8	Nickel	SU-8	Nickel
Density	1237 kg/m^3	8900 kg/m^3	1237 kg/m^3	8900 kg/m^3
Volume	155526 μm^3	24182 μm^3	207325 μm^3	30591 μm^3
Mass	1.92X10^{-10} kg	2.15X10^{-10} kg	2.56X10^{-10} kg	2.72X10^{-10} kg
Total mass	4.08×10^{-10} kg		5.28×10^{-10} kg	
Saturation magnetization	686 kA/m			
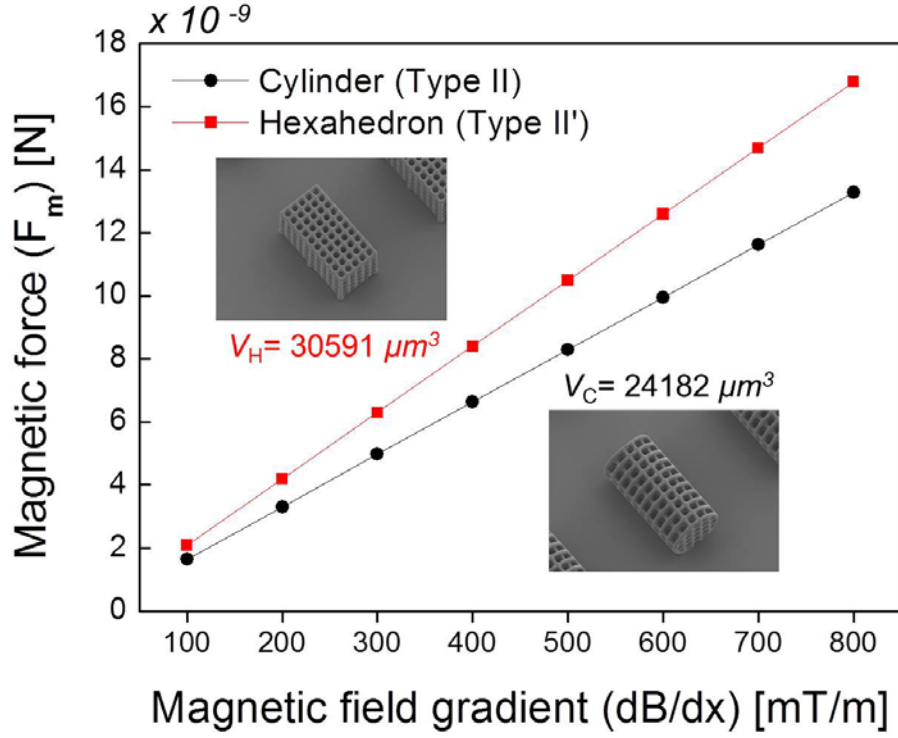
Figure 3.3 Calculated magnetic force under the applied magnetic field gradient for cylindrical and hexahedral shape of scaffold type microrobots, which range of 100 mT/m to 800 mT/m [88].
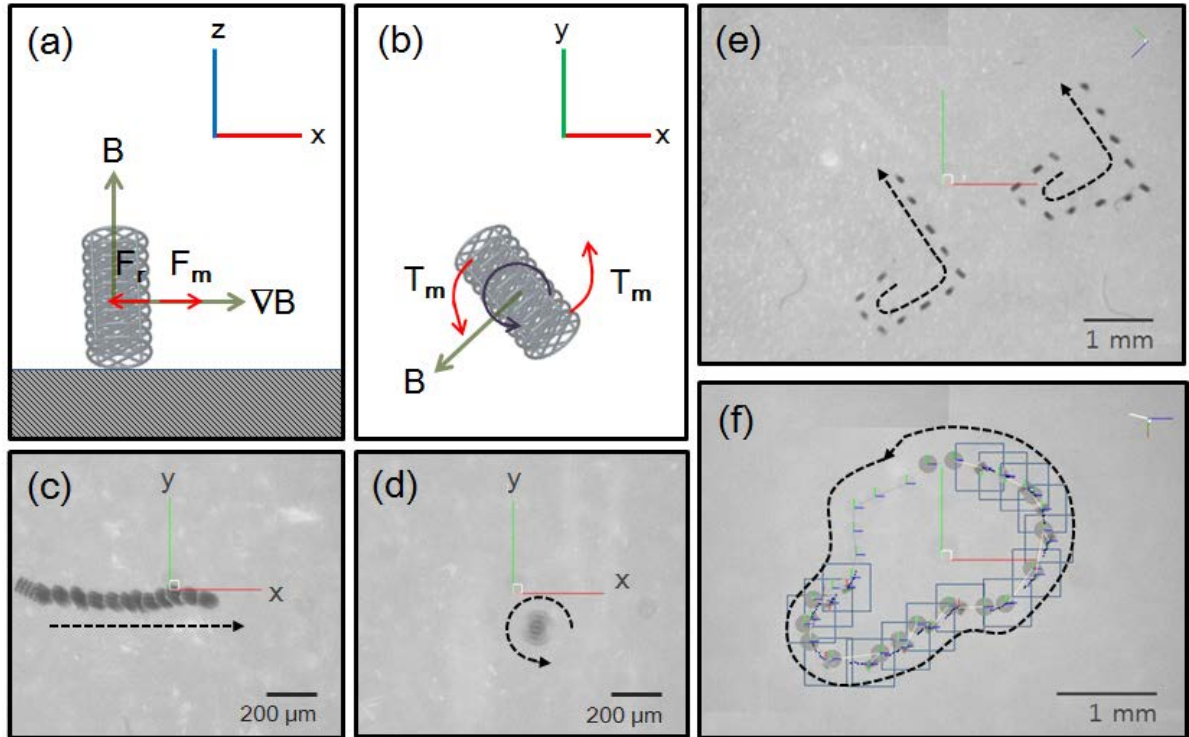
Figure 3.4 Various manipulation with the fabricated scaffold type microrobots. Schematic description of the cylindrical microrobot (a) translational motion and (b) rotational motion, Time-lapsed images of the cylindrical microrobot (c) translational motion and (d) rotational motion (e) Synchronized swimming with rolling motion, (f) Targeted control with rotational motion [88].

The position and the orientation of cylindrical and hexahedral shape of scaffold type microrobots could be controlled independently. We detached the microrobot from the glass substrate and put it in the container filled with DI water. The magnetic forces make microrobots to translate in the fluid. Figure 3.6 show the video images for microrobots with various control. Cylindrical microrobot translates along with x-axis by magnetic field gradient, and the orientation is aligned in z-direction (Figure 3.6(a, c)) by magnetic field. Microrobot rotates on the bottom surface with in-plane rotating by the rotating fields along with z-axis of rotating axis (Figure 3.6(b, d)) with a rotation frequency of 3 Hz. Two cylindrical microrobots rolls on the surface, which show the synchronized swimming (Figure 3.6 (e)) The rotation frequency for synchronized swimming was 4 Hz, the velocity of the rolling motion was 277 μm s^{-1} (1.85 body lengths per second); this was five times greater than the translational velocity by magnetic field gradient. Targeted position control with rotational motion was also demonstrated (Figure 3.6(f)) with 2 Hz of rotation field was applied to reduce the resistive force for targeted control. The translational velocities of the cylindrical and hexahedral microrobots were measured, which moves along with x-axis as a function of the applied magnetic field gradient from 100 to 800 mT/m. The microrobots were aligned with the *z*-direction such as Figure 3.6 (a, c). Figure 3.7 shows the results of translational velocities for cylindrical and hexahedral microrobots.

There are two resistive forces working against the motion of the microrobot: the drag force, and surface friction. For manipulation, the input magnetic force must overcome these resistive forces. A magnetic force in the *z*-direction was also required to compensate for the weight of the microrobot. The translational motion dynamics can be modeled as

$$\boldsymbol{F}_m + \boldsymbol{F}_r + \boldsymbol{F}_g = m\frac{dv}{dt} \qquad \text{equation (3.1)}$$

where F_m is the magnetic force, F_r is the resistive force (including the surface friction and drag force), F_g is the gravitational force, m is the mass, and v is the translational velocity of the microrobot.

When an external field gradient of 800 mT/m was applied in the x-direction, the translational velocity of the microrobot was approximately 50 µm/s for the cylindrical microrobot (~1/3 body lengths per second). The results showed a linear dependence of the required magnetic field gradient on the translational velocity for the cylindrical-shaped microrobots. However, for the hexahedral-shaped microrobots, the relationship between the translational velocity and input force was nonlinear.

Because the Reynolds number was low under these experimental conditions, we could consider microrobot motion to be quasi-static. For constant velocity motion in the *x*-direction, from Equation. 6, there is a balance between the magnetic force and the resistive force; there is no gravitational force in the horizontal direction. The resistive force consists of the drag force and the friction force. The drag force has a linear dependence on the microrobot velocity in a low-Reynolds number flow. Figure 3b indicates a higher velocity for a cylindrical microrobot when compared with a hexahedral microrobot for the same magnetic field gradient. For the hexahedral microrobot, a nonlinear relationship was evident between the translational velocity and the magnetic field gradient; this could be attributed to the nonlinear characteristics of the velocity and resistive force. Because the drag force is linear with respect to the velocity, the friction force plays a greater role in the nonlinear character of the hexahedral microrobot.

The surface area of the hexahedral microrobot was larger than that of the cylindrical microrobot. Because Ni was uniformly deposited on both of microrobot surfaces, the hexahedral microrobot had a larger volume of nickel. Therefore, the magnetic moment of the hexahedral microrobot was larger than that of the cylindrical microrobot, which implies a

higher magnetic force applied to the hexahedral microrobot for a specific magnetic field gradient (Equation.5 and Figure 3.4 (a)). However, the hexahedral microrobot exhibited a lower translational velocity, which may have been caused by a higher resistive force. Therefore, the cylindrical microrobot design is favorable for minimizing the resistive force against manipulation.
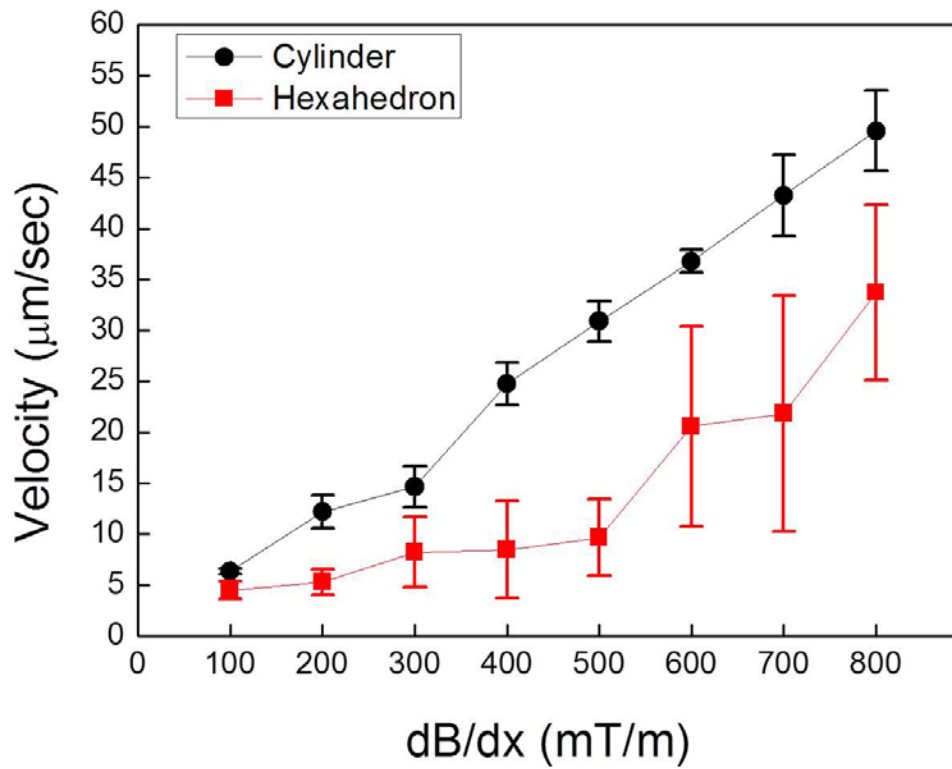
Figure 3.5 Translational velocities of the cylindrical and hexahedral microrobots in the *x*-direction as a function of the applied magnetic field gradient. The microrobots were aligned with the *z*-direction. (Note that these data correspond to Figures 3.6 (a, c) for the cylindrical robot.) [88].

3.3 Rolling and Corkscrew motion of scaffold type microrobots

For the higher propulsion efficiency in the low Reynolds number fluid environment, the effective motions are required as explained in the section 1.2.2. Scaffold microrobots with cylindrical and hexahedral shapes are using the pulling motion by magnetic field gradient, but this motion is based on the inertial force. Therefore it is very slow and hard for these bulky shapes of microrobots to overcome the drag force of the viscous fluid around the microrobots. Figure 3.6 shows the SEM images of the fabricated scaffold microrobots and their three propulsion mechanisms. The cylindrical and hexahedral shapes of microrobots (Figure 3.8(a, b)) are using the pulling motion by field gradient (∇B), (Figure 3.6(e), the helical microrobots (Figure 3.6(c)) move with Corkscrew motion by rotating magnetic field (B) (Figure 3.6(f)), and the spherical microrobots (Figure 3.6(d)) moves with rolling motion by rotating magnetic field (B) (Figure 3.6(g)).
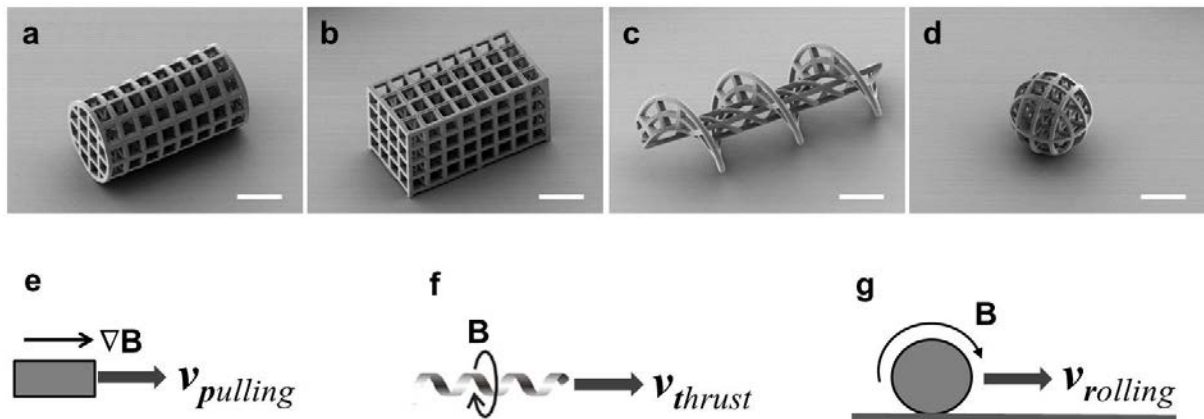
Figure 3.6 SEM images of the fabricated scaffold microrobots and their propulsion mechanisms [28].

Fabricated scaffold microrobots were manipulated in the DI water of the plastic container. Figure 3.7 shows the video clip images of fabricated microrobots. Cylindrical microrobot moves by pulling motion, microrobot is aligned in z-direction, and moves in x-direction. Hexahedral microrobot moves along with the designated targets, microrobot is aligned in x-direction, and moves in x-y plane. Helical microrobot moves by Corkscrew

motion. Spherical microrobot moves by rolling motion. The spherical microrobot has shape magnetic anisotropy due to the radially non-symmetrical design and non-uniform metal deposition by the sputtering system. Thus, it has a magnetic easy axis; the magnetic orientation has to be aligned with the external magnetic field to generate torque for rolling motion, although its shape appears spherical [56]. Figure 3.8 shows the results of measured velocities for manipulation of helical and spherical microrobots. The recorded videos were analyzed to determine the velocities of the microrobot at 15 frames/s. The velocities of these rotating microrobots are determined by the magnetic field rotating frequency and the field intensities, the translational velocities were measured under different magnetic field conditions. The step-out frequency (frequency limit above which the mechanical rotation of microrobots cannot follow the rotating magnetic field) was increased with an increasing applied field (Fig. 3.8). The translational velocity was increased as a function of the magnetic rotating frequency for both helical and spherical microrobots until the step-out frequencies with applied magnetic field intensities of 5, 10, and 15mT. The translation velocity of each microrobot is compared in Figure 3.9 as a function of the normalized input current. Normalized input currents were calculated with equation (3.2) with an acquisition rate of 1000 Hz, where I_1 to I_8 are the target currents for each coil.

$$I_{norm} = \sqrt{I_1 + I_2 + \cdots + I_8} \qquad \text{equation (3.2)}$$

When the normalized input current is 4.57 A, The velocity of the helical microrobots was 432.7 μm/s at 5 mT and 35 Hz (29.63 times faster than 14.6 μm/s of the cylindrical microrobot at 300 mT/m) and the velocity of the spherical microrobots was 686.0 μm/s at 5 mT and 20 Hz (46.98 times faster than the velocity of cylindrical microrobots).

The helical and spherical microrobots also showed precise position and orientation control by complex trajectory driving. Figure 3.10 is the stacked frame images show the complex trajectory driving for helical and spherical microrobots. "BMR" routes were driven

by each microrobot. This result indicates the developed microrobots can navigate precisely, with small number of radius of curvature on rotation.
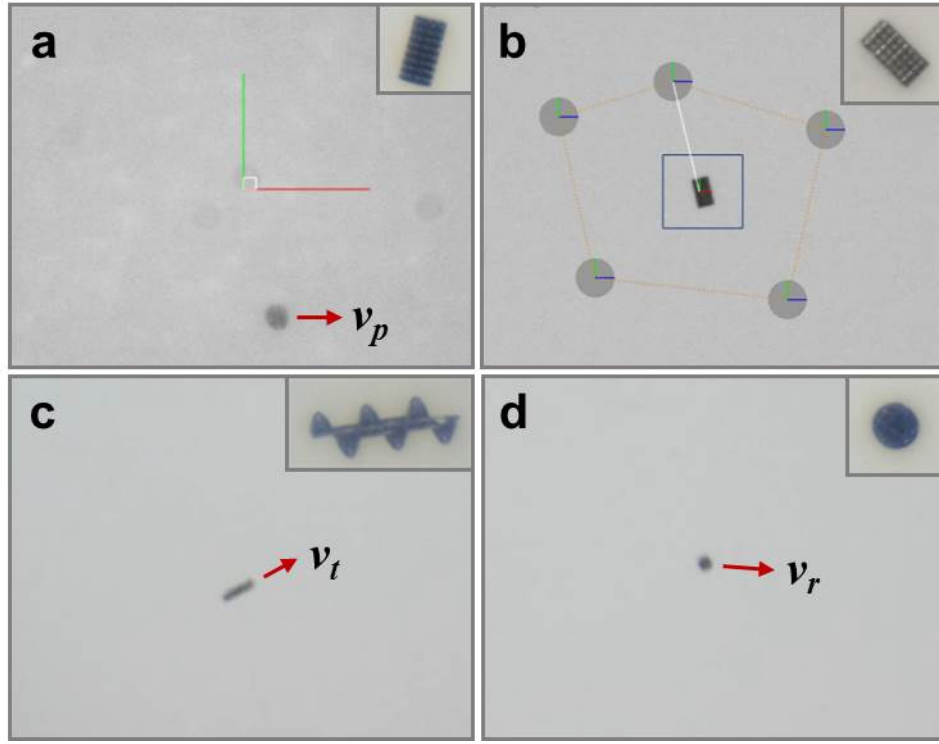
Figure 3.7 Magnetic manipulation of fabricated scaffold type microrobots. (a) Cylindrical microrobot moves by pulling motion, microrobot is aligned in z-direction, and moves in x-direction. (b) Hexahedral microrobot moves along with the designated targets, microrobot is aligned in x-direction, and moves in x-y plane. (c) Helical microrobot moves by Corkscrew motion. (d) Spherical microrobot moves by rolling motion [28].
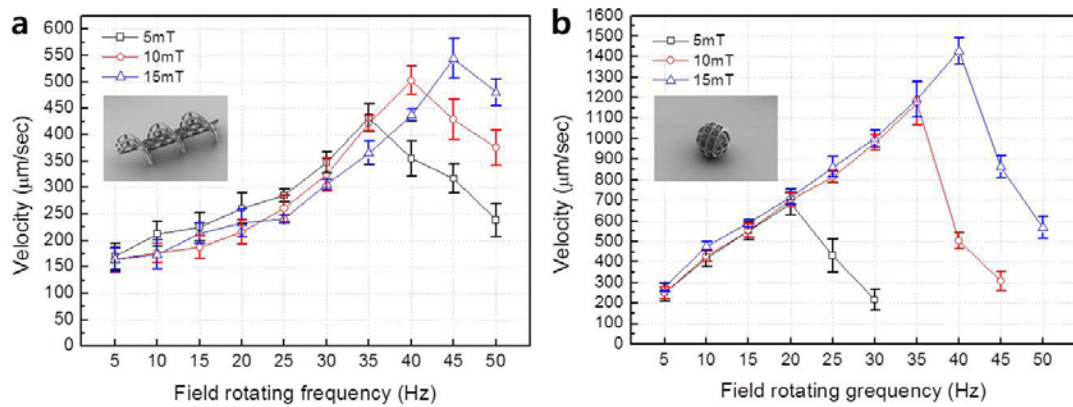
Figure 3.8 The velocities under external magnetic fields with rotating frequencies were measured for (a) helical and (b) spherical microrobots [28].
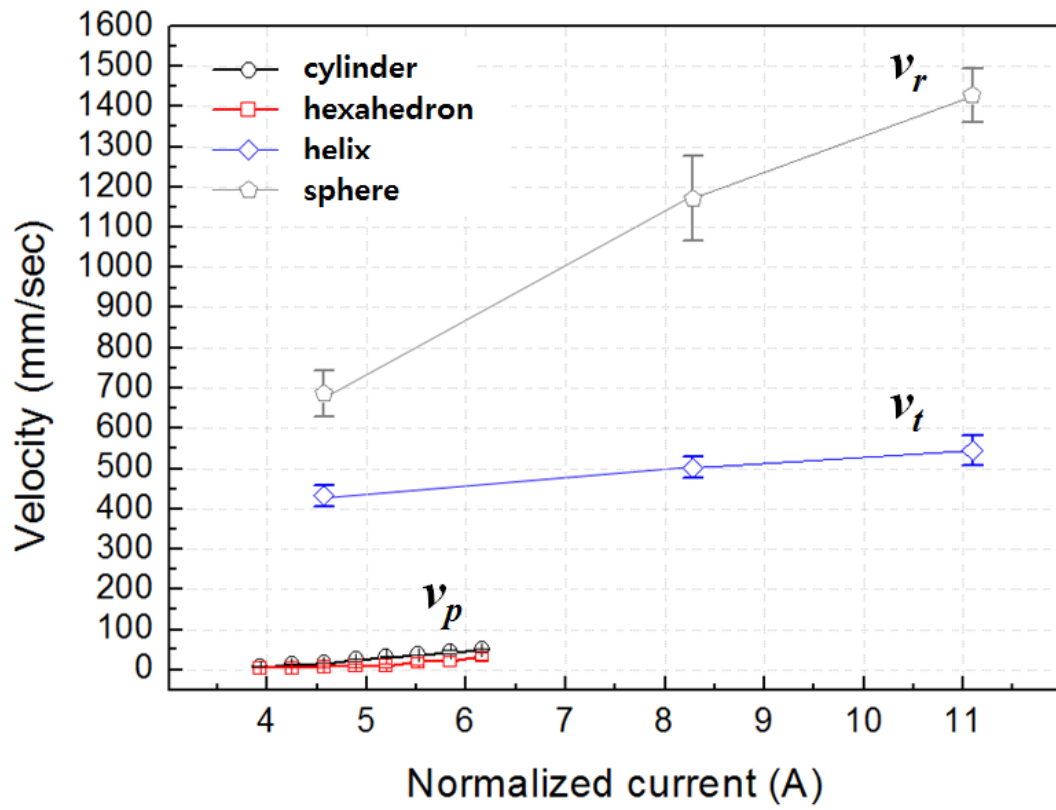
Figure 3.9 The velocities of the four different microrobots were measured and compared with respect to the normalized input current used to compare the propulsion efficiencies [28].
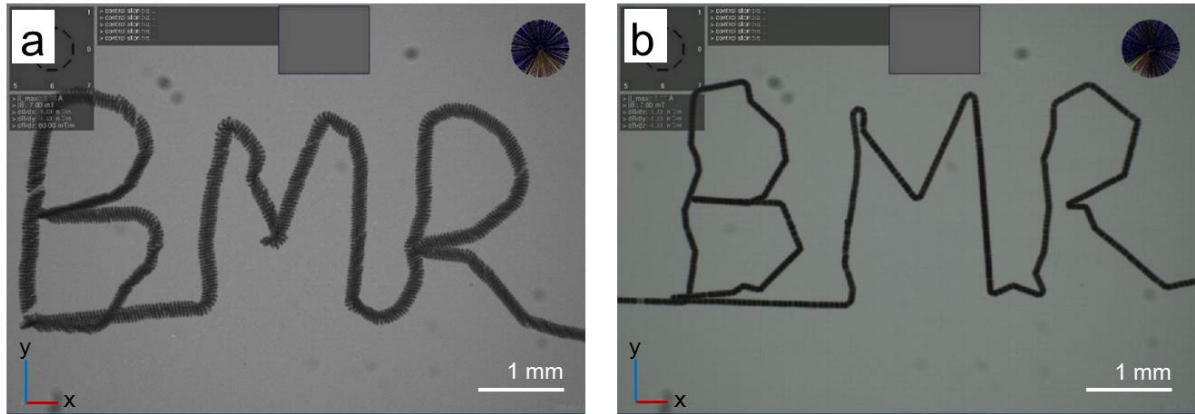
Figure 3.10 "BMR" routes driving demonstration. (a) Stacked frame images for helical microrobot which is manipulated with 7 mT, and 12 Hz. (b) Stacked frame images for helical microrobot which is manipulated with 6mT, and 10 Hz. These results show the precise manipulation of microrobots in the fluid [28].

Helical and spherical microrobots were manipulated by the magnetic manipulator following cell culture. The hippocampal NSCs were cultured on the surface of the microrobots following the protocol outlined in the online Supplementary methods. The motion of the helical microrobots was changed from the corkscrew motion to the tumbling motion with a decrease in microrobot velocities. Figure 3.11 show the magnetic manipulation of the microrobots with hippocampal NSCs cultured on them. The positions and orientations were controlled, but the controllability and the translational velocities were less than those of the original shapes of the microrobots. The helical microrobot was exposed to a 30 Hz rotating magnetic field with 9 mT. Tumbling occurred due to the changes in microrobot envelope shape and resulted in cell entanglement. The microrobot position and orientation were controlled. The video was captured in real time at 2X magnification. Magnetic manipulation of the spherical microrobot that rolled due to the rotating field, with rotating axis steering. The rotating frequency varied from 10 to 50 Hz and the magnetic field intensity was 7 to 9 mT. The translational velocity was decreased due to the increased overall mass, drag force, and friction due to cell attachment of the microrobot. The translational velocity was 280 μm/s with the 10 Hz of step-out frequency, which is less than half of the velocity without hippocampal NSCs. The video was captured in real time at 2X magnification.
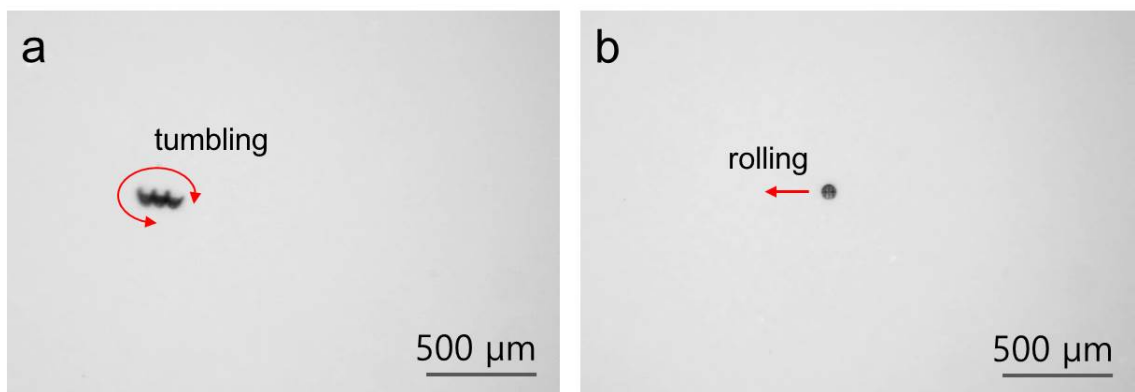
Figure 3.11 Helical and spherical microrobots manipulation with cell cultured microrobots. (a) the helical microrobot moves not with Corkscrew motion but with tumbling motion, and (b) the spherical microrobot moves with rolling motion normally.

3.4 Stroke motion with ciliary microrobots

Manipulation of the microrobots was conducted with a same magnetic manipulator. [45] This system also can apply stepping fields for translation of the ciliary microrobot, and can tilt the reference axis of the stepping fields to change the orientation of the microrobot as well. Figure 3.12 shows the principle of ciliary microrobot actuation for the generation of net displacement by the non-axial symmetric beating motion of the cilia. The cilium moves in 3D space by the external stepping fields; beating on backward and upward trajectory. We calculated the x-y planar force components of the generated force by a cilium because it is the net force contributed for translation. Therefore, the cilium angle (θ) and magnetic force (F) are projected components on the x-y plane. The relationships among the applied magnetic field direction (γ), cilium angle (θ), and magnetic force (F) can be calculated by a simple cantilever deflection method and the calculated results are shown in Figure 3.13.
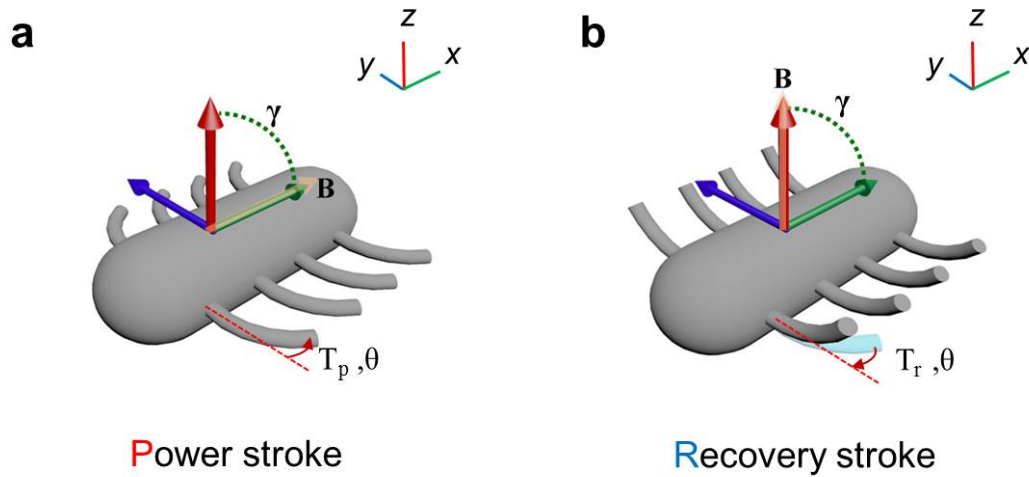
Figure 3.12 the principle of ciliary microrobot actuation for the generation of net displacement by the non-axial symmetric beating motion of the cilia [43].

The cilia beating cycle generates net translational force due to the difference in the magnetic actuation force between the power stroke and the recovery stroke. The cilium angle (θ), and magnetic force (F) are projected on the x-y plane to calculate the in-plane translational force of the ciliary microrobot. When an external magnetic field is applied along

the long axis of the microrobot body with magnetic field at angle γ, the cilia are bent, as shown in Figure 3.13(a) with cilium angle θ. The applied field direction is 0° for the recovery stroke stage, and a force is generated due to the difference between the maximum cilium angle and 0°. We assume the cilium angle is 0° after one beating cycle to calculate the actuation force. Magnetic torque ($\mathbf{T}_m$) of a cilium with an external magnetic field can be explained by Equation. (3.3).

$$\mathbf{T}_m = \mathbf{m} \times \mathbf{B}$$
equation (3.3)

where $\mathbf{m}$ is the magnetic moment of a cilium, and $\mathbf{B}$ is the magnetic field intensity, which has a maximum value when the field is applied orthogonally to the magnetic moment direction. The equation for the magnetic force on a cilium in the longitudinal axis of the cilium body can be simplified during the backward (power) and forward (recovery) strokes to the following equation if the cilium length is L, the applied field angle of γ, and actual cilium angle is θ: [90]

$$F_m = mB\sin(\gamma - \theta)/L$$
equation (3.4)

Only the planar (x-y plane) force components are counted in this calculation, and this affects only body translation along the x-direction. The cilium angle is evaluated by a simple cantilever deflection model, as follows:

$$\theta = TL/EI = mB\sin(\gamma - \theta)L/EI$$
equation (3.5)

where T is magnetic torque of the planar component of the ciliary microrobot, E is Young's modulus of the cilium, and the I is the moment of inertia. Relationships among the applied magnetic field direction (γ), cilium angle (θ), and magnetic force (F) were calculated with geometrical parameters and material properties are listed in Table 1. Figure 3.13 show the relationships among the applied magnetic field direction (γ), cilium angle (θ), and magnetic force (F). Figure 3.14 also present the temporal working mechanisms in one beating cycle explained in the Figure 3.13 in detail.
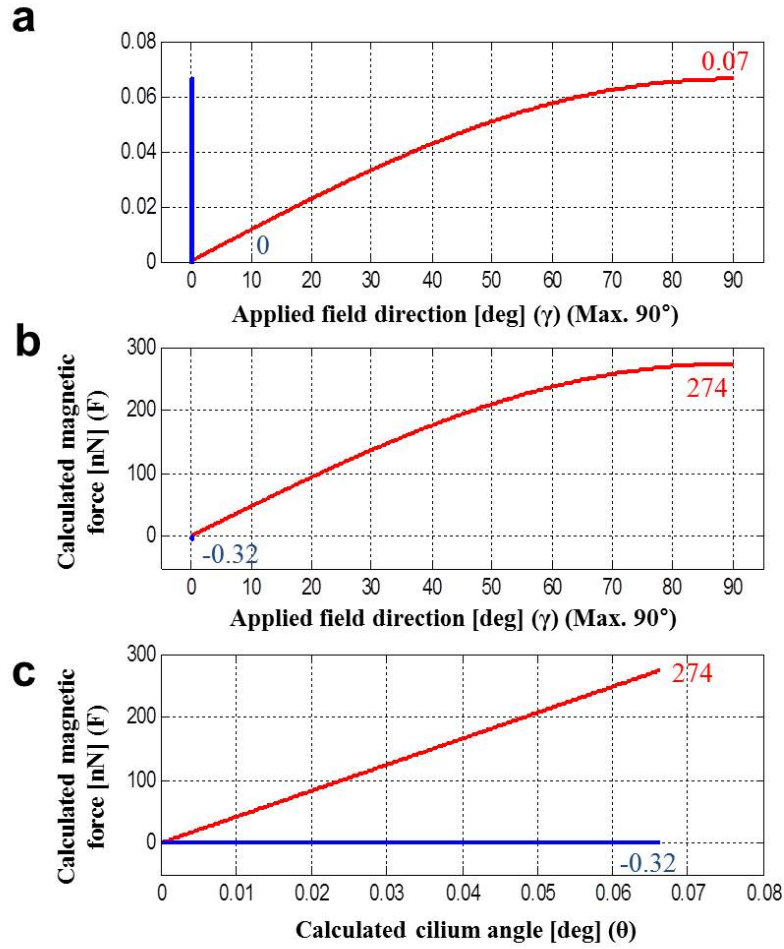
Figure 3.13 Calculated cilium angle and magnetic forces [43]..

The maximum force for the power stroke is 274.40 nN at 0.07° of cilium angle (θ), and the maximum force for the recovery stroke is 0.32 nN at 0° of cilium angle (θ) in the opposite direction to the power stroke. During the power stroke and recovery stroke stages, the angles of the cilium angle (θ) and the applied magnetic field direction (γ) are almost 90° and 0°, respectively; thus, a magnetic torque difference occurs, as expected, due to equation (3.3), This force difference causes non-reciprocal actuation, which is similar to the actual beating behavior of a cilium. [67]
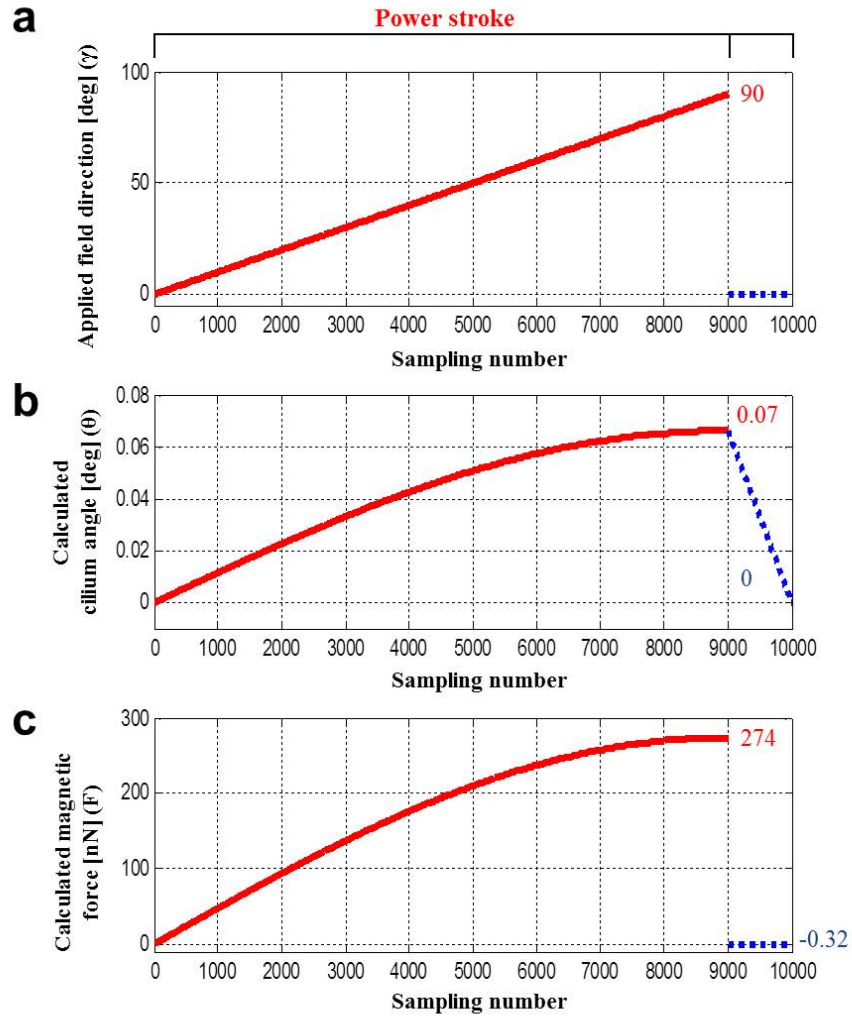
Figure 3.14 Calculated cilium angle and magnetic forces along with sampling number [43].

Figure 3.15 shows time lapse images of position and orientation control for a ciliary microrobot. The stepping fields were applied at 0-110° to change the polar angle for translation, and the azimuthal angle (φ) was changed for rotation. Non-symmetric on and off of the magnetic fields in the range of a 110° angle in the polar angle direction was used to move the cilia with non-axial symmetric actuation forces because the cilia tend to align with the applied magnetic field direction for stroke motion. The steering axis (azimuthal angle) can also be changed to control the orientation of the microrobots. The reference axis of

oscillating stepping field can be changed within the azimuthal angle to change the orientation of the ciliary microrobot. Therefore, the position and orientation can independently and precisely be controlled at any time. The stepping angle was tuned for the best controllability at 110° in an actual experiment. However, this does not mean the cilia are actually moving in this range of angle. Because of the bending stiffness of the cilia, the cilia actually move much less than the applied oscillating angle, as in the calculated results with equation (11), shown in Figure 3.14(b, c).
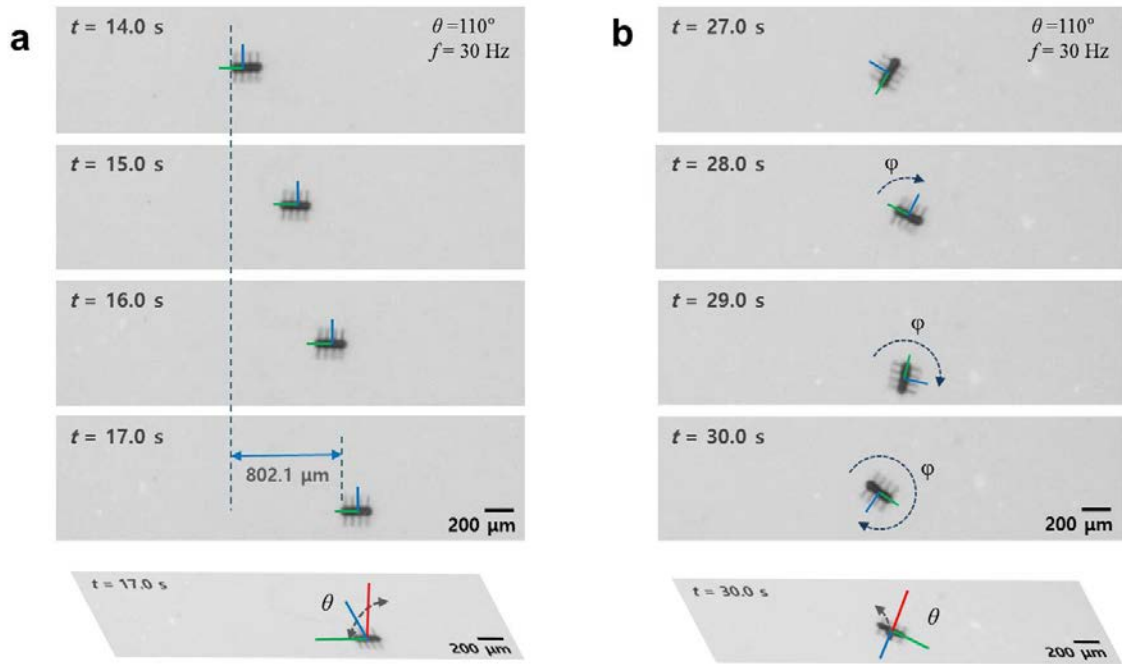
Figure 3.15 Time lapse images of position and orientation control for a ciliary microrobot. (a) position control of microrobot, and (b) orientation control of microrobot [43].

Figure 3.16 shows the manipulation of microrobot, which drives along with each letter of "DGIST", the five videos are merged. This result shows the precise position and orientation control for developed microrobots. The translational velocity of ciliary microrobots can be changed by controlling the frequency and the external magnetic field intensity. Figure 3.17 shows the measured velocities of the microrobots under different magnetic frequencies and magnetic field intensities in DI water. The maximum average velocity of the microrobots in

DI water was 340 μms^{-1} (1.55 body lengths per second) under both 9.5 mT and 12 mT field intensities at 60 Hz of frequency; this is the saturated velocity. Figure 3.18 is the measured velocities of the microrobots under different magnetic frequencies and magnetic field intensities in 10 CS of silicon oil. The maximum average velocity of the microrobots in DI water was 165 μms^{-1} (0.75 body lengths per second) under 12 mT field intensities at 45 Hz of frequency. The maximum velocity of the microrobots and the step-out frequencies are reduced in the silicon oil due to the higher drag forces than DI water. Figure 3.18 shows the microrobot velocities in comparison with the previously developed scaffold type microrobots. Magnetic field gradient was used for translational motion of cylindrical and hexahedral microrobots. The velocities are shown as function of the normalized applied current in the eight electromagnetic coils of the magnetic control system. Therefore, these results could be implied as the propulsion efficiency of each microrobot. The velocity for ciliary microrobot is 233 μms^{-1}, which is about 8.6 times and 25.8 times faster than cylindrical and hexahedral microrobots, respectively, when the normalized current is 5.09 A, which is indicated by the blue dashed line in the Figure 3.19. Therefore, the translational motion of the ciliary microrobots is much more efficient than the previously reported cylindrical and hexahedral microrobots while the three microrobots have a similar characteristic body length. (150 μm for cylindrical and hexahedral types of microrobots in the previous work [10], and 220 μm for ciliary microrobots reported in this paper) In Figure 3.20, the translational velocities per each microrobot body length results is shown. The velocities, measured from Figure 3.19 were divided into the each body lengths to compare their velocities directly. When the ciliary microrobot moved following a circular pass, the starting and ending points were deviated about 200 μm which is smaller than the body length. In the Figure 3.21, the targeted particle transportation by the ciliary microrobot was demonstrated by a micro-particle with 80 μm diameter. The micro-particle was pulled by the microrobot for the translation, and it was

released by the rotational motion of the microrobot. The applied field intensity was a 12 mT and 35 Hz stepping field with a stepping angle of 110°.
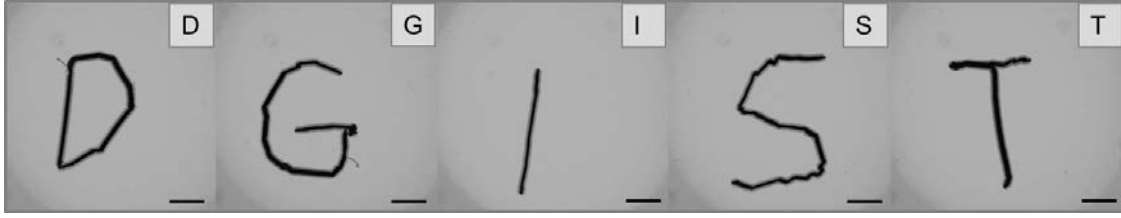
Figure 3.16 The microrobot was driven to write each letter of "DGIST". The image is acquired by superposing each image from the video for each letter. The applied field intensity was a 8 mT and 35 Hz stepping field with a stepping angle of 110°. The scale bar is 1000 µm [43].
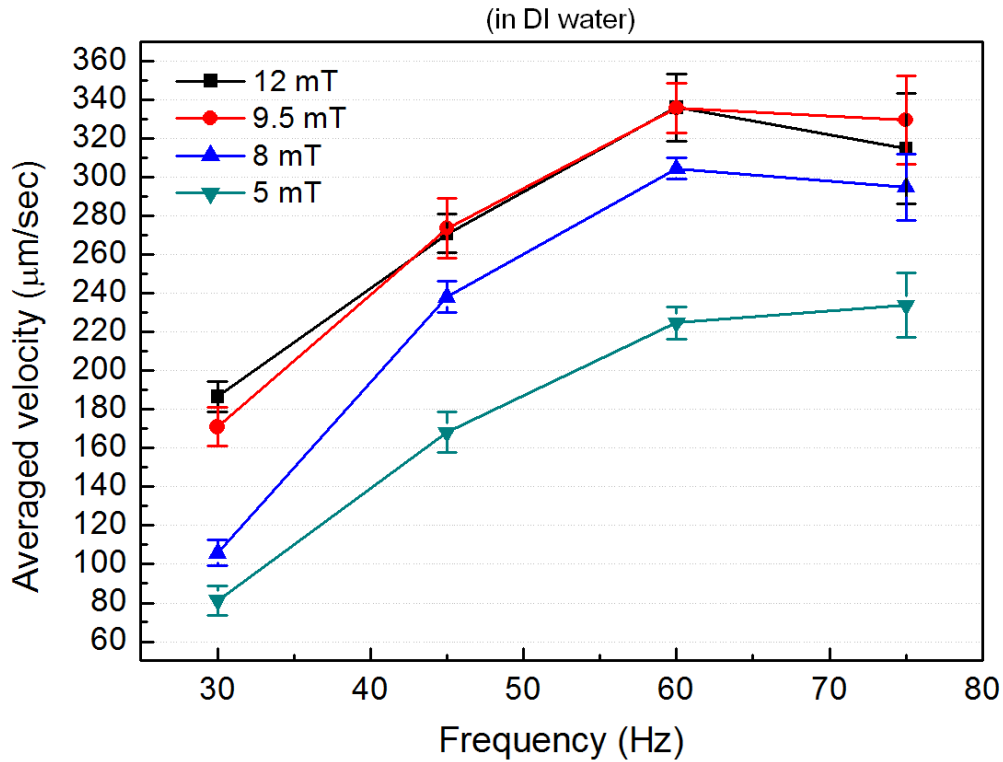
Figure 3.17 Averaged velocities ($n = 3$) of the ciliary microrobots manipulated in DI water under different magnetic frequencies and magnetic field intensities [43].

For the magnetic control of microrobots with cilia beating, the metal sputtering system was used to deposit the nickel and titanium layers on the only cilia parts by using the mask structures. Sputtering is conformal coating and we have the shadow structure which is very close to the ciliary microrobot. Because of the shadow structure, there will be considerably small amount of metal on the body of the microrobot. Magnetic field gradient was applied to

pull the microrobots but the robots didn't move at all. This means that the total amount of magnetic material is not enough to generate magnetic force to translate the whole body by magnetic pulling using magnetic field gradient at 1000 mT/m. This shows that there is no or very small amount of the magnetic material on the body of the microrobot.
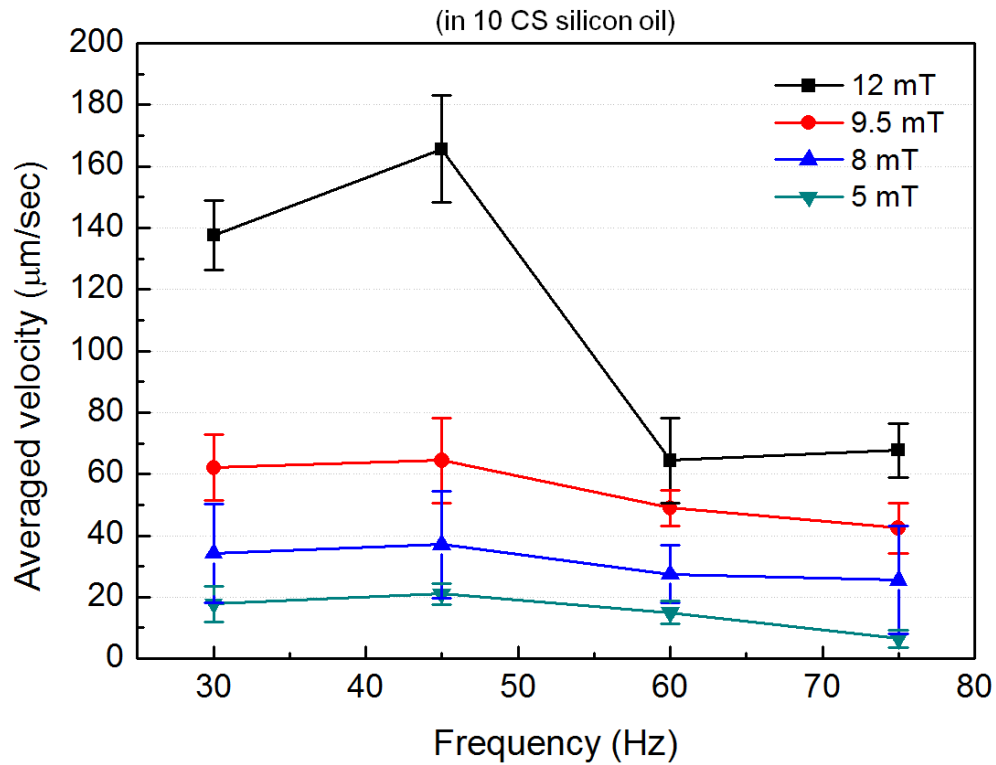
Figure 3.18 Averaged velocities ($n = 3$) of the ciliary microrobots manipulated in 10 CS of silicon oil under different magnetic frequencies and magnetic field intensities [43].
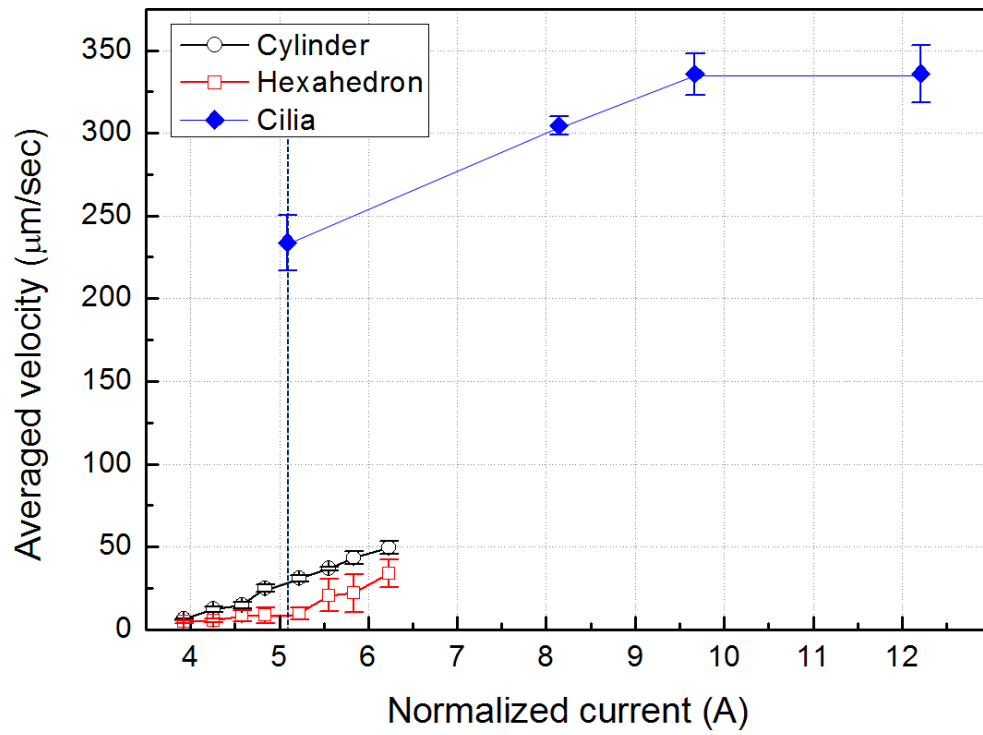
Figure 3.19 The microrobot velocities in comparison with the previously developed scaffold type microrobots [43].
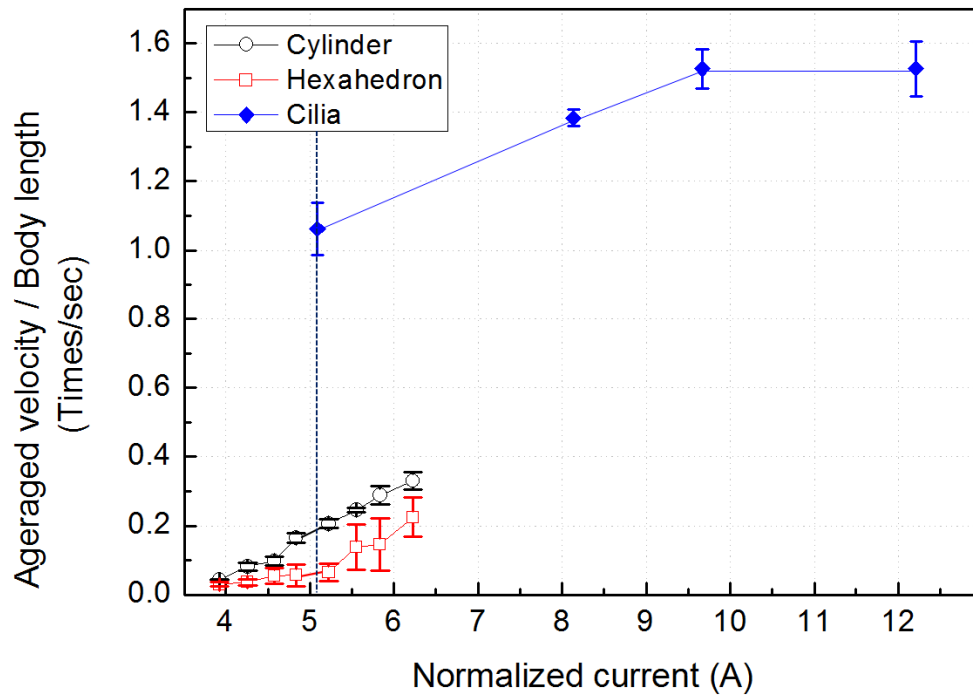
Figure 3.20 The microrobot velocities per each microrobot body length results manipulated in DI water [43].

71
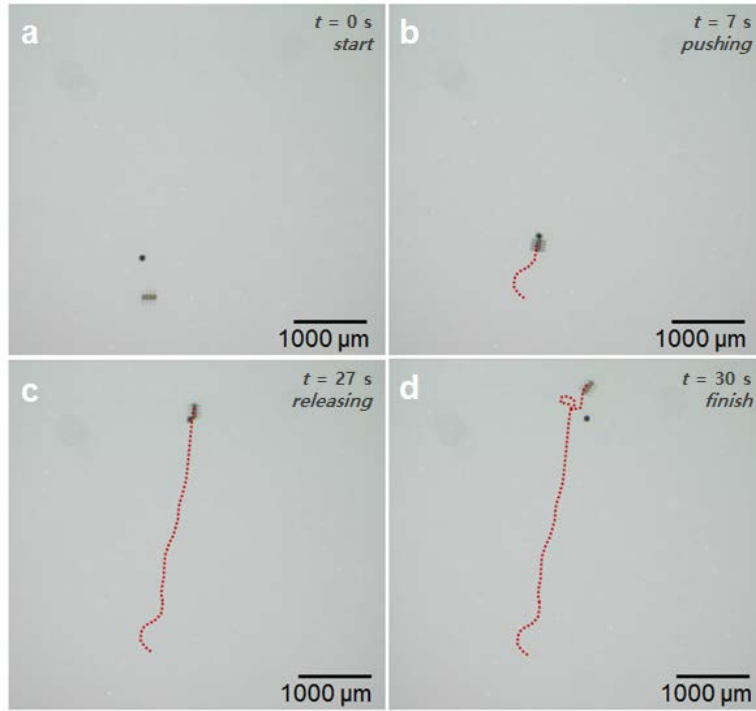
Figure 3.21 Time lapse images for targeted micro-particle transportation with ciliary microrobot. (a) Microrobot starts and change the orientation to catch the micro-particle on the front side, and (b) microrobot pushed the micro-particle with translational motion. (c) Microrobot rotates back and forth to release the micro-particle, and (d) finally microrobot moved away from the micro-particle. The diameter of microsphere is 80 μm. The diameter of the micro-particle is 80 μm. The applied field intensity is 12 mT and 35 Hz stepping field with a stepping angle of 110° [43].

3.5 Manipulation of microrobots in the microfluidic channels

3.5.1 Manipulation in the static fluidic channel

Developed microrobots were manipulated in the microfluidic channels. We tested the manipulation of the spherical and helical microrobots in a microfluidic channel that mimics a physiological confined environment. Figure 3.21 shows the manipulation of the spherical microrobot in a 200 μm wide microfluidic channel with planar and vertical configuration. The channel was also placed vertically so that the microrobot had to climb the slopes in the *z*-direction as well as planar motion. The spherical microrobot successfully rolled up, showing the possibility of manipulating a microrobot in a confined environment with a slope, overcoming the friction force on a small scale. Helical microrobots also operated in the microfluidic channel using Corkscrew motion. Figure 3.22 shows the manipulation of the helical microrobot in a 200 μm wide microfluidic channel with planar configuration.
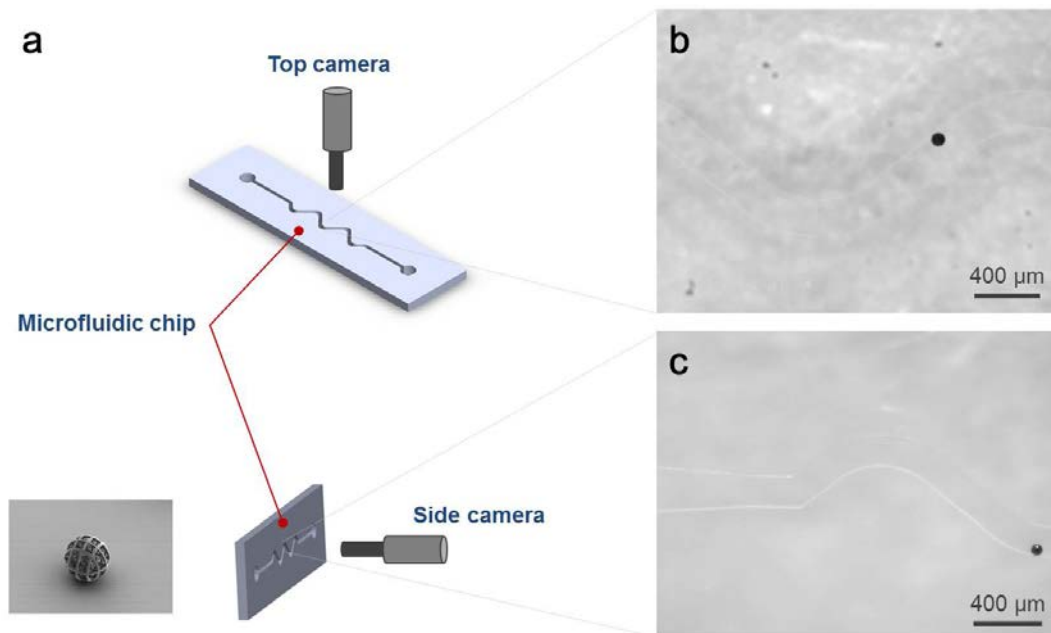
Figure 3.22 Video captured images for spherical microrobots with planar and vertical channel configurations. (a) The schematic images of channel configuration with camera position as well as image of spherical microrobot, (b) manipulation of microrobot in the planar placed channel, (c) manipulation of microrobot in the vertically placed channel.
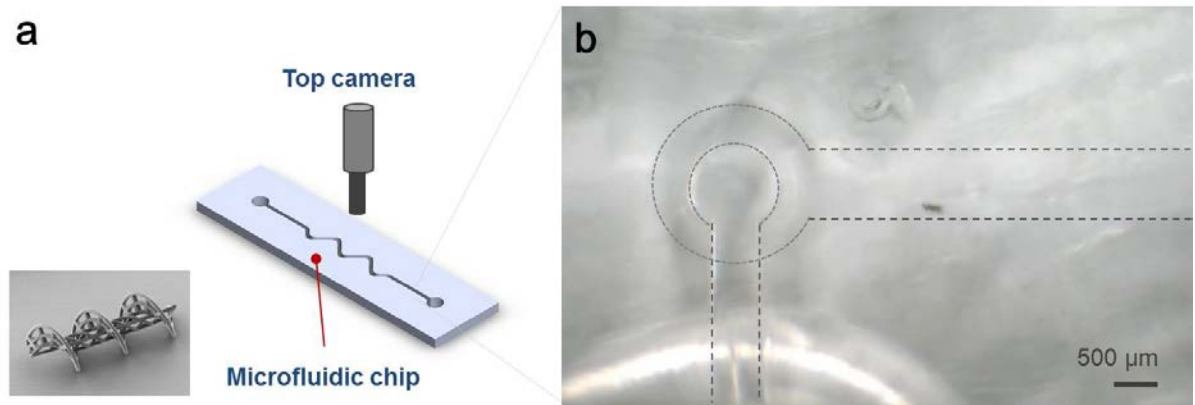
Figure 3.23 Video captured image for helical microrobots with planar channel configuration. (a) The schematic image of channel configuration with camera position as well as image of helical microrobot, (b) manipulation of microrobot in the planar placed channel [28].
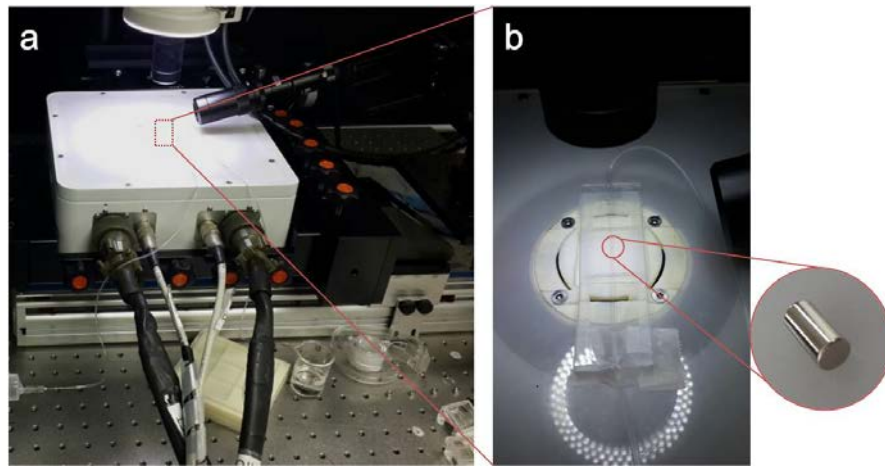
Figure 3.24 experimental setup for manipulation of microrobots in the pressure driven fluidic channel. (a) Silicon tube based fluidic channel on the magnetic manipulator, (b) Enlarged images of the silicon tube based fluidic channels with cylinder microrobots.

3.5.2 Manipulation in the pressure driven channel

Manipulation experiments of microrobots were conducted not only in the static fluids, but also in the perfusion environment within confined channels. The microfluidic channels fabricated were tested first, but the flow rate control of fabricated PDMS based microfluidic channel was very difficult to have meaningful and stable flow rate conditions. Therefore, the larger size of fluidic channel using silicon tubes was used to test the pressure effect on motion

of microrobots. Figure 3.24 shows the experimental setup for manipulation of microrobots in the pressure driven fluidic channel. The microrobot with cylinder neodymium (NdFeB) magnet was used for manipulation. The channel is connected with syringe pump for the flow rate control. Motion of microrobots can be modeled as applied forces on microrobots shown in Figure 3.23. External magnetic field gradient generated the magnetic force to translate microrobots, and the pressure also makes microrobot move. Therefore the total forces acting on microrobots along with x-axis are the summation of the forces on microrobots.
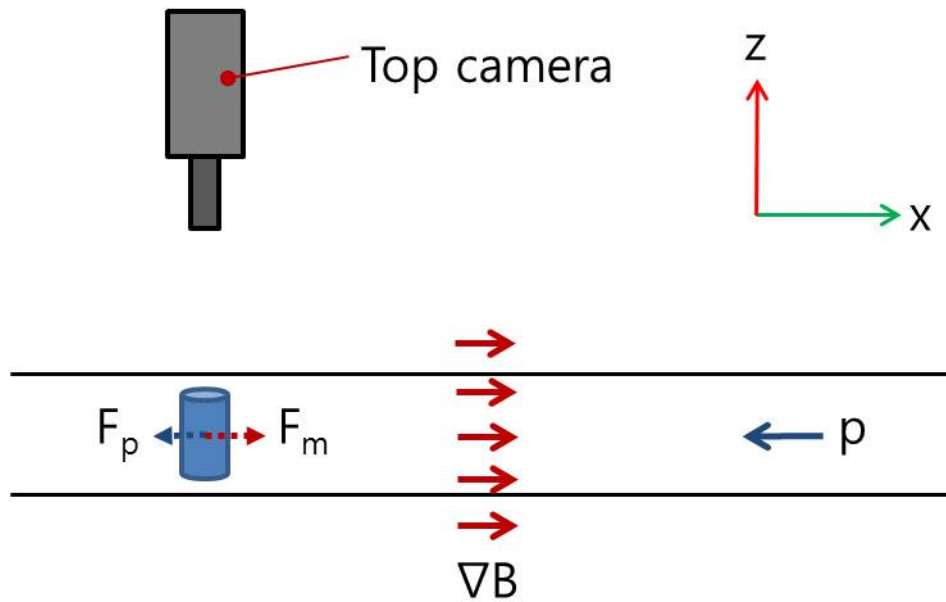
Figure 3.25 Schematics of forces acting on microrobot. The magnetic force and the force by pressure make the equilibrium state.

First experiment with cylinder magnet was conducted with viscosity change of silicon oil. The cylinder length was 800 μm, and the diameter was 400 μm. The magnetic field gradient was applied from 100 mT/m to 800 mT/m with 100 mT/m of increasing. Microrobot was aligned into z-direction to reduce the surface friction effect. The viscosity of silicon oil was 500, 1000, and 3000 cs with static fluid. Figure 3.26 shows the results of microrobot velocities under the three different fluid viscosities. The maximum velocities for cylinder

microrobots were 24000 um/s for 500 cs of silicon oil, and 12500 um/s for 1000, 4000 um/s for 3000 cs, respectively. By the incensement of fluid viscosity, the average velocities of microrobots were decreased because the effect of drag force. However for the higher viscous environment, the velocity results are showing the better linearity. This means the inertial force is getting weak in this high viscous fluid environment which is low Reynolds number fluid.
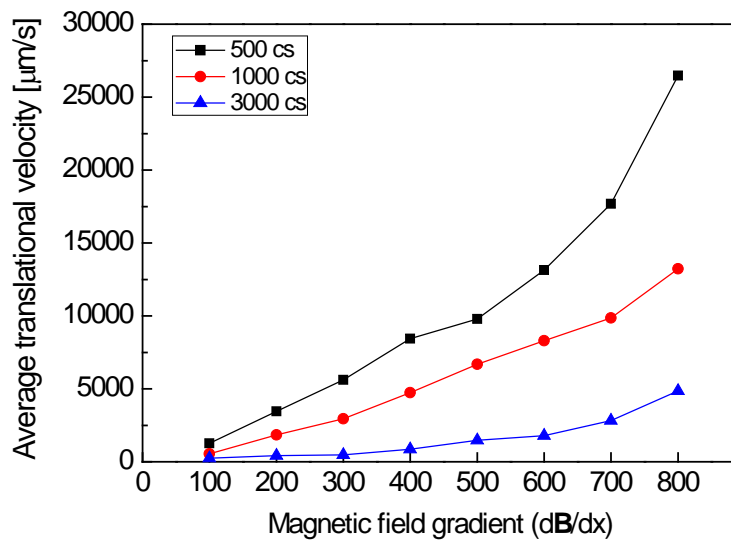
Figure 3.26 Velocity results for 800 μm of cylinder magnet by the magnetic field gradient with different viscosities of silicon oils.

And the cylinder magnet was manipulated with the pressure driven channel. Figure 3.27 is the video image of the cylinder magnet in the fluidic channel. The cylinder length was 400 μm, and the diameter was 250 μm. The channel inner diameter was 600 μm. The magnetic field gradient was applied from 400 mT/m, and 800 mT/m. Microrobot was also aligned into z-direction like previous experiment. The viscosity of silicon oil was 500 cs with 5 ml/m, and 10 ml/m of flow rate. Figure 3.28 shows the velocity results for 400 μm of cylinder magnet by the magnetic field gradient with different flow rates; 5 ml/m and 10 ml/m. The result

reveals that the flow pressure affects the microrobot force which is combined with the

magnetic force by the magnetic fields gradient.
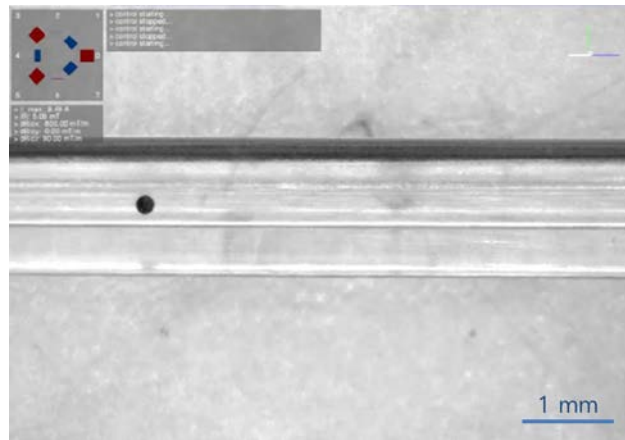
Figure 3.27 the video image for manipulation of the 400 μm of cylinder magnet in the fluidic channel.
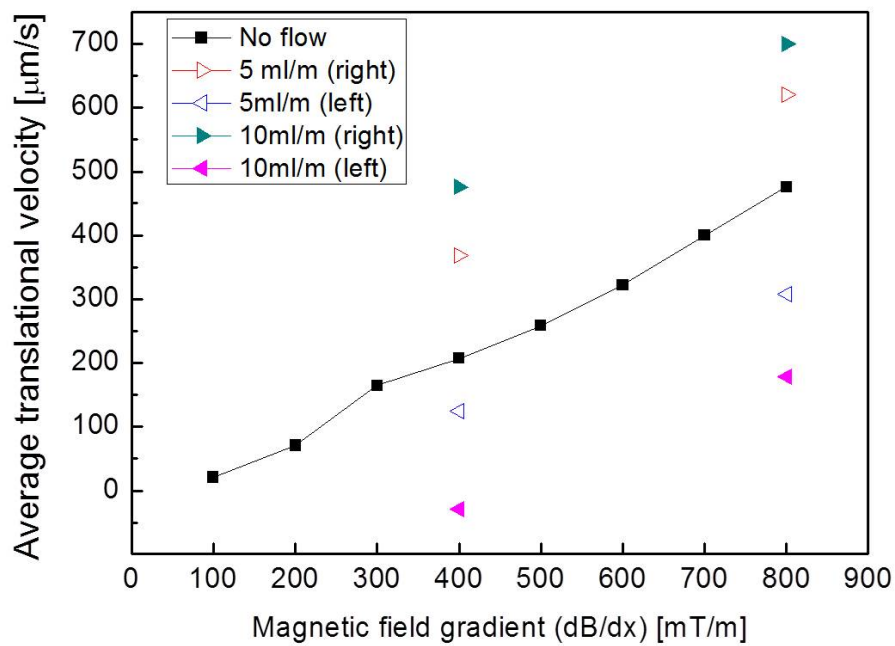
Figure 3.28 Velocity results for 400 μm of cylinder magnet by the magnetic field gradient with different flow rates.

4. CELL CULTURE AND DIFFERENTIATION EXPERIMENTS ON MICROROBOTS

4.1 Human embryonic kidney 293 cells culture on microrobots

HEK 293 cells were cultured on the cylindrical and hexahedral shape of microrobots. [39] Figure 4.1 shows SEM microscopy images of the cell cultured microrobots. The HEK 293 cells were affixed using paraformaldehyde solution, before SEM inspection, after 96 h of cell culture. Filopodia formed during cell migration, as depicted in the enlarged SEM image (Figure 4.1(b)), which indicates that the cells interacted with the microrobots. Also the confocal microscope images after staining the cells are shown in Figure 4.2. The microrobots were coated with poly- L -lysine (PLL) before cell culture. PLL is a synthetic amino acid chain that is positively charged and used widely as a coating material to enhance cell attachment. In addition, PLL does not react in the staining assay. Since the cell surfaces are negatively charged, cells attach to the PLL via ionic bonding. Since PLL is a synthetic molecule, it does not stimulate cells cultured on it biologically. Therefore, we can consider the microrobot as a supporting structure and PLL simply as a linking material for cells. [40]
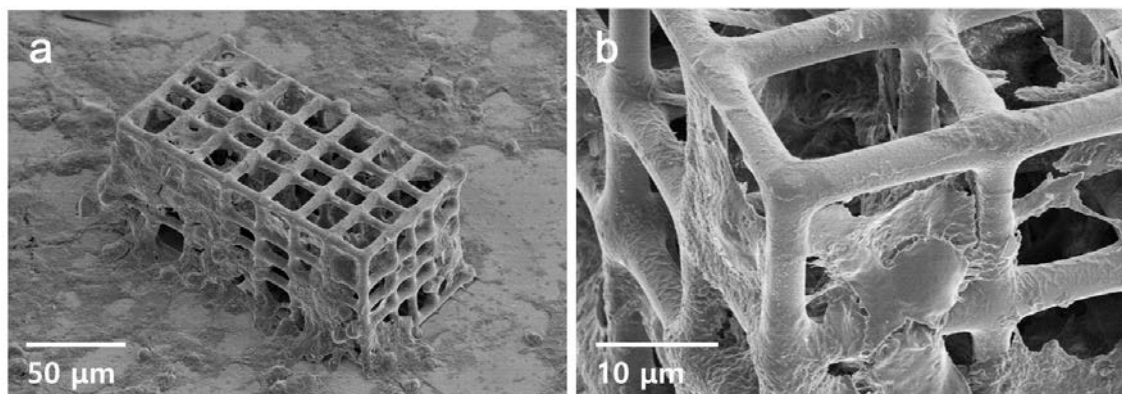
Figure 4.1 SEM images of a hexahedral microrobot after cell culture. (a) Whole microrobot image, and (b) enlarged SEM image [88].

The results revealed that the microrobot material was not cytotoxic to the myoblasts, as indicated by the ease in adhesion, migration, and proliferation of the cells over the structure. The confocal microscopy images were obtained after staining the cells inside. The detailed protocols for HEK 293 culture on microrobots are explained in the following sections.
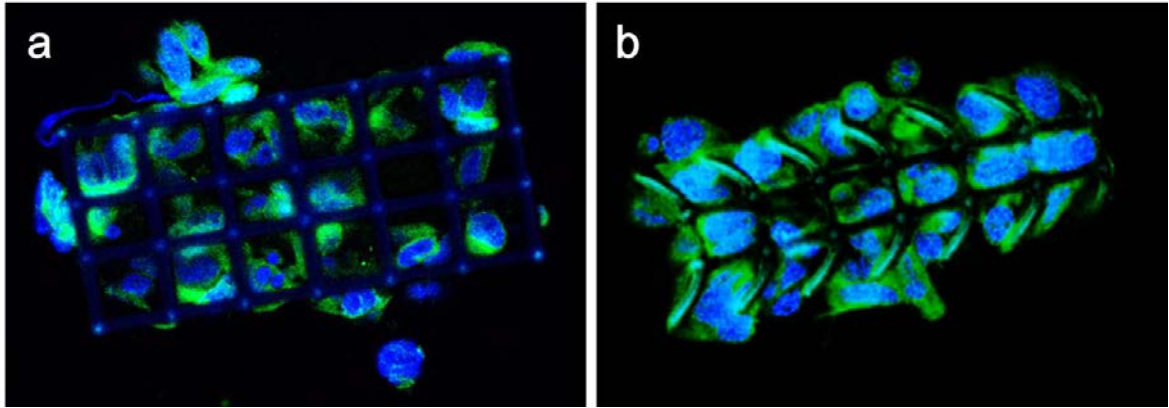
Figure 4.2 Confocal microscope images after staining the cells for the a) hexahedral microrobot and b) cylindrical microrobot [88].

4.1.1 Cell culture and SEM inspection

Prior to cell seeding, the microrobot fabricated on a glass wafer was coated with 10 μg mL^{-1} of poly-L-lysine (PLL) (Sigma Chemical Co., USA), followed by sterilization using an autoclave and ultraviolet irradiation. The human embryonic kidney 293 (HEK 293) cells were grown on dishes in Dulbecco's Modification of Eagle's medium (DMEM) (Thermo, USA), supplemented with 10% fetal bovin serum (FBS) (Thermo, USA) and 1% antibiotics at 37°C under 5% CO_2. HEK293 cells (1×10^6 cells per mL) were seeded in the culture dish containing the microrobot. The dish was stored in an incubator at 37°C under 5% CO_2. The cells were cultured for four days, and the growth media was changed every other day. After four days, we immersed the microrobot in 4% paraformaldehyde (PFA) solution, and stored the microrobot at 4°C overnight. Lastly, the microrobot was coated with platinum for examination using SEM.

4.1.2 Immunocytochemistry assay

First, we affixed the HEK 293 cells cultured in the PLL-coated microrobots using a 4% PFA solution. The cells were immersed in 0.5% Triton X-100, which contained Dulbecco's phosphated buffered solution (DPBS) (Thermo, USA), at room temperature. After 10 min, the cells were incubated with DPBS containing 4% normal donkey serum (NDS) (Jackson Immuno Research, USA) for 1 h. To label β-actin, we incubated the cells with antibodies against β-actin (Chemicon, Germany) diluted at 1:500 at 4°C for 2 h. Subsequently, the cells were washed twice with DPBS and incubated with fluorescein isothiocyanate (FITC) conjugated antibodies (Jackson Immuno Research, USA), diluted at 1:1000 for cytoskeletal staining at room temperature for 2 h. We visualized the nucleus of cells cultured in the microrobot using DAPI (Vector, USA) and β-actin under a confocal microscope (LMS 700, Zeiss, Germany). Confocal microscopy images were taken of the microrobots on a glass substrate as shown in Figure 4.3. The microrobot contained cells inside of its structure, and was detached for wireless manipulation.
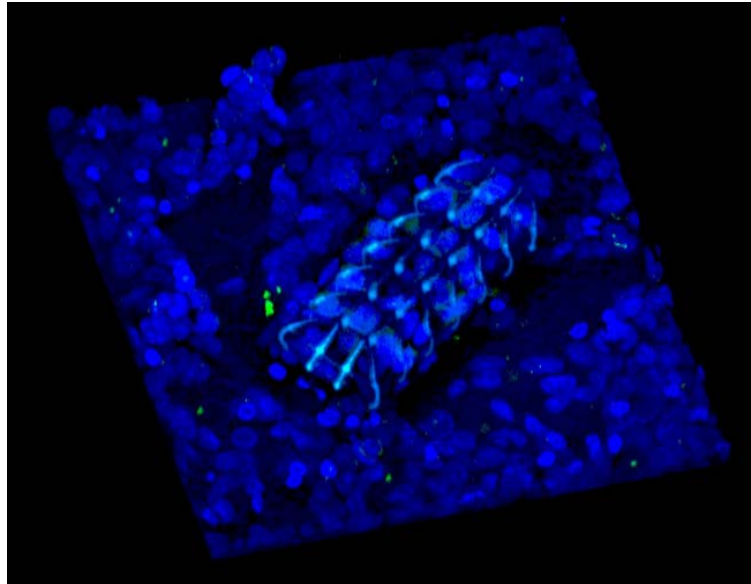
Figure 4.3 Confocal 3D microscopy image of a cylindrical microrobot on a glass substrate after staining the cells [88].

4.2 Hippocampal neural stem cells culture on microrobots
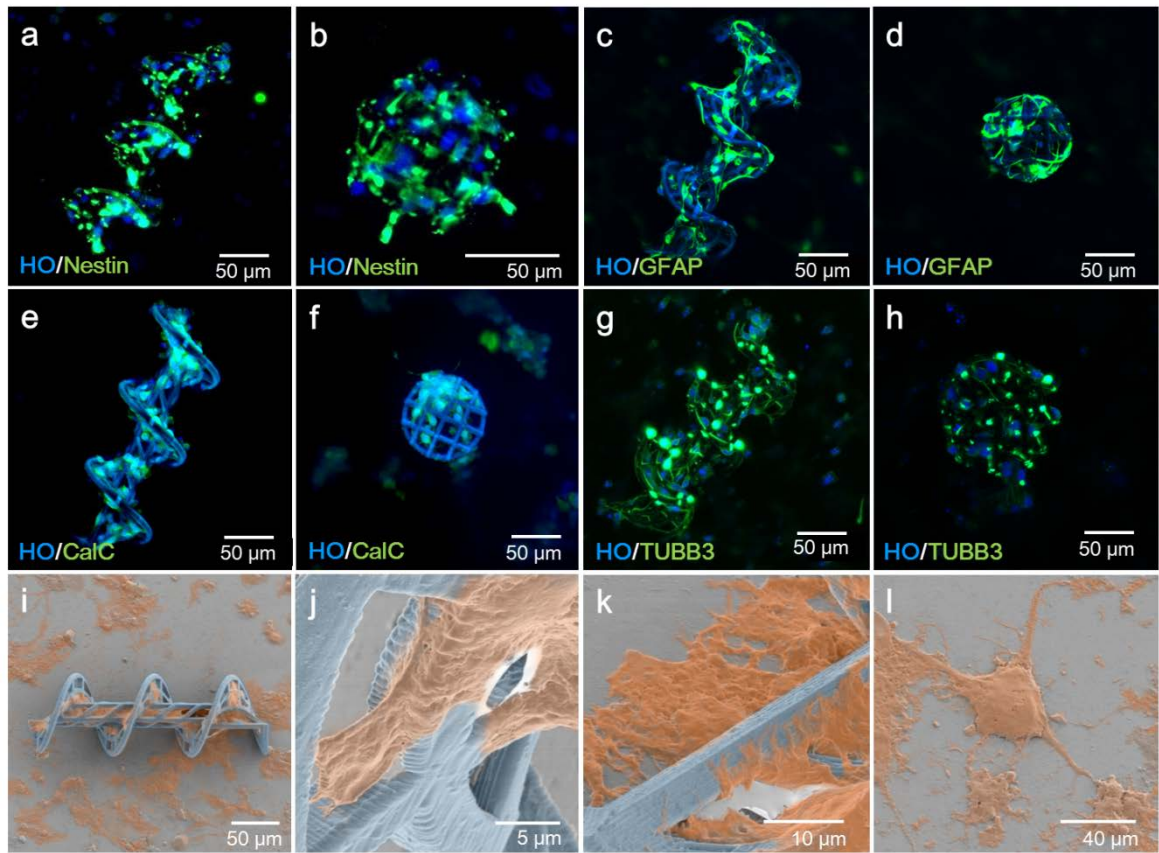
Figure 4.4 Immunofluorescent and SEM images of hippocampal NSCs cultured on microrobots.
Hippocampal NSCs were cultured on (a) helical and (b) spherical microrobots. Immunofluorescent
images of differentiated hippocampal NSCs on helical and spherical microrobots for (c, d) astrocyte, (e, f)
oligodendrocyte, and (g, h) neurons. SEM images for (i) differentiated neurons, (j) enlarged, suspended
neurites, (k) entangled neurites on the helical microrobot, and (l) neurons on a substrate. The cell type-
specific markers (Nestin for NSCs, GFAP for astrocytes, GalC for oligodendrocytes, and TUBB3 for
neurons) were co-stained with Hoechst 33342 nucleus marker for visualization [28].

As a proof of concept for targeted NCS therapy using helical and spherical scaffold-type microrobots, hippocampal NSCs were cultured on the microrobots. The attachment, proliferation, and differentiation of hippocampal NSCs on the microrobots were investigated using confocal microscopy. Figure 4.4 shows immunofluorescence and electron microscope images of the hippocampal NSCs after attachment and differentiation on the microrobots. Nestin (green) and Hoechst 33342 (blue) were used as NSC and nuclear markers, respectively, to show the attached NSCs (Figure 4.4(a, b)). The NSCs were differentiated into astrocytes

(Figure 4.4(c, d)), oligodendrocytes (Figure 4.4(e, f)), and neurons (Figure 4.4(g, h)) for 72 h in differentiation media designed for each cell lineage.

SEM images were also used to investigate the cell morphologies of differentiated neurons on the helical microrobots, as shown in Figure 4.4(i-l). The SEM images showed that differentiated neurons were sustained on the scaffold microrobot (Figure 4.4(i, j)), entangled with the frame (Figure 4.4(k)), and the entire neuron shape can be seen clearly on the substrate (Figure 4.4(l)). These results indicate that the microrobot was not cytotoxic to the NSCs, as indicated by attachment, proliferation, and differentiation of the NSCs on the structures. The morphologies of each cell were similar to those in 2D cultures, as shown in Figure 4.5 which is the same cells cultured on the conventional 2D plates.

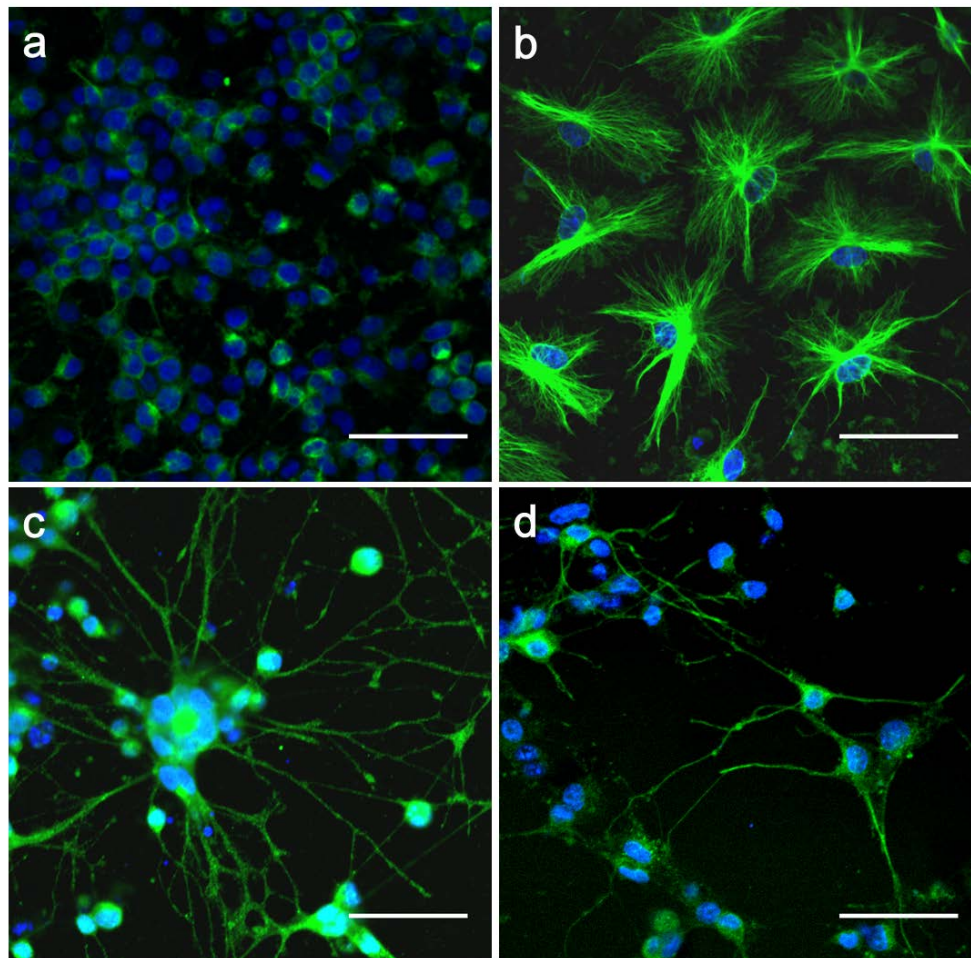**Figure 4.5 Immunofluorescent images are shown for (a) hippocampal NSCs, (b) astrocytes, (c) oligodendrocytes, and (d) neurons. Scale bar, 50 μm [28]**
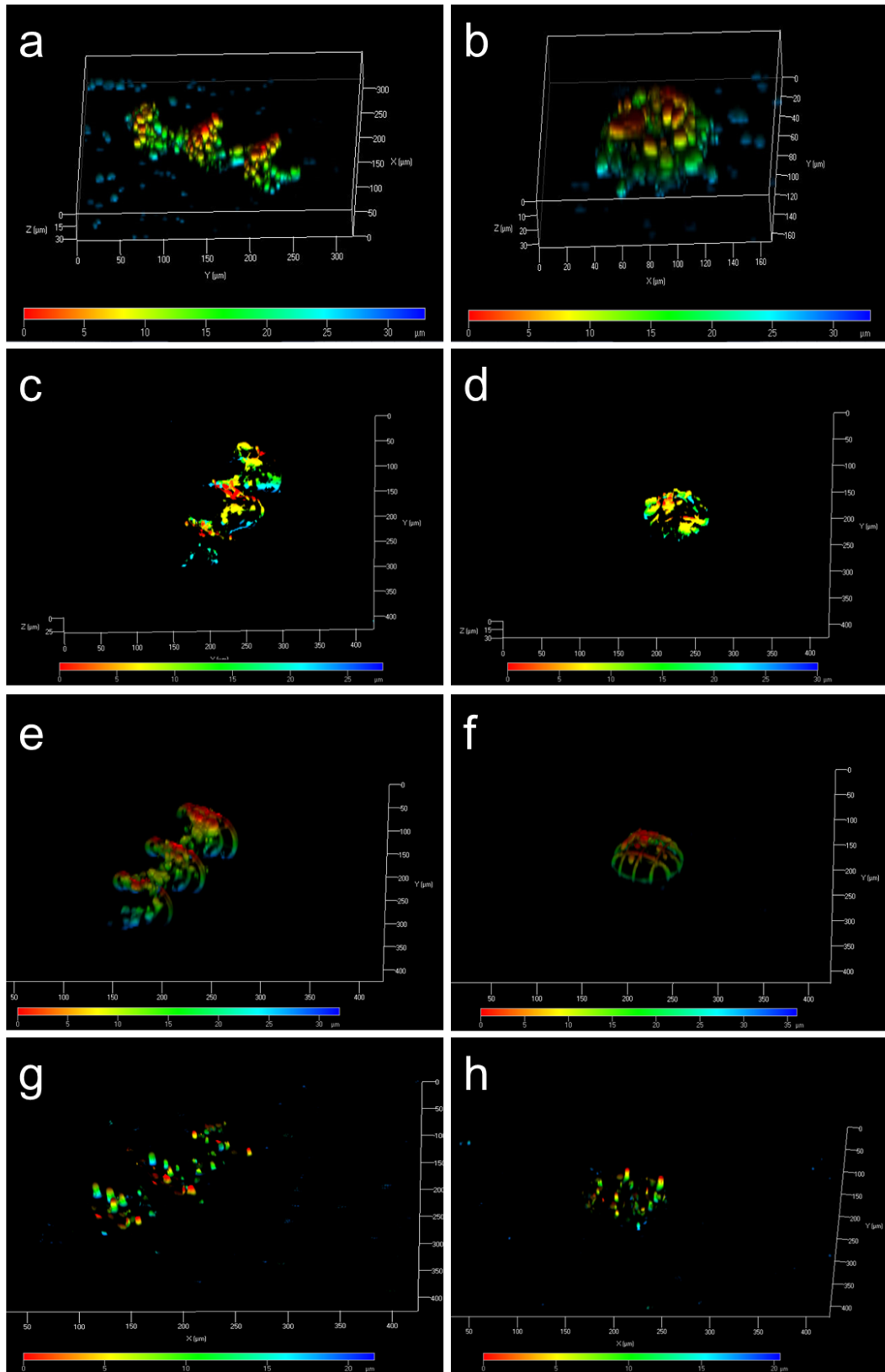
Figure 4.6 Images of the 3D hippocampal NSCs distributed on the helical (a) and spherical (b) microrobots. Shown are the 3D cell distributions for astrocytes (c, d), oligodendrocytes (e, f), and neurons (g, h) following differentiation [28]

4.2.1 Detailed protocols for Hippocampal NSC culture and differentiation

All procedures for the care and use of laboratory animals were approved by the Institute's Animal Care and Use Committee (IACUC, No. 0014) at DGIST. Hippocampal NSCs were isolated from the hippocampus of seven-week-old female Sprague Dawley rats and cultured in the chemically defined serum-free media containing Dulbecco's modified Eagle's medium/Ham's F12 (#12400-024, Invitrogen, Carlsbad, CA, USA) containing 20 µg/mL basic fibroblast growth factor (bFGF; #100-18B, Peprotech, NJ, USA) and N2 components, 1.27 g/L sodium bicarbonate (#S6014, Sigma-Aldrich), and 1% penicillin/streptomycin (#SV30010, Hyclone, UT, USA). Hippocampal NSCs were grown on plates coated with 10 µg/mL poly-L-ornithine (PLO; #3655, Sigma-Aldrich) for 8 h and then 5 µg/mL laminin (#354232, BD, CA, USA) overnight.

For differentiation, hippocampal NSCs were grown with microrobots on sterilized glass substrates coated with PLO and laminin at a density of $\sim 1 \times 10^5$ cells/mL. Hippocampal NSCs were incubated for 24 h in the culture medium, which was replaced with the differentiation medium for each lineage. The culture medium was supplemented with (1) 1 µM retinoic acid (RA; BML-GR100-5000, Enzo, NY, USA) and 5 µM forskolin (BML-CN100-0100, Enzo) for neurons, (2) 1 µM RA, 2 ng/mL bFGF, and 1% fetal bovine serum (FBS; #SH30071.03HI, Hyclone, UT, USA) for oligodendrocytes, and (3) 1 µM RA and 5% FBS for astrocytes. Every 2 days, half of the differentiation medium was replaced with fresh differentiation medium.

4.2.2 Analysis and cell counting

The proposed microrobots are promising scaffolding structures for NSC transplantation. The 3D cell distribution graphs on the helical and spherical microrobots are shown in Figure 4.6. Images were reconstructed from fluorescent z-stacked images (from Figure 4.4(a-h)). These results indicated that NSCs attached and differentiated on the microrobots with a

uniform distribution. The cells on each microrobot were counted, and the results are shown in Figure 4.7 and 4.8. The number of cells on each microrobot were counted using Image J. NSCs grown on the helical and spherical microrobots were counted following 24 and 72 h culture (Figure 4.7(a-c)), and again after differentiation (Figure 4.7(d-f)). The normalized cell counts before and after differentiation are shown in Figure 4.8. Normalization was performed by dividing the number of cells on microrobots by the surface area of each microrobot. Variabilities between the number of cells on the same surface area were recorded. Following 24 h proliferation, two times as many cells were present on the helical microrobots, compared to the number of cells on the spherical microrobots. These data suggest that cell attachment on the helical microrobot was superior to that of the spherical type due to the larger surface area.
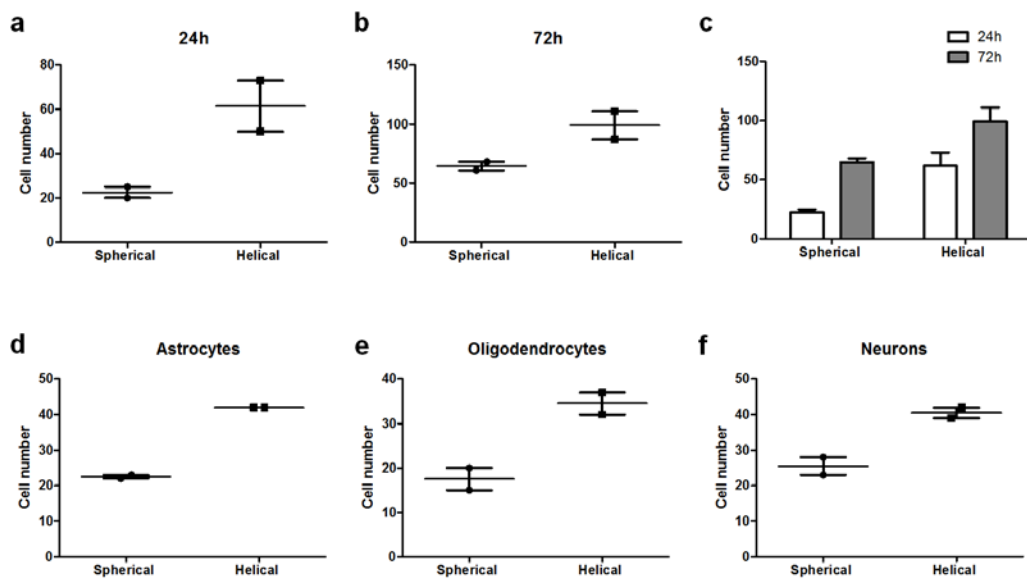

Figure 4.7 Cell counts. The number of proliferated cells on the microrobots following 24 (a) and 72 h (b) differentiation. (c) A comparison of cell counts. The number of cells on the microrobots following differentiation into astrocytes (d), oligodendrocytes (e), and neurons (f). N=2 [28].
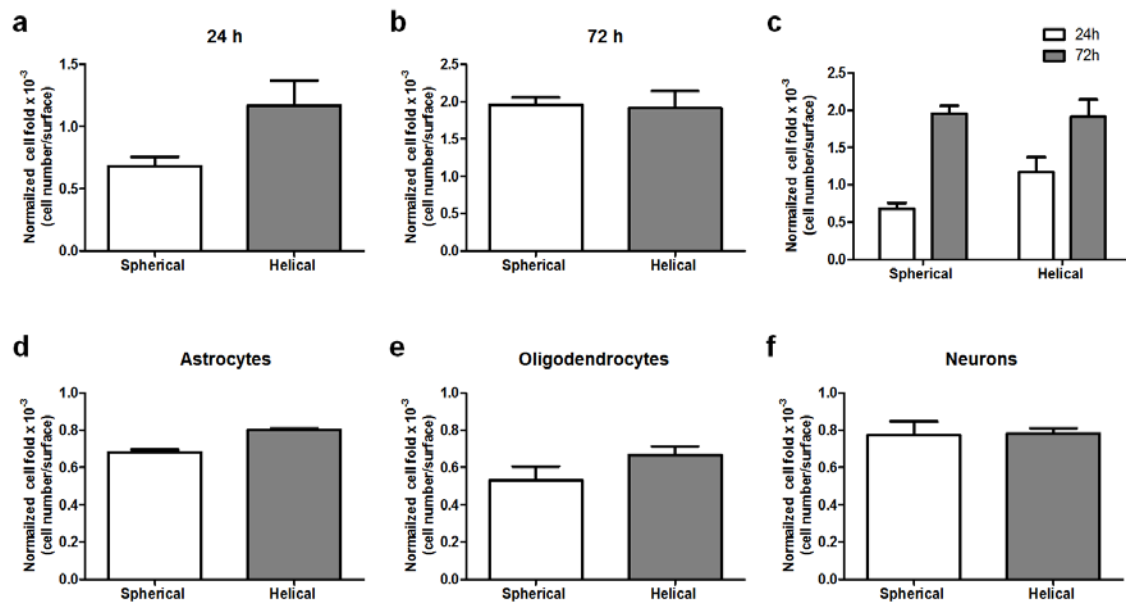
Figure 4.8 Cell counts. The number of stem cells following 24 (a) and 72 h (b) culture. (c) A comparison of cell counts. The number of cells on the microrobots following differentiation into astrocytes (d), oligodendrocytes (e), and neurons (f). The normalized cell fold is the number of cells per surface area for each microrobot. N=2 [28].

Manipulation of the scaffold-type microrobots with attached cells was conducted after cell culturing on the microrobots. The hippocampal NSCs were cultured on the surface of the microrobots following the protocol outlined in the online Supplementary methods. Figure 4.9 reveal the manipulation results for cell-cultured microrobots. The motion of the helical microrobots was changed from the corkscrew motion to the tumbling motion with a decrease in microrobot velocities.

The NSCs were attached and differentiated for each microrobot. The numbers of cells increased from 23 to 65 on a spherical microrobot, and from 61 to 99 on a helical microrobot at 24 h and 72 h, respectively. The number of cells on the helical microrobot was 2.65 times and 1.62 times larger than that of the spherical microrobot at 24 and 72 h, respectively, probably because the surface area of the helical microrobot is 1.56 times larger than that of the spherical microrobot.

5. CONCLUSION

In summary, scaffold type microrobots for a targeted cell delivery system were developed as smart microrobotic devices for cell transportation. The fabricated porous 3D structures could be used as bio-scaffolds to transport the cells/tissues to target points with coated magnetic materials under the control of magnetic fields. A 3D laser lithography system was used to fabricate the SU-8 structures, and nickel and titanium were deposited as magnetic and biocompatible materials, respectively. The optimum fabrication parameters were established and could be easily customized for different cells. The scaffold type microrobots had a pore size of 10~ 20 μm, a length of 150 μm, and diameter of 75 μm The microrobots were shaped as hexahedrons and cylinders, and manipulated by external magnetic fields. Scaffold-type microrobots with helical and spherical shapes were developed as a platform for NSC culture with higher propulsion efficiencies. When the normalized input current was 4.57 A, the velocity of the helical microrobots was 432.7 μm/s at 5 mT and 35 Hz (29.63 times faster than 14.6 μm/s of the cylindrical microrobot at 300 mT/m) and the velocity of the spherical microrobots was 686.0 μm/s at 5 mT and 20 Hz (46.98 times faster than the velocity of the cylindrical microrobot). The helical and spherical microrobots also showed precise position and orientation control by complex trajectory driving. Thus, corkscrew and rolling motions showed higher propulsion efficiencies than the pulling motion, and would be more suitable for precise and versatile manipulation in a fluidic environment. We demonstrated the manipulation of the microrobots with complex trajectories and in a microfluidic channel. Ciliary microrobots were also developed as one of the bio-inspired microrobot which swims in the low Reynolds number fluid efficiently. The position and orientation of the fabricated ciliary microrobots were manipulated magnetically in DI water and 10 CS of silicon oil, and the maximum average velocity of the microrobots in DI water was 340 μms^{-1} (1.55 body

lengths per second) under 12 mT field intensities at 60 Hz of frequency. The external stepping magnetic field with 0-110° of polar angle change generates an actuating force, which results in different stroke patterns of the cilia during the power stroke and recovery stroke. The translational velocities were evaluated by changing the frequency and applied magnetic field intensity. Locomotion of ciliary microrobots was first demonstrated, and this propulsion mechanism represents a high-efficiency swimming method for microrobots. HEK293 cells were cultured on these microrobots to confirm their feasibility as a cell transportation system. The materials used for the structures were not cytotoxic to myoblasts, as the cells readily adhered, migrated, and proliferated over the structure. Cell attachment, proliferation, and differentiation of the hippocampal NSCs on the microrobots were confirmed with immunofluorescent staining and SEM images. The NSCs were used for targeted and controlled differentiation into astrocytes, oligodendrocytes, and neurons on the microrobots. These results showed the feasibility of the microrobot as a platform for a new era of neuroregenerative medicine. The proposed microrobots are promising tools for *in vivo* NSC delivery, with high propulsion efficiencies for future stem cell therapies.

ACKNOWLEDGEMENT

REFERENCES

[1]   Intuitive Surgical, Inc., (http://www.intuitivesurgical.com)

[2]   Given Imaging Ltd., (http://www.givenimaging.com)

[3]   Virob medical microrobot, Medgadget.

[4]   Zhang, L. *et al.* Artificial bacterial flagella: Fabrication and magnetic control. *Appl. Phys. Lett.* **94,** 064107 (2009).

[5]   A. Ghosh, P. Fischer, Nano Lett. 2009, 9, 2243 –2245.

[6]   RoboBee, Harvard university, (https://en.wikipedia.org/wiki/RoboBee)

[8]   Institute of Robotics and Intelligent Systems (IRIS), Multi Scale Robotics Lab. (MSRL), ETHZ, (https://www.cnet.com/news/microrobot-swims-through-eyes-to-deliver-drugs/)

[9]   International Journal of Robotics Research, 2013: V32, p218-246, Planning and Control for Microassembly of Structures Composed of Stress-Engineered MEMS Microrobots, DOI: 10.1177/0278364912467486.

[10]   Magmites, Institute of Robotics and Intelligent Systems (IRIS), Multi Scale Robotics Lab. (MSRL), ETHZ

[11]   Nelson, B. J., Kaliakatsos, I. K. & Abbott, J. J. Microrobots for Minimally Invasive Medicine. Annu. Rev. Biomed. Eng. 12, 55 (2010).

[12] Sitti, M. Miniature devices: Voyage of the microrobots. Nature 458, 1121-1122 (2009).

[13] Fusco, S. et al. Microrobots: a new era in ocular drug delivery. Expert Opin. Drug Deliv. 11, 1815 (2014).

[14] Park, S., Cha, K. & Park, J. Development of Biomedical Microrobot for Intravascular Therapy. Int. J. Adv. Robot. Syst. 7, 91-98 (2010).

[15] Forgione, A. In vivo microrobots for natural orifice transluminal surgery. Current status and future perspectives. Surg. Oncol. 18, 121-9 (2009).

[16] Ullrich, F. et al. Mobility Experiments with Microrobots for Minimally Invasive Intraocular Surgery. Invest. Ophthalmol. Vis. Sci. 54, 2853-2863 (2013).

[17]   https://web.stevens.edu/msrobotics/SMRDC2010/pastwin.html

[18] Hoover A M, Steltz E, Fearing R S, "RoACH: An autonomous 2.4g crawling hexapod robot", IEEE/RSJ International Conference on Intelligent Robots and Systems, pp 22-26, September, 2008.

[18] B. Subia, J. Kundu, S. C. Kundu, "Biomaterial Scaffold Fabrication Techniques for Potential Tissue Engineering Applications," in *Tis. Eng.* vol. 2, Ch. 6, D. Eberli, Ed. Intech, 2010, pp. 141-158.

[19] F. Klein, B. Richter, T. Striebel, C. M. Franz, G. Freymann, M. Wegener, and M.

Bastmeyer, "Two-Component Polymer Scaffolds for Controlled Three-Dimensional Cell Culture," *Adv. Mater.,* vol. 23, pp. 1341-1345, 2011.

[20] Nanotechnological strategies for engineering complex tissues, Nature Nanotechnology 6, 13-22 (2011).

[21] Gage, F. H. Mammalian Neural Stem Cells, *Science* **287**, 1433-1438 (2000).

[22] Lindvall, O., Kokaia, Z. & Martinez-Serrano, A. Stem cell therapy for human neurodegenerative disorders-how to make it work. *Nat. Med.* **10**, S42-S50 (2004).

[23] Palmer, T. D., Takahashi, J. & Gage, F. H. The Adult Rat Hippocampus Contains Primordial Neural Stem Cells. *Mol. Cell. Neurosci.* **8**, 389-404 (1997).

[24] Amariglio, N. *et al.* Donor-Derived Brain Tumor Following Neural Stem Cell Transplantation in an Ataxia Telangiectasia Patient. *PLOS med.* 6, 221 (2009).

[25] Kelly, S. *et al.* Transplanted human fetal neural stem cells survive, migrate, and differentiate in ischemic rat cerebral cortex. *Proc. Natl. Acad. Sci. USA.* **101**, 11839-11844 (2004).

[26] S. Kim, *et al.* Fabric of Magnetically Actuated Microstructure for Targeted Cell Transportation, Proceedings of the 13th IEEE International Conference on Nanotechnology, Beijing, China, August 5-8, 2013.

[27] Fusco S, Chatzipirpiridis G, Sivaraman KM, et al. Chitosan electrodeposition for microrobotic drug delivery. Adv Healthc Mater, 2013;2(7):1037-44.

[28] S. Kim, *et. al.*, DGIST, Unpublished data.

[29] Tung, H. *et al.* Polymer-Based Wireless Resonant Magnetic Microrobots. *IEEE Trans.Robot.* **30,** 26 (2014).

[30] Metin Sitti, Carnegie Mellon University's (CMU) NanoRobotics Lab, bacteria-based microrobots.

[31] Pensilvenia

[32] Park, Sung Jun, et al., "New paradigm for tumor theranostic methodology using bacteria-based microrobot," *Scientific Reports,* vol. 3, pp. 3394, 2013.

[33] Bacteriobot, Robot Research Initiative, Chonnam University..

[34] Metin Sitti, Carnegie Mellon University's (CMU) NanoRobotics Lab, Mag-μBot

[35] DGIST-ETH Micororobor Research Center, polymer helical swimmer fabricated by 3D laser lithography, Unpublised data.

[36] Tottori, S. *et al.* Magnetic Helical Micromachines: Fabrication, Controlled Swimming, and Cargo Transport. *Adv. Mat.* **24,** 811-816 (2012).

[37] Cheang, U. K., Lee, K., Julius, A. & Kim, M. Multiple-robot drug delivery strategy through coordinated teams of microswimmers. *Appl. Phys. Lett.* **105,** 08375 (2014).

[38] Cheang, U. K. & Kim, M. Self-assembly of robotic micro- and nanoswimmers using magnetic nanoparticles. *J. Nanopart. Res.* **17,** 145 (2015).

[39] Jiang, G. et al. Development of rolling magnetic microrobots. *J. Microme. Microeng.* **20**, 085042 (2010).

[40] Dreyfus, R. *et al.* Microscopic artificial swimmers. *Nature* **437,** 862 (2005).

[41] Khalil, I. M. Dijkslag, H. C., Abelmann, L. & Misra, S. Magneto Sperm: A microrobot that navigates using weak magnetic fields. *Appl. Phys. Lett.* **104,** 223701 (2014)

[42] Precise cell manipulation with microrobotic insertion system

[43] S. Kim. *et al.* Fabrication and Manipulation of Ciliary Microrobots with Non-reciprocal Magnetic Actuation. *Sci. Rep.* **29**, 30713 (2016).

[44] S. Schuerle, S. Erni, M. Flink, B.E. Kratochvil, and B.J. Nelson, *IEEE Tran. Magn.* **2013**, 49, 321.

[45] Schuerle, S., Erni, S., Flink, B., Kratochvil, B. E. & Nelson, B. J. Three-dimensional Magnetic Manipulation of Micro- and Nanostructures for Applications in Life Sciences. *IEEE Tran. Magn.* **49,** 321 (2013).

[46] Carnegie mellon university,

[47] Nanomag, Institute of Robotics and Intelligent Systems (IRIS), Multi Scale Robotics Lab. (MSRL), ETHZ.

[48] M. P Jummer, J. J. Abott, B. E. Kratochvil, R. Borer, A. Sengul, and B. J. Nelson, Octomag: An Electromagnetic System for 5-DOF Wireless Micromanipulation, IEEE TRANSACTIONS ON ROBOTICS, VOL. 26, NO. 6, DECEMBER 2010.

[49] INSA Center.

[50] Geonnam university.

[51] Aeon Phocus, Aeon Scientific, GmbH, Switzerland.

[52] Niobe system, Stereotaxis, Inc., USA.

[53] Robotic Catheter Guidance Control and Imaging (CGCI) system, Magnetecs, Inc., USA.

[54] J. J. Abbott, *et al.* How Should Microrobots Swim? *Int. J. Robot. Res.* 28, 1434 (2009).

[55] Zhang, L. *et al.* Characterizing the Swimming properties of Artificial Bacterial Flagella. *Nano. Lett.* **9,** 3663-3667 (2009).

[56] Peyer, K. E., Zhang, L. & Nelson, B. J. Bio-inspired magnetic swimming microrobots for biomedical applications. *Nanoscale* **5,** 1259 (2013).

[57] Gao, W. *et al.* Bioinspired Helical Microswimmers Based on Vascular Plants. *Nano Lett.* **14,** 305 (2014).

[58] Peyer, K. E., Tottori, S., Qui, F., Zhang, L. & Nelson, B. J. Magnetic Helical Micromachines. *Chem. Eur. J.* **19,** 28 (2013).

[59] Qiu, F. *et al.* Noncytotoxic artificial bacterial flagella fabricated from biocompatible ORMOCOMP and iron coating. *J. Mater. Chem. B* **2,** 357 (2014).

[60] Barbot, A., Decanini, D. & Hwang. G. On-chip Microfluidic Multimodal Swimmer toward 3D Navigation. *Sci. Rep.* **6,** 10941 (2016).

[61] Gao, W. Sattayasamitsathit, S., Manesh, K. M., Weihs, D. & Wang, J., Magnetically Powered Flexible Metal Nanowire Motors. *J. Am. Chem. Soc.* **132,** 14403 (2010).

[62] Gao, W. *et al.* Cargo-Towing Fuel-Free Magnetic Nanoswimmers for Targeted Drug Delivery. *Small* **8,** 460-467 (2012).

[63] Jang, B. *et al.* Undulatory Locomotion of Magnetic Multilink Nanoswimmers. *Nano Lett.* **15,** 4829 (2015).

[64] Ghosh, A. & Fischer, P. Controlled Propulsion of Artificial Magnetic Nanostructured Propellers. *Nano Lett.* **9,** 2243 (2009).

[65] Maier, A. M. *et al.* Magnetic Propulsion of Microswimmers with DNA-Based Flagellar Bundles. *Nano Lett.* **16,** 906 (2016).

[66] Hill, D. B. *et al.* Force Generation and Dynamics of Individual Cilia under External Loading. *Biophys. J.* **98,** 57 (2010).

[67] Ghanbari, A. & Bahrami, M. A novel Swimming Microrobot Based on Artificial Cilia for Biomedical Applications. *J. Intell. Robot. Syst.* **63,** 399 (2011)

[68] Khademolhosseini, F. & Chiao, M. Fabrication and Patterning of Magnetic Polymer Micropillar Structures Using a Dry-Nanoparticle Embedding Technique. *J. Microelectromech.* **22,** 131 (2013).

[69] Palagi, S. *et al.* Structured light enables biomimetic swimming and versatile locomotion of photoresponsive soft microrobots. *Nat. Mater.* (2016).

[70] Paek, J., Cho, I. & Kim, J. Microrobotic tentacles with spiral bending capability based on shape-engineered elastomeric microtubes. *Sci. Rep.* **5,** 10768 (2015).

[71] Park, S. J. *et al.* New paradigm for tumor theranostic methodology using bacteria-based microrobot. *Sci. Rep.* **3,** 3394 (2013).

[72] Ou, Y., Kim, D., Kim, P., Kim, M. & Julius, A. A. Motion Control of Tetrahymena pyriformis Cells with Artificial Magnetotaxis: Model Predictive Control (MPC) Approach. *Paper presented at IEEE Int. Conf. Robot. Aut., Saint Paul,* Minnesota doi: 10.1109/ICRA.2012.6225015 (2012, May 14-18).

[73] Williams, B. J., Anand, S. V., Rajagopalan, J. & Saif, M. T. A self-propelled biohybrid swimmer at low Reynolds number. *Nat. Commun.* **5,** 2081 (2014).

[74] Gibbs, J. & Zhao, Y. Catalytic nanomotors: fabrication, mechanism, and applications. *Front. Mater. Sci.* **5,** 25 (2011).

[75] Purcell, E. M. Life at low Reynolds number. Amer. J. Phys. **45,** 3 (1977).

[76]   V.L. Tsang,   S.N. Bhatia, *Adv. Drug Deliv. Rev.* **2004**, 56, 1635.

[77]   S. C. Owen, M. S. Shoichet, *J. Biomed. Mater. Res. A.* **2010**, 94A, 1321.

[78]   B. Subia, J. Kundu, S.C. Kundu, in *Tis. Eng.* Vol. 2 (Eds: D. Eberli), Intech, **2010**, Ch. 6.

[79]   O.A. Abdelaal,   S.M. Darwish, *Wor. Aca. of Sci., Eng. and Tech.* **2011**, 59, 577.

[80]   R. Wittig, E. Waller, G. Freymann, R. Steiner, *J. Laser Appl.* **2012**, 24, 042011.

[81]   E. Kapyla, D.B. Aydogan1, S. Virjula, S. Vanhatupa, S. Miettinen, J. Hyttinen, M. Kellomaki, J. Micromech. Microeng. 2012, 22, 115016.

[82]   F. Klein, T. Striebel, J. Fischer, Z. Jiang, C.M. Franz, G. Freymann, M. Wegener, M. Bastmeyer, Adv. Mater. 2010, 22, 868.

[83]   F. Klein, B. Richter, T. Striebel, C.M. Franz, G. Freymann, M. Wegener, M. Bastmeyer, Adv. Mater. 2011, 23, 1341.

[84] C. Liu, in Foundations of MEMS, Prentice-Hall, Englewood Cliffs, NJ 2005.

[85] V. Iacovacci, G. Lucarini, L. Leonardo & A. Menciassi, Lab-on-a-Chip Fabrication and Application, Nanotechnology and Nanomaterials, Margarita Stoytcheva and Roumen Zlatev, ISBN 978-953-51-2458-0, 2016.

[86] http://nptel.ac.in/courses/115103038/module5/lec35/2.html.

[87] Nanoscibe, User manual, GmbH, Germany.

[88] Kim, S. *et al.* Fabrication and Characterization of Magnetic Microrobots for Three-dimensional Cell Culture and Targeted Transportation. Adv. Mat. 25, 5863 (2013).

[89] Slotted Photonic Crystal Sensors, Mark G. Scullion, Thomas F. Krauss and Andrea Di Falco, Sensors 2013, 13(3), 3675-3710.

[90] Abbott, J. J., Ergeneman, O., Kummer, M. P., Hirt, A. M. & Nelson, B. J. Modeling Magnetic Torque and Force for Controlled Manipulation of Soft-Magnetic Bodies. *IEEE Trans. Robot.* **23,** 1247 (2007).

요 약 문

표적지향형 세포전달을 위한 자기장 구동의 마이크로로봇의 설계, 제작 및 특성평가

세포연구 및 표적지향형 수송을 위한 플랫폼으로써 자기장에 의해 조작되는 마이크로로봇이 개발되었다. 본 논문에서는 의용학적 사용을 위한 마이크로로봇으로 표적치료, 미세 환경에서의 효과적인 추진방법, 자기장 조작, 및 전자성 코일 시스템에 관하여 간단히 소개하였다. 제안한 마이크로로봇은 3 차원 레이저 리소그래피로 구조물이 제작되고 및 스퍼터링 시스템을 통해 자성물질 및 생체적합성 물질이 증착되었으며 유체 환경에서 유영하기 위해 정밀 자기장 제어가 실시되었다. 지지체형 마이크로로봇은 세포 크기와 유사한 20 ㎛ 내외의 공극을 가지는 다공성 구조물에 3 차원 세포배양을 통해 많은 양의 세포를 특정 목표지점으로 운송할 수 있다. 지지체형 마이크로로봇은 끌림운동, 구름운동, 나사선 추진운동 등의 다양한 구동 메커니즘을 적용할 수 있도록 원통형, 육면체형, 나선형 및 구형 등의 다양한 모양으로 설계되었다. 첫번째로 원통형 및 육면체형과 같은 덩어리 모양의 지지체 마이크로로봇이 설계, 제작되었으며 자기장 기울기에 의해 끌림구동 되었다. 최대 평균속도는 DI water 내에서 800 mT/m 의 자기장 기울기를 인가하였을 때, 원통형의 경우에 50 ㎛/s, 육면체형의 경우 35 ㎛/s 로 측정되었다. 끌림구동으로 추진하였을 때는 속도 및 추진효율이 비교적 낮은데 이것은 저 레이놀즈 수에서 유체의 점성의 영향이 커지게 되어 끌림구동 마이크로로봇이 극복하기 힘들어지기 때문이다. 미세 유영환경에서 추진효율을 향상시키기 위해 나사선 추진법 및 굴림 추진법이 제안되었고, 이를 위해 지지체형 로봇을 나사선 모양 및 구형모양으로 각각 제작하였다. 최대 평균속도는 DI water 내에서 15 mT 의 자기장 세기와 각각의 step-out 회전주파수를 인가하였을 때, 나선형 로봇의 경우 550 ㎛/s 로, 구형의 경우 1400 ㎛/s 로 측정되었으며, 이것은 기존의 원통형 및 육면체형의 마이크로로봇의 경우에 비해 대단히 증가된 속도이다. 네가지 지지체형 로봇의 에너지 효율은 속도와 자기장 제어기에

인가된 전류값의 비율로 정의되었으며, 이들 로봇들의 에너지 효율이 비교되었다. 원통형과 육면체형 로봇에 비해 나선형과 구형 로봇의 에너지 효율이 월등히 높았다. 또한 저 레이놀즈 수 환경에서 고추진 효율을 가지는 로봇의 한 형태로 섬모 마이크로로봇이 개발되었다. 섬모 로봇은 자연에 존재하는 짚신벌레와 같은 미생물의 섬모의 모양과 섬모의 비대칭적 노젓기 운동을 모방하여 제작된 생체모사형 마이크로로봇이다. 긴 타원구형의 몸통의 양쪽에 4 개씩 총 8 개의 섬모가 부착되어 있는 모양의 섬모 마이크로로봇이 제작되었고 stepping 자기장에 의해 섬모의 비대칭적 왕복운동을 구현하였다. 섬모의 비대칭적 노젓기 운동은 로봇이 추진하기 위한 알짜힘을 생성하고, 섬모가 왕복할 때 내는 힘과, 섬모의 휘어짐 각도 등이 계산되었으며 섬모 마이크로로봇의 이동속도 또한 측정되었다. 또한 복잡한 경로 주행, 입자 운송 등이 시현되었으며 이것은 향후 정밀 약물운송의 가능성을 보여주었다. 개발된 나선형 및 구형 지지체 마이크로로봇은 미세 유체채널 내에서 구동되었으며 이것은 혈관 등과 같은 체내 속박된 환경에서 구동의 가능성을 보여주는 것이다. Human embryonic kidney (HEK) 세포 및 hippocampal 뇌줄기세포 (Neuronal stem cell; NSC) 등이 제작된 지지체형 마이크로로봇에 3 차원 배양되었으며, 뇌줄기세포의 경우에는 astrocyte, oligodendrocyte, 및 neuron 으로 분화되는 것을 확인하였다.

결론적으로 다양한 모양과 구동방식을 가지는 다공성 지지체형 마이크로로봇 및 섬모 마이크로로봇이 미세 공정기술을 통해 개발되었다. 로봇의 구조는 3 차원 레이저 리소그래피를 통해 제작되었으며, 표면에 니켈 및 티타늄 코팅을 통해 자성을 띠면서 생체 적합성을 가지도록 제작되었다. 제작된 마이크로로봇은 자기장에 의해 정밀 구동되었으며, 그 속도 및 에너지 효율이 측정 및 비교되었다. 또한 Human embryonic kidney (HEK) 세포배양 및 hippocampal 뇌줄기세포가 제작된 지지체형 로봇에 배양 및 분화되었고, 원하는 위치로 제어되어 향후 세포치료에 응용 가능한 마이크로로봇의 가능성을 확인하였다.

핵심어: 마이크로로봇, 지지체, 표적치료, 자기장 조작, 미세공정기술, MEMS 기술, 생체모방 기술, 섬모 마이크로로봇, 3 차원 세포배양, 줄기세포, 줄기세포 분화, 줄기세포 치료

APPENDIX

Measurement of magnetic property of deposited nickel on microrobots

The M-H curve of nickel, deposited on scaffold type microrobots was conducted. Figure 2.7 shows the measured magnetization per unit volume for nickel using Physical Property Measurement System (PPMS; Quantum Design, US). The measured saturation magnetization per volume was 686 kA/m 1 (686 emu/cm^3) and the coercivity was 5 kA/m (62.83 Oe). The measured sample we used is piece of substrate which microrobots are on it.

Nickel volume: 0.2 µm $\times$ 8885426 µm^2 = 1.777085 $\times$ 10^{-3} m^3

Some part of law data from the equipment.

H	M	M/volume	M/volume	M/volume	H
Oe	emu	emu/m3	emu/cm3	A/m	A/m
-0.13404	-4.29E-05	-2.41E-02	-2.41E+04	-2.41E+07	-10.6666
-1.91398	-4.27E-05	-2.40E-02	-2.40E+04	-2.40E+07	-152.31
11.725	-3.61E-05	-2.03E-02	-2.03E+04	-2.03E+07	933.0459
40.25313	4.25E-05	2.39E-02	2.39E+04	2.39E+07	3203.242
67.72167	9.14E-05	5.14E-02	5.14E+04	5.14E+07	5389.119
92.63966	1.50E-04	8.44E-02	8.44E+04	8.44E+07	7372.03
118.9317	2.22E-04	1.25E-01	1.25E+05	1.25E+08	9464.287

Magnetic moment of the sample

Unit conversion

1 Oe= $1000/4\pi$ A/m, emu/cm^3= 1000 A/m

	Cylinder (type B)		Hexahedron (type B')	
Material	SU-8	Nickel	SU-8	Nickel
Density	1237 kg/m^3	8900 kg/m^3	1237 kg/m^3	8900 kg/m^3
Volume	155526 μm^3	24182 μm^3	207325 μm^3	30591 μm^3
Mass	1.92X10^{-10} kg	2.15X10^{-10} kg	2.56X10^{-10} kg	2.72X10^{-10} kg
Total mass	4.08×10^{-10} kg		5.28×10^{-10} kg	

Writing codes for 3D laser lithography (For nanowrtie, Nanoscribe, GmbH, Germany)

For the writing of the 3D structures by using the 3D laser lithography, we need writing codes which are gwl file format. The header file for the 3D laser lithography is shown in below. This file is coded by Nanowrite software (Nanoscribgm GmbH)

```
% File generated by DeScribe 2.1

% Writing parameters
PiezoScanMode
ContinuousMode
ConnectPointsOn
SettlingTime 300

% PerfectShape Initialization
PerfectShapeIntermediate
psPowerProfile "IP Resist"

% System Initialization
measuretilt 4
TiltCorrectionOn
ResetInterface
invertzaxis 1

% Field Parameters
XOffset 0
YOffset 0
ZOffset 0

PowerScaling 1
LaserPower 35


% Include slicer output

MoveStageX 400
FindInterfaceAt 1.6
include rectangle1_data.gwl

MoveStageY 300
FindInterfaceAt 1.6
include cylinder1_data.gwl

MoveStageY 300
FindInterfaceAt 1.6
include sphere1_data.gwl

MoveStageY 300
FindInterfaceAt 1.6
include helix3_data.gwl

MoveStageY 300
```

In the codes, the each structures are included as also gwl format, which file is the sequence coordinates of the scanning points. This writing coordinates data for spherical shape of structure is shown in below that is the one example. This detailed data is generated by Describe Nanowrite software (Nanoscribgm GmbH)

```
% Layer 1/267, Z = 0.000
39.152    38.262    0.000
39.225    38.285    0.000
40.642    38.458    0.000
40.642    40.389    0.000
40.059    39.649    0.000
40.059    41.607    0.000
39.152    41.732    0.000
39.130    41.709    0.000
38.711    41.536    0.000
38.711    38.458    0.000
38.883    38.387    0.000
39.152    38.262    0.000
Write
39.559    39.293    0.000
39.559    41.171    0.000
39.242    41.214    0.000
39.211    41.201    0.000
39.211    38.787    0.000
40.142    38.900    0.000
40.142    39.091    0.000
39.559    39.293    0.000
Write

…(clipping)

39.967    39.825    79.800
40.138    39.997    79.800
39.967    40.168    79.800
39.795    39.997    79.800
39.967    39.825    79.800
Write
```